T.R.

GEBZE TECHNICAL UNIVERSITY

GRADUATE SCHOOL OF NATURAL AND APPLIED SCIENCES

IMPROVING CURVING PERFORMANCE OF MONORAIL VEHICLE BY USING SEMI ACTIVE DAMPERS

ALİ SUAT YILDIZ

A THESIS SUBMITTED FOR THE DEGREE OF

DOCTOR OF PHILOSOPHY

DEPARTMENT OF MECHANICAL ENGINEERING

GEBZE

2019

T.R.

GEBZE TECHNICAL UNIVERSITY

GRADUATE SCHOOL OF NATURAL AND APPLIED SCIENCES

IMPROVING CURVING PERFORMANCE OF MONORAIL VEHICLE BY USING SEMI ACTIVE DAMPERS

ALİ SUAT YILDIZ

A THESIS SUBMITTED FOR THE DEGREE OF DOCTOR OF PHILOSOPHY

DEPARTMENT OF MECHANICAL ENGINEERING

THESIS SUPERVISOR

PROF. DR. SELİM SİVRİOĞLU

GEBZE

2019

T.C.
GEBZE TEKNİK ÜNİVERSİTESİ
FEN BİLİMLERİ ENSTİTÜSÜ

MONORAY TAŞITLARININ VİRAJ DİNAMİKLERİNİN YARI AKTİF SÖNÜMLEYİCİLER İLE İYİLEŞTİRİLMESİ

ALİ SUAT YILDIZ
DOKTORA TEZİ
MAKİNE MÜHENDİSLİĞİ ANABİLİM DALI

DANIŞMANI
PROF. DR. SELİM SİVRİOĞLU

GEBZE
2019

GEBZE TEKNİK ÜNİVERSİTESİ	**DOKTORA JÜRİ ONAY FORMU**

GTÜ Fen Bilimleri Enstitüsü Yönetim Kurulu'nun 03/07/2019 tarih ve 2019/30 sayılı kararıyla oluşturulan jüri tarafından 30/07/2019 tarihinde tez savunma sınavı yapılan Ali Suat YILDIZ'ın tez çalışması Makine Mühendisliği Anabilim Dalında DOKTORA tezi olarak kabul edilmiştir.

JÜRİ

ÜYE (TEZ DANIŞMANI)	: Prof. Dr. Selim SİVRİOĞLU
ÜYE	: Prof. Dr. Erkan ZERGEROĞLU
ÜYE	: Doç. Dr. Ahmet Sinan ÖKTEM
ÜYE	: Dr. Öğr. Üyesi Yalçın EYİGÜN
ÜYE	: Dr. Öğr. Üyesi Muzaffer METİN

ONAY

Gebze Teknik Üniversitesi ..... Enstitüsü Yönetim Kurulu'nun ...../...../..... tarih ve ...../..... sayılı kararı.

SUMMARY

This work is concerned with improving the curving performance of the monorail vehicles which are one of the modern mass transport systems, by using semi-active magnetorheological (MR) dampers. Controlling the curving dynamic of monorail vehicles with semi-active devices is a new research area. In the context of the study, a new barrier Lyapunov function (BLF) based constrained backstepping control design is presented for vibration suppression of the suspension system. The considered monorail vehicle has a single segment supported by two bogies. As a secondary suspension, lateral and vertical MR dampers are taken into consideration in addition to the air suspensions. Also, the proposed controllers are investigated along with the designed road profiles based on the International Standard Organization (ISO) 8608 classification.

The control performances of the proposed control approach are compared with robust H∞ control, the quadratic Lyapunov function (QLF) based adaptive control and the passive case along with the designed road profiles. To make a conclusive judgment about the effectiveness of the proposed semi-active control strategies, a co-simulation structure that consists of a 38 degree of freedom (DOF) nonlinear full-scale vehicle model is constructed. Such a co-simulation structure provides an opportunity to investigate dynamic system response under various curve radius, vehicle speed and wind load effect. Also, proposed control approaches are implemented experimentally by using a suspension test setup.

Parametric uncertainties in running tires and vehicle mass are taking into consideration in the control simulations. According to the simulation and experimental results, the designed controllers improved the roll, yaw and vertical motions of the monorail vehicle when compared to uncontrolled and passive cases. It is concluded that the proposed control approaches provide better ride comfort and ride safety without violating suspension rattle space constraint, and despite the uncertainties in suspension parameters as well as small turning radius can be achieved by monorail vehicles equipped with the semi-active suspension system.

Key Words: Semi-active Suspension, Adaptive Controller, Monorail Vehicle, Robust Control, Backstepping Controller.

ÖZET

Bu çalışmada, yarı-aktif manyetoreolojik (MR) damperleri kullanarak, modern toplu taşıma sistemlerinden biri olan monoray taşıtlarının viraj performansının iyileştirilmesi amaçlanmıştır. Monoray taşıtların viraj dinamiklerinin yarı aktif sönümleyiciler kullanarak kontrol etmek yeni bir araştırma alanıdır. Çalışma kapsamında, taşıt titreşiminin bastırılması için yeni bir Lyapunov fonksiyon tabanlı kısıtlı geriadımlama kontrol tasarımı sunulmuştur. Ele alınan monoray aracı, iki boji tarafından desteklenen tek bir segmente sahiptir. İkincil süspansiyon, hava süspansiyonlarına ek olarak yanal ve dikey MR sönümleyicileri içerecek şekilde modellenmiştir. Ayrıca önerilen denetleyici tasarımları, Uluslararası Standartlar Teşkilâtı (ISO) standartlarında tanımlanan yol pürüzlülük profilleri altında incelenmiştir.

Farklı eğri yarıçapına sahip yol profilleri ile gürbüz kontrol ve uyarlamalı kontrol tasarımlarının, odaklanan performans kriterlerine etkileri araştırılmış ve kontrolör etkinliği MR sönümleyicinin bağlı olmadığı "Kontrolsüz", MR sönümleyicinin bağlı olduğu ancak herhangi bir gerilim uygulanmadığı ''Pasif'' durumlar ile sonuçlar kıyaslanmıştır. Önerilen denetleyici etkinlikleri 38 serbestlik derecesine sahip bir monoray modeli içeren eşzamanlı simülasyon ortamında test edilmiştir. Oluşturulan bu yapı ile birlikte farklı hız ve rüzgar yükü gibi çalışma şartları oluşturulabilmektedir. Ayrıca, deneysel test sistemi kullanılarak deneysel kontrol çalışması gerçekleştirilmiştir. Monoray tahrik tekerlerinde, taşıt gövdesinin kütlesinde ve MR sönümleyici matematiksel model parametrelerinde belirsizlikler içerdiği kabulü ile kontrol tasarımları gerçekleştirilmiştir. Simülasyon ve deneysel sonuçları incelendiğinde, tasarlanan kontrol yapıları, kontrolsüz ve pasif durumlara kıyasla monoray taşıtın yuvarlanma, yalpalama ve düşey hareketlerini iyileştirdiği görülmektedir. Bu iyileştirmelerin konfor ve sürüş güvenliğinde sağladığı avantajların yanısıra, yarı aktif süspansiyon sistemine sahip monoray sistemleri ile küçük dönüş yarıçapları elde edilebileceği sonucuna varılmıştır.

Anahtar Kelimeler: Yarı-aktif Süspansiyon, Uyarlamalı kontrol, Monoray Taşıt, Gürbüz Kontrol, Geriadımlama Kontrol.

ACKNOWLEDGEMENTS

Firstly, I would like to thank my supervisor, Prof. Dr. Selim SİVRİOGLU, for his unwavering support since I arrived at Gebze Technical University. I appreciate his guidance and technical insight to complete this work.

I articulate my thankfulness to Prof. Dr. Erkan ZERGEROĞLU for his encouragement and invaluable guidance.

I wish to express my gratitude to the members of my dissertation committee: Prof. Dr. Ercan ERTÜRK, Assoc. Prof. Ahmet Sinan ÖKTEM, Asst. Prof. Muzaffer METİN and Asst. Prof. Yalçın EYİGÜN for taking the time to read my thesis and their support and guidance.

I wish to express my warm and sincere thanks to Asst. Prof. Sinan BAŞARAN and Asst. Prof. Fevzi Çakmak BOLAT for their collaboration and friendship.

I am highly indebted to my family who has made all this possible: my mother and father, and my sister.

And, last but not least, I give my sincere thanks to my dear wife for her support and encouragement.

TABLE of CONTENTS

	Page
SUMMARY	v
ÖZET	vi
ACKNOWLEDGEMENTS	vii
TABLE of CONTENTS	viii
LIST of ABBREVIATIONS and ACRONYMS	x
LIST of FIGURES	xii
LIST of TABLES	xv
1. INTRODUCTION	1
1.1. Suspended Monorails	2
1.2. Supported (Straddle-beam) Monorails	2
1.3. Previous Studies Related to Monorail Vehicles	5
1.4. Scope and Contribution of the Thesis	8
1.5. Structure of the Thesis	9
2. MODELLING OF THE STRADDLE-TYPE MONORAIL VEHICLES	10
2.1 Tire Modelling Approaches	11
2.2. MR Damper Parameter Identification	15
2.3. Road Profile Design	19
2.3.1. Guideway Surface Roughness	23
2.4. The Dynamic Equations for Straddle Monorail Vehicle	27
2.5. Assessment of the Critical Design Parameters	37
3. ROBUST CONTROL DESIGN	41
3.1. Monorail Vehicle with Uncertainties in Model Parameters	42
3.2. MR Damper Model with Multiplicative Uncertainty	43
3.3. Weighting Transfer Function for Sensor Noises	46
3.4. Selection of the Performance Filters	46
4. ADAPTIVE CONTROL DESIGN	50
4.1. Adaptive Control Design Based on QLF	50
4.1.1. Comparison of Ride Comfort	57
4.1.2. Comparison of Curving Performance	58

4.1.3. Parameter Adaptation Performance 59
4.2. Adaptive Backstepping Control Design Based on BLF 61
4.2.1. A Numerical Study of the Proposed Control Approaches 68
5. VALIDATION OF THE PROPOSED CONTROL APPROACHES ON TEST SETUP 70
5.1. Experimental System 70
5.2 Power Consumption Analysis 76
5.3. Parameter Adaptation Performance 77
5.4. Control Performance Under Varying Operating Conditions 78
6. VALIDATION OF THE PROPOSED CONTROL APPROACHES USING CO-SIMULATION TOOL 81
6.1. Comparison of Curving Performance 83
6.2. Effect of the Crosswind 88
7. CONCLUSIONS AND RECOMMENDATION 91

REFERENCES 93
BIOGRAPHY 98
APPENDICES 99

LIST of ABBREVIATIONS and ACRONYMS

Abbreviations and Acronyms		**Explanations**
M_s	:	Mass matrix
C_s	:	Damping matrix
K_s	:	Stiffness matrix
$\ddot{x}(t)$	:	Acceleration vector
$\dot{x}(t)$	:	Velocity vector
$x(t)$	:	Displacement vector
f_{mr}	:	MR damper force
v_{maks}	:	Maximum Input current
$z(t)$	:	Inner state of the MR damper
κ_i	:	Positive control gain
v	:	Control voltage
σ_0	:	Stiffness of $z(t)$ influenced by $v(t)$
σ_1	:	Damping coefficient of $z(t)$
σ_2	:	Viscous damping coef. influenced by $v(t)$
σ_a	:	Stiffness of $z(t)$
a_0	:	Constant value
$\zeta_1, \zeta_2, \zeta_3$	:	Auxiliary filters
$\gamma_1, \gamma_2, \gamma_3$	:	Positive adaptation gains
ϕ	:	System parameter vector
$e(t)$	:	Position tracking error
r	:	Filtered error signal
a_w	:	Weighted acceleration
F_{gl}	:	Pre-pressure on the guiding tires
F_{sl}	:	Pre-pressure on the stabilizing tires
F_c	:	External force that exerted on the vehicle body

Υ	:	Track distance covered by the vehicle.
R	:	Curve radius
Δr	:	Tire deflection
C_x	:	Longitudinal slip stiffness
C_y	:	Lateral slip stiffness
i	:	Ratio of the super elevation
θ_{se}	:	Super elevation angle
V	:	Average monorail speed
G_d	:	Reference PSD function
q_i	:	Generalized coordinate
α_i	:	Sideslip angles of the tires
$F^{preload}$	:	Pre-pressure value on tires
a_{nc}	:	Critical unbalanced acceleration
$\bar{x}$	:	Filtered version of the signal
S	:	Suspension working space
V_i	:	Lyapunov Function candidate
W_p	:	Performance filter
W_n	:	Sensor noise filter
DOF	:	Degree-of-Freedom
QLF	:	Quadratic Lyapunov Function
BLF	:	Barrier Lyapunov Function
COG	:	The center of gravity
MR	:	Magnetorheological
LVDT	:	Linear Variable Differential Transformer
ISO	:	International Organization for Standardization
PSD	:	Power spectral density
PTP	:	Peak to Peak
NSD	:	Normalized suspension deflection
DLC	:	Dynamic load coefficient
UM	:	Universal Mechanism

LIST of FIGURES

Figure No:		Page
1.1:	Tire wear, a) partial abrasion, b) normal state.	1
1.2:	A view of suspended monorail: Chiba Monorail, Japan.	2
1.3:	A view of supported monorail: Daegu Monorail, South Korea.	3
1.4:	Bogie structure, a) bogie of a railroad vehicle, b) bogie of a straddle-type monorail vehicle	3
1.5:	Semi-active control approaches.	5
2.1:	Illustration of the straddle type monorail vehicle.	10
2.2:	Tire enveloping models.	11
2.3:	Tire forces and rotation.	12
2.4:	Overview of the structure of the tire model.	12
2.5:	Lateral force and slip angle relation.	14
2.6:	Lateral force comparison.	14
2.7:	MR damper parameter identification setup components.	18
2.8:	MR damper parameter identification: a) Displacement input b) Voltage to MR damper, c) Force responses of MR damper.	18
2.9:	Top view of the designed road profile.	21
2.10:	Curvature and cant of the road profile.	22
2.11:	Track beam super elevation setting mode.	22
2.12:	a) Simulated road profile, b) PSDs of the used road profiles (solid line) and upper bound (dotted line).	25
2.13:	Track surface roughness for running tires.	26
2.14:	Track surface roughness for guiding tires.	27
2.15:	Track surface roughness for stabilizing tires.	27
2.16:	Schematic rear view of the idealized monorail vehicle.	28
2.17:	Schematic side and top views of the idealized monorail vehicle.	29
2.18:	Vertical displacements of the bogies vehicle body.	35
2.19:	Lateral displacements of the bogies vehicle body.	35
2.20:	Yaw displacements of the bogies vehicle body	36
2.21:	Pitch displacements of the bogies vehicle body.	36
2.22:	Roll displacements of the bogies vehicle body.	37

3.1:	Generalized system structure.	41
3.2:	Open-loop block diagram model including structured uncertainties.	42
3.3:	Uncertain frequency responses of the monorail vehicle.	43
3.4:	Transfer function approximation: a) Input displacement, b) Force output.	44
3.5:	Open-loop vehicle model including uncertain actuator model.	45
3.6:	Frequency response transfer function.	45
3.7:	Inverse performance weighting functions for case 1.	48
3.8:	Open-loop interconnection.	48
3.9:	Frequency response of the controllers: a) Vertical acceleration, b) Lateral acceleration.	49
4.1:	Top view of the designed road profile for simulations.	53
4.2:	Curvature and cant of the road profile.	53
4.3:	Vehicle body roll acceleration.	55
4.4:	Vehicle body lateral acceleration.	55
4.5:	Vehicle body vertical displacement.	56
4.6:	Force output of the MR damper placed at the left side of the front bogie.	56
4.7:	Vertical and lateral comfort values.	58
4.8:	Front bogie inner side running tire lateral displacement.	58
4.9:	Front bogie inner side running tire vertical force.	59
4.10:	Estimation behaviour of the monorail mass values to their true values.	60
4.11:	Estimation of the damping and stiffness parameters to their real values.	60
4.12:	Nonlinear filter function response: a) Effect of the dead zone and b) Effect of the exceeded limits.	62
4.13:	Monorail body lateral displacement on the route.	69
5.1:	Experimental Quarter car setup.	71
5.2:	Schematic diagram of the experimental setup.	72
5.3:	Experimentally realized the road profile and B-grade road profile.	72
5.4:	Vertical acceleration spectrum of the simulated model and the experimental system.	73

5.5:	Vehicle body displacement.	73
5.6:	Unsprung mass acceleration.	74
5.7:	Sprung mass vertical acceleration output spectrum.	74
5.8:	Measured instantaneous current.	76
5.9:	Total consumed power.	77
5.10:	Estimation of the damping and stiffness parameters to their real values.	78
5.11:	RMS value of the frequency-weighted acceleration of the sprung mass.	79
5.12:	Peak to peak values of suspension rattle space at different speed levels.	79
5.13:	Dynamic load coefficient	80
6.1:	Illustration of the straddle type monorail vehicle.	82
6.2:	Co-simulation system with a semi-active control strategy	82
6.3:	Track beam surface roughness.	83
6.4:	Front Bogie COG lateral deflection with various curve radius.	84
6.5:	Monorail body lateral displacement on the curve radius of 300 m.	85
6.6:	Monorail body rolling angle on the curve radius of 300 m.	85
6.7:	Stabilizing tire deflection on the curve radius of 200 m.	86
6.8:	Passive system entering the curve segment at excessive speed.	86
6.9:	Voltage to MR dampers at radius of 100 m: a) Front Bogie, b) Rear Bogie.	87
6.10:	MR dampers force at a radius of 100 m: a) Front Bogie, b) Rear Bogie.	88
6.11:	Wind load acting on vehicle during the movement.	89
6.12:	Peak-to-peak values of body roll angle at different speed levels.	89
6.13:	Peak-to-peak values of front bogie lateral displacement at different speed levels.	90
6.14:	Lateral slip of the running tire at wind speed of 3 m/s.	90

LIST of TABLES

Table No:		Page
2.1:	Experimentally obtained values for the MR damper parameters.	19
2.2:	ISO road roughness classification.	24
2.3:	DOF of the vehicle index.	28
2.4:	Critical value of centrifugal acceleration.	39
2.5:	Maximum curving speed (m/s) with 13 kN preload.	40
4.1:	RMS and peak to peak values of the monorail body accelerations.	54
4.2:	Effect of the control approaches on ride comfort: weighted RMS values.	57
4.3:	RMS values of the monorail body accelerations.	69
5.1:	Parameters of the quarter car model.	71
5.2:	Summary of experimental results for the random road.	75
5.3:	Summary of experimental results in steep ramp and bump stages.	75
5.4:	Total energy consumption results (Joule).	77
5.5:	The controller parameter of the semi-active controller	78
6.1:	Peak to peak values of the front bogie lateral displacement.	84
6.2:	The values of aerodynamic coefficients.	89

1. INTRODUCTION

With the growth of urban population, the demand to increase the capacity of transport systems has been pushing engineers to develop faster, high capacity and more comfortable vehicles. To meet mass transit requirement and ensure urban sustainability, it is needed to take the pressure off overcrowded streets. At this point, monorail transit systems are the promising means of transportation vehicles to relieve urban traffic jam. In the early days, monorails were considered suitable only for amusement parks, this perspective changed when the Tokyo Monorail that went into service in 1964 by HITACHI. Nowadays, monorails have been used for transit systems in a number of countries including: China, South Korea, India, Japan, Brazil, and the USA. The length of the route varies from 6.6 km to 28 km in Japan and varies 1.7 km to 98 km in China. Monorail transit systems have some advantages such as;

- Capital costs for monorail systems are lower than those for heavy rail systems constructed either above or below grade level.
- Monorail vehicles can negotiate steep grades and small-radius curves
- Rubber tires also provide a quiet, comfortable ride for passengers. Monorail vehicles can also be operated driverless on the small radius of curve tracks.
- Acceleration and deceleration rates can be greater than rail rapid transit due to the higher adhesion between the rubber tire and concrete guideway.

In contradiction to conventional railways, the straddle type monorail traffic line is mainly curved, and the minimum circle curve radius may reach to 50 m. Small track beam radius deteriorates the driving stability and causes the running wheel of the vehicle seriously worn out frequently as seen in Figure 1.1.

Figure 1.1: Tire wear, a) partial abrasion, b) normal state [Du et al., 2017].

Such severe uneven wear of the running wheel not only decrease durability but also lead to the significant reduction of the adhesion ability of the running wheel. Two distinct classes of monorail systems have been implemented for transit purposes, these are grouped by the way in which their vehicles are supported and guided.

1.1. Suspended Monorails

The earliest representative countries in the world studied the suspended monorails are Germany and Japan. First suspended type passenger system was constructed in Wuppertal, Germany in 1901. The bogie structure of the suspended monorails is quite different than those of straddle type. Firstly, bogies are placed inside the box-beam bridge as given in Figure 1.2. and the bolster is supported on the bogie with the secondary suspensions, and the central pin is connected to the bolster by using a rotating hinge. Also, an articulated four-linkage mechanism is used to connect the central pin and the car body. As in straddle type monorail, suspended monorail bogies consist of four driving tires, four guiding tires and air spring as a secondary suspension.

Figure 1.2: A view of suspended monorail: Chiba Monorail, Japan.

1.2. Supported (Straddle-beam) Monorails

The straddle-type monorail vehicles have certain differences from traditional rail vehicles as seen in Figure 1.3. This system has a separate right of way, which has no

influence on the current ground transportation system. They stride over the guideway and run above it.

Figure 1.3: A view of supported monorail: Daegu Monorail, South Korea.

The major difference between monorails vehicles and traditional railway vehicles is that the propulsion units on monorails are included in each car. Monorail vehicles have three types of tires such as running, guide and stabilization tires as shown in Figure 1.4.b). While running tires provide the longitudinal movement, guide tires lead the truck along the guideway. In addition, stabilization tires prevent excessive rolling motion of the vehicle.

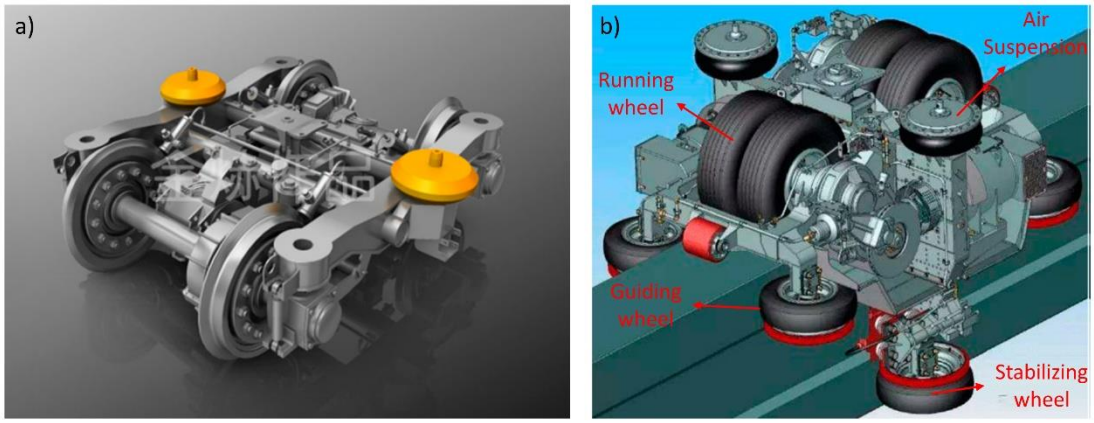

Figure 1.4: Bogie structure, a) bogie of a railroad vehicle, b) bogie of a straddle-type monorail vehicle [Zixue Du et al., 2018].

The main purpose of the suspension system is to provide a high level of ride quality and isolate the vehicle from road surface irregularities. In the design of vehicle suspension systems, there is a trade-off between driving comfort and road-holding ability. With a passive suspension system, improving the ride quality and handling at the same time has limitations. Therefore, active and semi-active suspension control strategies have been studied by many researchers in the field of vehicle dynamics [Koch and Kloiber, 2014], [Sammier et al., 2003], [Du et al., 2005], [Sun et al., 2013].

Due to the high energy consumption and expensive components, active control has not widely used in vehicle suspension systems. At this point, semi-active devices have recently been widely concerned as one of the promising devices for a vehicle suspension system. Also, low energy requirement and working as a passive damper in case of no energy supplied to them are advantages of the semi-active dampers over the active components.

There are two semi-active suspension control approaches in the application of the vehicle suspension system as schematically represented in Figure 1.5. First one is the inverse or clipped method [Dong et al., 2009] in which the required voltage is calculated by comparing actual and calculated damper force by the inverse model of the MR damper. In this approach, the actual force should be measured continuously to track the desired force and the inherent nonlinear dynamic of MR damper is not considered in the calculation of the system controller. Therefore, this approach may end up with a force tracking problem. The other one is the direct method [Du et al., 2013] in which control voltage or current is calculated by incorporating the MR damper model into the system controller. In this approach, the issues relating to practical implementation costs are eliminated due to the force measuring sensor (load cell) is no longer needed.

Various semi-active control strategies for the system controller have been studied by many researchers in the field of the automobile but studies related to the rail vehicles are relatively few. For example, skyhook control [Sun et al., 2013], [Ha et al., 2013], $H\infty$ control [Zong et al., 2013], [Shin et al., 2014], [Orvnäs et al., 2011], LQG control [Liao et al., 2003], backstepping control [Fukao et al., 2002]. However, controlling the translation and rotational dynamics of the monorail vehicle with semi-active devices is a new research area. Another issue to be considered in a vehicle system is the parametric uncertainties of the vehicle model which have effects on the dynamic response of the vehicle. In such uncertainties, the vehicle weight depends on

the number of passengers and the property of the suspension system is changed with time due to the heating of the damper. These uncertainties should be considered when designing system controllers.

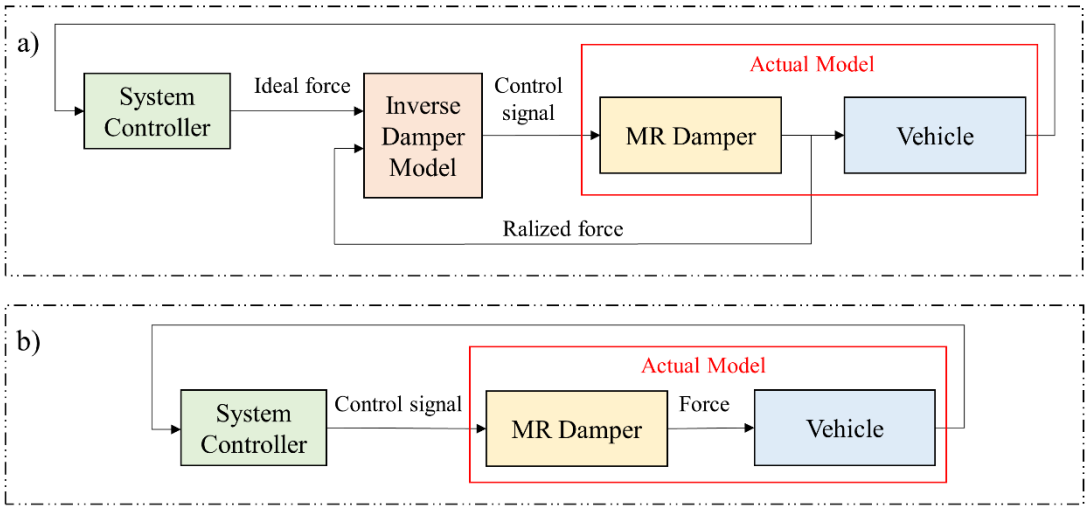

Figure 1.5: Semi-active control approaches.

Besides the aforementioned suspension performance criteria, the suspension working space must be restricted in practice to avoid mechanical damage and deterioration in comfort. To deal with such a restriction, multi-objective control approaches have been presented in the literature for active control of the suspensions [Lin J-S and Kanellakopoulos, 1997], [Huang et al., 2015]. For an output constraint system, the design of barrier Lyapunov function (BLF) is an effective method [Sun et al., 2014], [Tee et al., 2009]. In the BLF approach, the conventional quadratic Lyapunov function (QLF) is replaced by a BLF which has the property of growing to infinity at some finite limit. This enables the controller to switch between the desired performance criteria.

1.3. Previous Studies Related to Monorail Vehicles

Various studies have been carried out to elucidate the dynamic behaviour of monorail vehicles with respect to different aspects including the vehicle modelling by considering different operation conditions, tire wear properties and monorail train-guideway interaction. In literature, there are few types of research on the dynamic behaviour of the monorail systems under the different segment of the guideway,

particularly on the suspension control units. Modelling related studies are summarized as follows:

Zhou et al. conducted a dynamic parameter optimization study that focuses on the curve negotiation properties, comfort and tire eccentricity of a straddle-type monorail vehicle. In the mentioned study, the curve negotiation properties after the optimization are increased by 18.93 %, and the comfort is increased by 22.85 % and the tire eccentric wear is reduced by 41.33 % after optimization [Zhou et al., 2019].

Jiang et al. examined the main reason of abnormal vibration occurs in Chongqing monorail line, that causes the vehicle to exceed the comfort standard. From the frequency domain analysis, they concluded that abnormal vibration caused by wheel out of round can only be reduced by increasing the vertical stiffness of the air spring and car body mass [Jiang et al., 2019].

Ji and Ren proposed a method for determining the preload pressure of stabilizing wheels based on the critical roll angle of straddling monorail vehicles. Also, they specified the maximum and the minimum negotiation speed limits for a monorail with single-axle bogie vehicle by using the preload pressure values to ensure the reliable anti-overturning capacity of the vehicles [Ji and Ren, 2018].

Jiang et al. introduce two types of articulated monorails named non-bolster and bolster type. They compared the dynamic properties of two types of articulated monorails by using the load reduction rate and overturning coefficients criteria's when vehicles pass a curve. They concluded that the ''non-bolster type'' structure will be a better choice for vehicles passing a small radius curve [Jiang et al., 2018].

Maciel and Barbosa considered the three degrees of freedom monorail vehicle. They studied the combination of linear and nonlinear cornering stiffness and slip velocities to calculate tire forces at contact points under the misalignment of the guideway inputs [Maciel and Barbosa, 2016].

Zhao et al. surveyed the riding stability of straddle- type monorail vehicles under the lateral wind condition by means of the multi-body dynamics analysis software Adams. They arrived at a conclusion that changes of car speed and wind speed can exert a great influence on the transverse acceleration of straddle-type monorail vehicles affected by lateral wind, and an excessive speed of vehicle [Zhao, 2014].

Goda et al. developed a curving simulation algorithm for a monorail car by using a moving coordinate system. In the simulation structure, the radial force of all tires and the side force of the running tire are considered. They conceded that the yaw moments

generated by the guiding tire on the leading truck were larger than those on the trailing truck. Thus, it is important to evaluate the leading guide tire radial force on the leading truck to design the lightweight truck frame and the guideway [Goda, 2000].

Monorail-guideway interaction related studies can be summarized as follows:

Cai et al. developed a coupled dynamic model of the suspension-type monorail vehicle-bridge system to evaluate the dynamic responses of the model. The simulation results are compared with the field test data. They remark that the box-beam bridge with an open bottom has lower vertical and lateral stiffness than those of straddle monorail bridge and subway bridge. Therefore, the bridge can produce larger displacement and acceleration compared with the traditional railway bridge. Also, the proposed model may consider periodic variations of the driving and guiding forces due to the flexible bridge, it can be helpful to suggest a more reasonable initial compression force of the guiding tire for better running stability [Cai et al., 2019].

Wang and Zhu derived a new steel-concrete composite track beam-train interaction system, that can simulate the slip phenomenon for the monorail vehicle and obtained results are verified by comparing the calculations with field-test data [Wang and Zhu, 2018].

Wang et al., proposed an analytical procedure of dynamic interaction analysis of the straddle monorail bridge–vehicle coupling system. The effects of speed, three kinds of loads and different radius of curvature on dynamic responses of the monorail bridge–vehicle coupling system are analyzed. It is observed that the maximum lateral vibration amplitude is 0.075 mm with respect to the radius of 1000 m, while the maximum vertical vibration amplitude is 0.43 mm with respect to the radius of 100 m. Also, the vibration amplitude of the track beam in the lateral and vertical direction increases as the driving speed increases as, the maximum vertical deflection is 0.69 mm, while the maximum lateral amplitude is 0.046 mm, at the speed of 80 km/h [Wang et al., 2017].

Lee et al. investigate the traffic-induced vibration analysis of a monorail bridge and train considering track roughness to evaluate the riding comfort of trains. They conclude that the occurrence of the resonance in the vertical and lateral direction is low. Also, the amplitude of the bridge dynamic response is increased with the speed and decreased according to the passenger loading. Finally, it is stated that the riding comfort of the monorail train can be categorized as good by ISO 2631 [Lee et al., 2005].

1.4. Scope and Contribution of the Thesis

The dynamic behaviour of the monorail vehicles is influenced by the vehicle design parameters, particularly the suspension and the guideway on which the vehicle runs. Due to the small lateral span of the running wheel and guideway, monorail vehicles cannot provide sufficient anti-overturning capacity and show tendency to instability. Motivated by these observations, a new barrier Lyapunov function (BLF) based constrained adaptive backstepping controller was proposed for the monorail suspension system and effectiveness of the controller was tested on both the experimental setup and co-simulation structures. Also, an uncertain robust control and a quadratic Lyapunov function (QLF) based adaptive control that includes parametric uncertainty both system and suspension parameters was designed. In this thesis, straight, transition and circular stages of a track were designed, and a full turn of a monorail vehicle was simulated.

The proposed control approaches are model-based controller, therefore, the dynamic model of the monorail vehicle that includes a tire model should be established. In the context of thesis, a 15 DOF (Degree of freedom) model is constructed and the validity of the model is tested by a multibody simulation software under various track beam curvature and vehicle travelling speed condition.

To increase the performance of the system controller and taking full advantage of the MR dampers, mathematical model parameters values of the damper should be known or estimated. Therefore, a parameter identification setup was constituted for the estimation of the parameter values of a MR damper. By this way, the effectiveness of the model-based control approaches was increased.

Vehicle dynamic response is greatly affected by environmental factors such as track surface roughness, varying vehicle speed, lateral wind condition and also tire pre-pressure value. These factors should be considered in the selection of vehicle parameters and suspension control design. The relation between the pre-pressure of guiding, stabilizing wheels and the unbalanced lateral acceleration was constituted to specify the initial pre-pressure value. The surface irregularities of the monorail track surface were classified according to ISO 8608 standards. More realistic road surface specification brings more reasonable assessment about the travelling comfort and safety criteria.

Due to the structural difference of the monorail bogies, partial abrasion occurs on running tires. These unevenly wear result from the load transfer between the inner and outer wheels that arise from running on the various radius of curve including small radius. Also, the side slip of the running tire causes partial abrasion. Thanks to the designed controllers, the lateral displacement and the roll angle of the bogie are decreased. This decrement may also provide an extended service life to running tires and lower tire wear.

The nonlinear tire dynamics are not considered, tires are modelled as a linear spring with viscous damping by taking into considerations the parametric uncertainties that corresponding to tire wear. Also, vehicle body weight is assumed 10 % of its nominal value in suspension control design that corresponding to the difference between operating in full capacity and no passenger cases. The obtained results are promising for the possible implementation of such a semi-active suspension component in the bogie structure of the monorail vehicles.

1.5. Structure of the Thesis

This thesis is organized as follows. In Chapter 2, a monorail vehicle with its subsystems is described from the modelling point of view. Also, the MR damper characterization setup and the critical design parameter of the monorail vehicle are presented. The robust control design procedure that deals with the uncertain system and MR damper parameters are given in Chapter 3. The novel constrained adaptive backstepping control design scheme and stability analysis are discussed in Section 4. The test rig utilized for the controller performance evaluation is introduced, and experimental results are discussed in Section 5. Constructed co-simulation structure is presented for the effectiveness of the proposed semi-active control strategies in Section 6. Finally, some concluding remarks, challenges and future prospects of the proposed suspension structure are given in Section 7.

2. MODELLING OF THE STRADDLE-TYPE MONORAIL VEHICLES

Straddle type monorail vehicle runs on rubber tires that straddle a single concrete guideway beam and has three types of tires as shown in Figure 2.1. The running tire is the main component of the bogie and provides longitudinal motion. Guide tires at the four corners of the bogie and stabilizing tires at the two sides of the bogie, lead the car body along the guideway [Goda et al., 2000]. Also, stabilization tires prevent excessive rolling motion of the vehicle. Traction power is supplied by power rail installed at both sides of the guideway.

In this study, a 15 degree-of-freedom vehicle model is constituted. In the context of modelling structure, vertical, lateral and rotational dynamics of the monorail vehicle are considered, and the longitudinal dynamics are neglected because of the constant speed assumption. In modelling approach to monorail vehicle, there are three main factors, these are tire modelling, guideway design and produced centrifugal forces arising from guideway curved segments. In this chapter, all these effects are examined, and the reliability of the constructed model was validated with the help of the multibody simulation program package Universal Mechanism (UM) developed in Bryansk State Technical University [Wu et al., 2018].

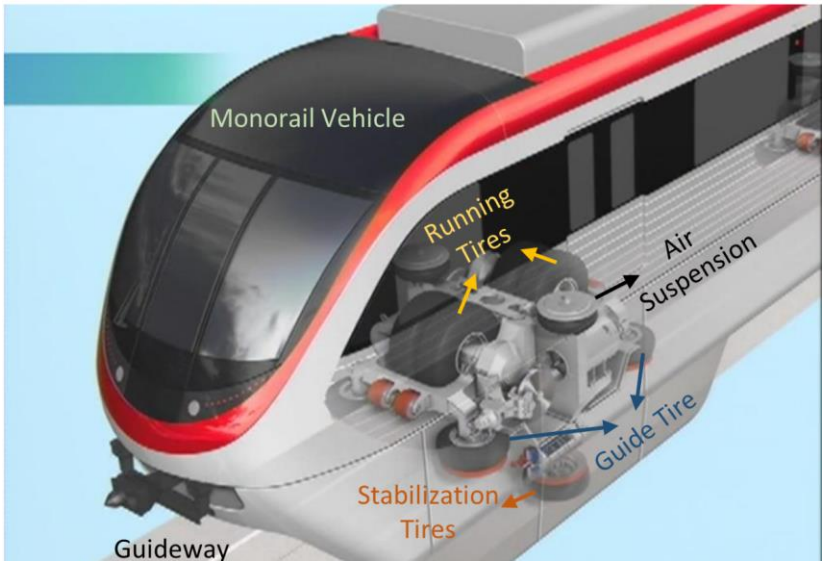

Figure 2.1: Illustration of the straddle type monorail vehicle [Web 2, 2019].

2.1. Tire Modelling Approaches

Tires are the most critical part of the monorail vehicles as they establish the only contact between the bogie and the guideway. Therefore, the tires have a significant impact on vehicle performance characteristics such as ride comfort and handling. There are different tire modelling approaches in the literature that depends on the complexity of the system to be examined. Also, the selected model should correctly represent the interaction between tire and road surface. In practice, tires are in contact with the road surface at many points while the wheel is moving, therefore, the enveloping problem is arising when the road disturbances have short wavelengths. These modelling structures are given in Figure 2.2.

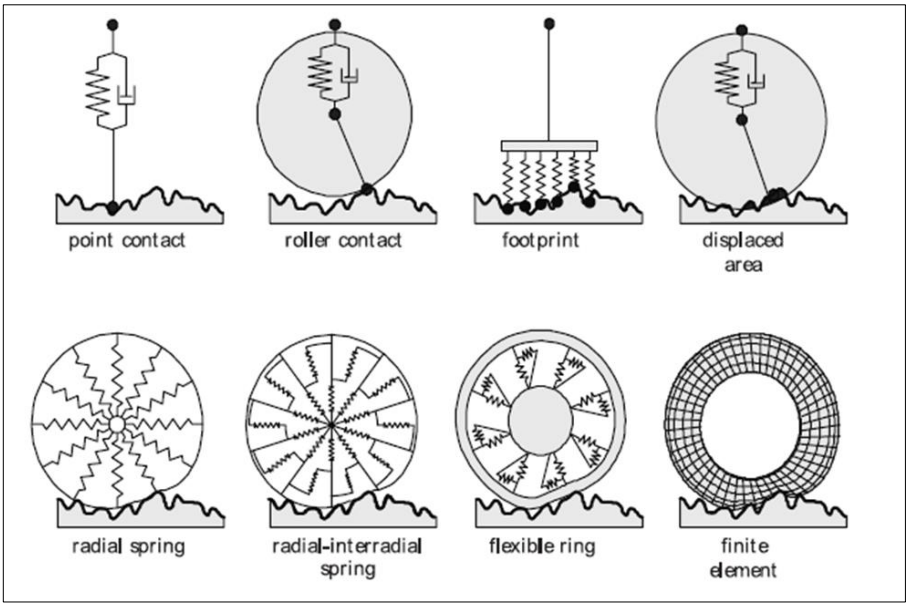

Figure 2.2: Tire enveloping models [A. Schmeitz, 2004].

Evaluating vehicle handling and comfort performance for low-frequency and steady-state vehicle motions on large-wavelength road profiles, semi-empirical Magic tire model [Pacejka, 2005] and FIALA [Fiala, 1954] tire model widely used to calculate steady-state tire force and moment characteristics. These models require wheel longitudinal slip, lateral slip and vertical forces as an input to calculate the longitudinal force, lateral force and the aligning torque. As shown in Figure 2.3, the lateral slip of a tire is defined by an angle between the direction of wheel travel and the direction of wheel heading. Longitudinal slip is the ratio of wheel speed to contact

point speed. Aligning torque is produced due to the pneumatic trail that caused by non-proportional lateral force distribution.

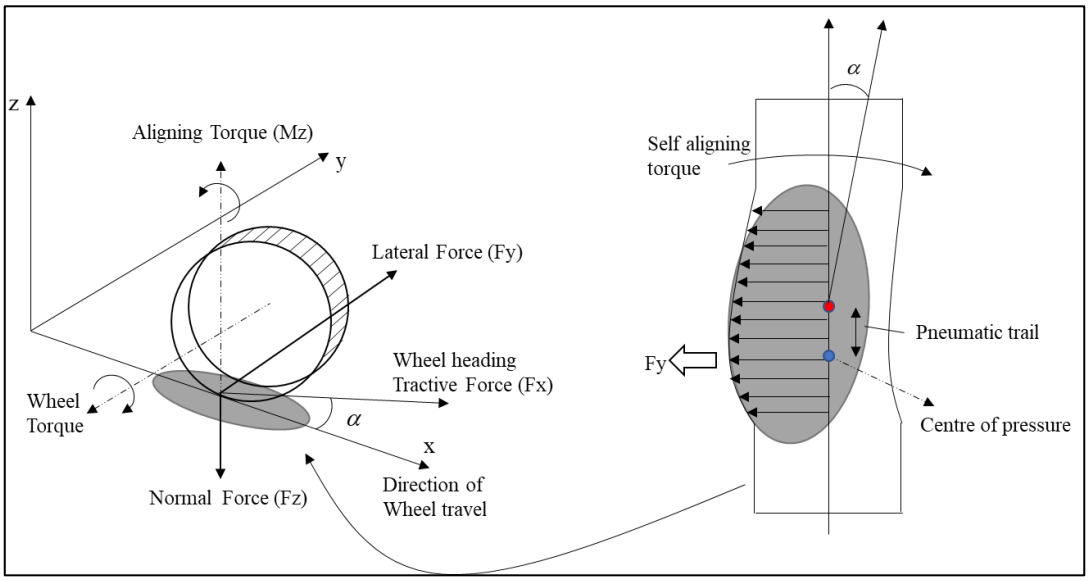

Figure 2.3: Tire forces and rotation.

Magic Formula: The general form of the Magic Formula is given in equation (2.1) and summarized in Figure 2.4. Camber effect is not considered in this model.

$$Y(\chi) = D\sin\left[C\tan^{-1}\left\{B\chi - E\left(B\chi - \tan^{-1}(B\chi)\right)\right\}\right] + S_v$$
$$\chi = x + S_h \tag{2.1}$$

Here $Y(\chi)$ can be longitudinal, lateral force or aligning moment, and χ stands for the longitudinal slip ratio and lateral slip and the rest of factors are curve fitted parameters that should be selected with respect to tire data for the corresponding value.

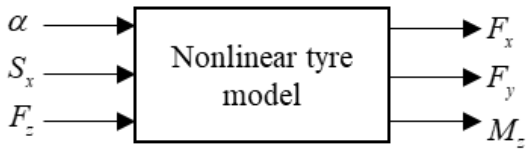

Figure 2.4: Overview of the structure of the tire model.

FIALA tire model: In FIALA tire model, the produced force and moment is calculated depending on the tire state. In working condition, tires could be in Elastic Deformation State or Complete Sliding state. Equation (2.2) is used for the vertical force,

$$\begin{matrix} F_z = -k_z \Delta r - d_z V_{\Delta r} \\ F_z = 0 \end{matrix} \quad if \begin{cases} \Delta r < 0 \\ \Delta r > 0 \text{ or } F_z < 0 \end{cases} \tag{2.2}$$

Tire damping constant in the vertical direction can be written as $d_z = 2\beta_z \sqrt{mk_z}$. Here, Δr represent tire deflection which is defined by $\Delta r = \left(F_{tot} / k_z\right) - \delta_{static}$. To determine which state the tire is in, a critical longitudinal slip and lateral slip ratio is first calculated as the following equation

$$\begin{aligned} S_x^{\ *} &= \frac{\mu F_z}{2C_x} \\ S_y^{\ *} &= \frac{3\mu F_z}{C_y} \end{aligned} \tag{2.3}$$

Longitudinal force equation becomes as

$$\begin{matrix} F_x = C_x S_x \\ F_x = sign\left(S_x\right)\left[\mu F_z - \dfrac{\left(\mu F_z\right)^2}{4\left|S_x\right| C_x}\right] \end{matrix} \quad if \begin{cases} \left|S_x\right| < S_x^{\ *} \\ \left|S_x\right| \geq S_x^{\ *} \end{cases} \tag{2.4}$$

where C_x is the longitudinal slip stiffness value, lateral force equation is given as,

$$\begin{matrix} F_y = \mu F_z \left(1 - h^3\right) sign\left(S_y\right) \\ F_y = \mu F_z sign\left(S_y\right) \end{matrix} \quad if \begin{cases} \left|S_y\right| < S_y^{\ *} \\ \left|S_y\right| \geq S_y^{\ *} \end{cases} \tag{2.5}$$

where h is defined as $h = \left(1 - \left(C_y \left|S_y\right|\right) / \left(3\mu F_z\right)\right)$.

Monorail vehicles are designed considering some comfort and riding safety criterions. For example, lateral unbalanced acceleration should be less than tolerable limits for comfort and, also travelling speed is restricted due to safety limitations. When these limits are regarded, the tire model can be assumed as a linear model. As the sideslip angle of the running tire does not exceed 3˚-5˚ in real application [Goda, 2002]. Therefore, lateral force and aligning torque can be accepted almost linear with the lateral slip angle. As given in Figure 2.5, linear tire model is tested with FIALA tire model under the different radial forces and the tire slip angles. The resulting force output for both the Magic Formula and the FIALA model are given in Figure 2.6.

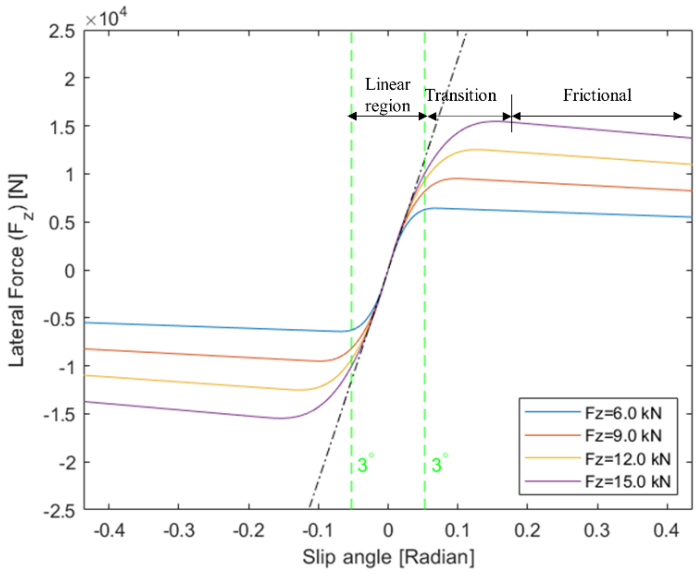

Figure 2.5: Lateral force and slip angle relation.

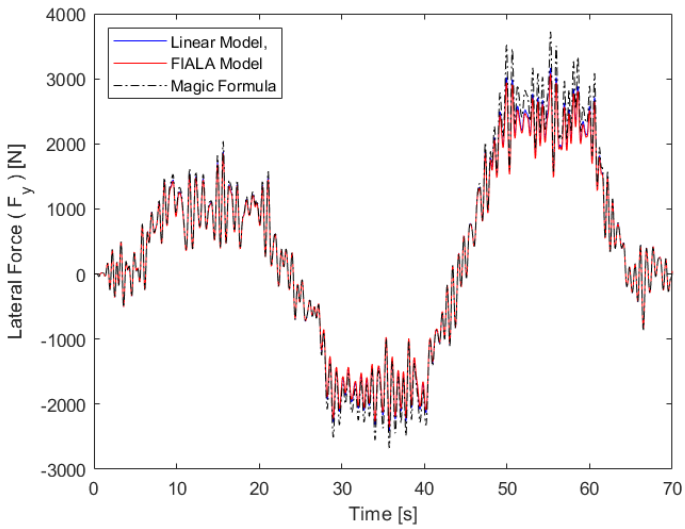

Figure 2.6: Lateral force comparison.

2.2. MR Damper Parameter Identification

The most effective use of the potentials provided by MR dampers depends on the realistic expression of their dynamic behaviour. Control approaches based on the mathematical model of MR damper provide certain advantages in control applications. MR dampers have nonlinear dynamics and contain hysteresis. Their nonlinear structure is resulting from the fact that the force output of the damper is a nonlinear function of electrical input and mechanical excitations. Their hysteresis structure is resulting from the fact that the force output does not only dependent on the current values of the inputs but also depends on the output history.

The selected mathematical model that required to reflect these two characteristics closely affects the effectiveness of the control design to be performed. Several models have been developed to describe the intrinsic behaviour of the MR damper. Therefore, the mathematical model for describing the intrinsic behaviour of the MR damper has been the subject of many studies [Spencer, 1997], [Kwok, 2006], [Xia, 2003]. These models are classified as the parametric and non-parametric models. Non-parametric models are able to model the MR damper behaviour in such a way that the model consists of polynomials which do not have physical meanings. A model expressing the force as a six-degree polynomial function of velocity, with current-dependent coefficients, was introduced to study the dynamical behaviour of MR damper by [Choi, 2001]. The predicted results of this model showed that the model adequately predicts the non-linear force-velocity hysteresis loop of the MR damper.

A literature survey would indicate that, although non-parametric models can effectively represent MR damper behaviour, they are highly complicated and demanding massive experimental datasets for model validation [Şahin, 2010]. Parametric models, on the other hand, consist of some mechanical elements such as linear viscous, friction, springs, etc. The parameters of these elements are estimated by experimental studies [Jimenez, 2005], [Gamota, 1991]. In the parametric MR damper modelling approaches, modified Bouc-Wen model has been used extensively for modelling hysteretic behaviour. The model can predict the nonlinear behaviour of the MR damper over a wide range of operating conditions under various input voltage levels, however, it has 14 model parameters needs to be identified. In addition, inversion of the mathematical model of MR damper can be needed to determine the

required control voltage/current signal in semi-active control applications. These weaknesses make the Bouc-Wen model difficult to use in control design and parameter adaptation schemes. An alternative parametric modelling is the LuGre friction model [Terasawa, 2004], [Sakai, 2003]. The damper model based on the LuGre friction model has a relatively simple structure and the number of model parameters can also be reduced. Therefore, the LuGre friction model enables us to do a nonlinear control application and carry out parameter estimation. Modified dynamic LuGre friction model is defined as follows [Sakai, 2003]

$$f = \sigma_a z_{mr} + \sigma_0 z_{mr} v + \sigma_1 \dot{z}_{mr} + \sigma_2 \dot{x}_{mr} + \sigma_b \dot{x}_{mr} v \tag{2.6}$$

$$\dot{z}_{mr} = \dot{x}_{mr} - a_0 \left| \dot{x}_{mr} \right| z_{mr} \tag{2.7}$$

Here, x_{mr} and $\dot{x}_{mr}$ variables represent the relative displacement and velocity between the rod head and bottom side of the MR damper, respectively. The model contains an internal state z_{mr} which can be interpreted as the MR fluid deformation and v represents the control input voltage to the MR damper. The internal state z cannot be externally measured because of MR fluid enclosed within the damper cylinder. Therefore, its estimated value should be used. For control design purposes, the force equation given in equation (2.6) can also be written in the following form

$$f = \begin{bmatrix} z & vz & -\left|\dot{x}_{mr}\right| z \end{bmatrix} \begin{bmatrix} \sigma_a \\ \sigma_0 \\ \sigma_1 a_0 \end{bmatrix} + \begin{bmatrix} \dot{x}_{mr} & \dot{x}_{mr} v \end{bmatrix} \begin{bmatrix} \sigma_1 + \sigma_2 \\ \sigma_b \end{bmatrix} \tag{2.8}$$

where z_{mr}, v and $\dot{x}_{mr}$ are the vectors whose elements correspond to each MR damper value, equation (2.8) can be rewritten as

$$f = \rho_1 \theta_1 + \rho_2 \theta_2 \tag{2.9}$$

Here, MR damper parameter vectors θ_1, θ_2 and the input signals ρ_1, ρ_2 are defined as

$$\rho_1 = \begin{bmatrix} z & vz & -\left|\dot{x}_{mr}\right| z \end{bmatrix} \quad \rho_2 = \begin{bmatrix} \dot{x}_{mr} & \dot{x}_{mr} v \end{bmatrix} \tag{2.10}$$

$$\theta_1 = \begin{bmatrix} \sigma_a & \sigma_0 & \sigma_1 a_0 \end{bmatrix}^T \quad \theta_2 = \begin{bmatrix} \sigma_1 + \sigma_2 & \sigma_b \end{bmatrix}^T \tag{2.11}$$

An estimate of the force expression defined in equation (2.9) would be in the form $f = \hat{\rho}_1 \hat{\theta}_1 + \rho_2 \hat{\theta}_2$. Here, the uncertain parameter vectors, $\hat{\theta}_1$, $\hat{\theta}_2$ and the auxiliary vectors $\hat{\rho}_1$ and ρ_2 can be defined as:

$$\begin{gathered} \hat{\rho}_1 = \begin{bmatrix} \hat{z}_{mr} & v\hat{z}_{mr} & -|\dot{x}_{mr}|\hat{z}_{mr} \end{bmatrix} \qquad \rho_2 = \begin{bmatrix} \dot{x}_{mr} & \dot{x}_{mr} v \end{bmatrix} \\ \hat{\theta}_1 = \begin{bmatrix} \hat{\sigma}_a & \hat{\sigma}_0 & \hat{\sigma}_1 a_0 \end{bmatrix}^T \qquad \hat{\theta}_2 = \begin{bmatrix} \hat{\sigma}_1 + \hat{\sigma}_2 & \hat{\sigma}_b \end{bmatrix}^T \end{gathered} \tag{2.12}$$

Finally, estimated force expression can be written as

$$\hat{f} = \hat{\theta}_{11} z - \hat{\theta}_{13} |\dot{x}_{mr}| \hat{z} + \hat{\theta}_{21} \dot{x}_{mr} + \left(\hat{\theta}_{12} z + \hat{\theta}_{22} \dot{x}_{mr} \right) v \tag{2.13}$$

To obtain MR damper parameters, some experiments studies were conducted, the force produced by the MR damper was measured while the random displacement input and the bump input was applied as an excitation source. The MR damper parameter identification setup and its components are shown in Figure 2.7. In general, the identification of the MR damper parameter is performed by using small vibration amplitudes and constant current/voltage levels. However, selected parameters may fail in case of large amplitude and fast-changing voltage inputs. Therefore, selected model parameters were tested under the condition of the fluctuating voltage and excitation amplitude. These cases can be considered as the worst case to determine the real force response of the MR damper.

As seen in Figure 2.8.a), selected displacement input to the MR damper is close to the limit of the MR damper working space. There is a little difference between real and simulation force response of the MR damper in case of bump input and random stage as seen in Figure 2.8.c). Employed parameters to describe the MR damper and mechanical linkage of experimental setup may cause this difference. In addition, small peaks are observed in the force response because of the sensor noise. Obtained parameters in the identification procedure for the MR damper model are given in Table 2.1.

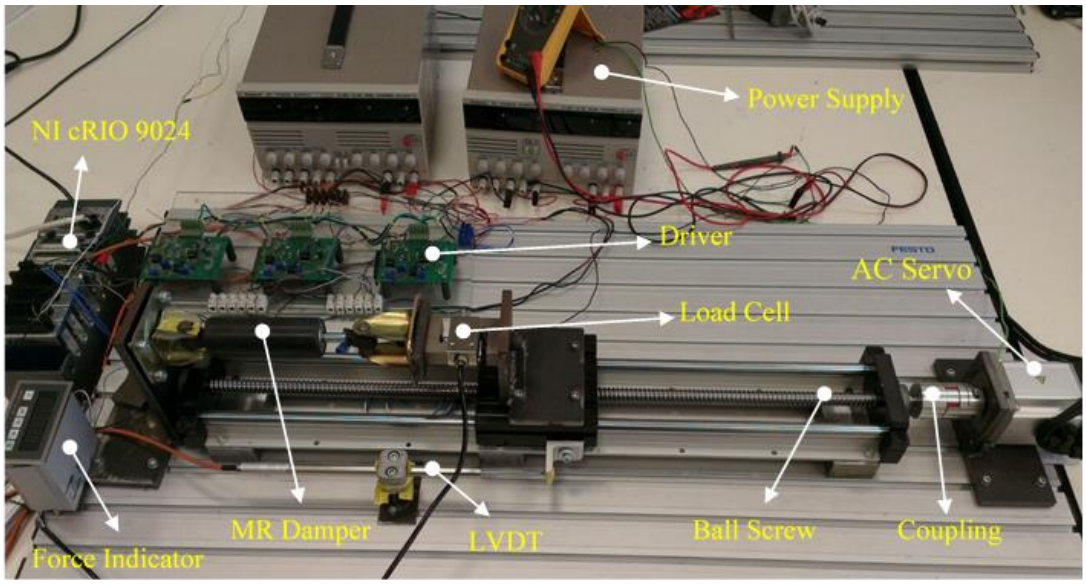

Figure 2.7: MR damper parameter identification setup components.

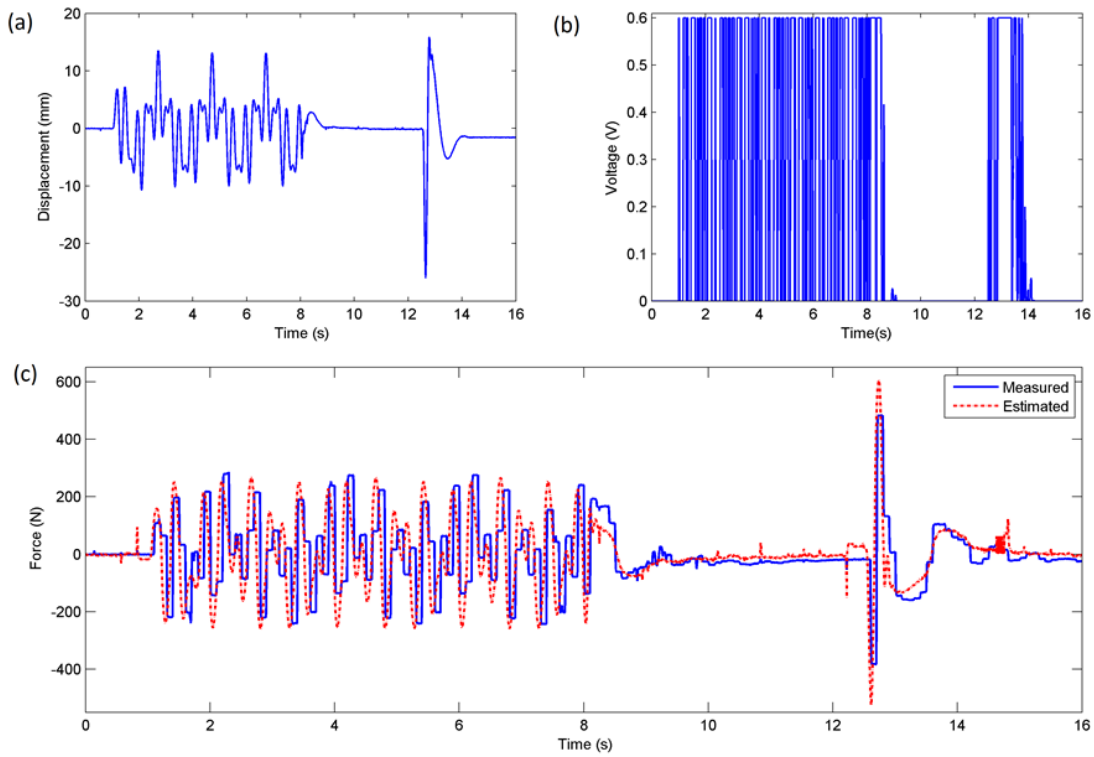

Figure 2.8: MR damper parameter identification: a) Displacement input b) Voltage to MR damper, c) Force responses of MR damper.

The various mathematical models for the MR dampers used in literature were investigated in detail in the Reference [Yıldız, 2013].

Table 2.1: Experimentally obtained values for the MR damper parameters.

Parameters	Definitions	Values	Units
σ_0	Stiffness of $z(t)$ influenced by $v(t)$	320000	N/(m.V)
σ_1	Damping coefficient of $z(t)$	3.21	N.s/m
σ_2	Viscous damping coef. influenced by $v(t)$	1153.3	N.s/m
σ_a	Stiffness of $z(t)$	10000	N/m
σ_b	Viscous damping coef. influenced by $v(t)$	315	N.s/(m.V)
a_0	Constant value	1400	V/N

2.3. Road Profile Design

Railway routes are defined in two fashions. First one is its horizontal (X-Y) plane design and the second one is the vertical profile that includes elevation, rise and fall segments. To design a road profile that will be used in dynamic simulation track centerline should be parameterized by a variable Υ that describes track distance covered by the vehicle. Thus, all road inputs to tires can be defined by using a single parameter.

Also, a moving coordinate system is usually used in the curving simulation of a rail vehicle [Pombo and Ambrósio, 2003], [Shaltout et al., 2015]. In this approach, the position of the coordinates is defined with respect to the track centerline. In literature, there are some track centerline parameterization methods such as analytical segments, and cubic splines [Shaltout et.al, 2015]. In analytical segments procedure, the track is built using a combination of straight, transition and circular curve segments. In straight-line stage, vehicle firstly runs on the straight route without superelevation, then the clothoid curve which has gradually increased superelevation and radius is used as a transition curve stage. Finally, the vehicle enters a circular curve stage that has a constant radius of curvature and superelevation.

When the monorail vehicle passes through the curve, the centrifugal force pushes the whole vehicle system to the outside. This phenomenon causes lateral acceleration which inversely effects comfort. To eliminate or reduce lateral acceleration the outer part of the guideway is raised thus, a component of the gravitational force (weight) has been effectively used [Iwnicki, 2006]. In addition, the clothoid curves enable a gradual transition in lateral acceleration. The track centerline position in the global coordinate system can be defined by equation (2.14) with respect to road distance Υ.

$$p_T(\Upsilon)=\begin{bmatrix} x_t(\Upsilon) \\ y_t(\Upsilon) \\ z_t(\Upsilon) \end{bmatrix}=\begin{bmatrix} \Upsilon-\frac{1}{10}\frac{\Upsilon^5}{\pi^2}\kappa^2 \\ \frac{1}{6}\Upsilon^3\kappa-\frac{1}{84}\frac{\Upsilon^7}{\pi^2}\kappa^3 \\ \frac{h_{\max}-h_{\min}}{l_{clo}}\Upsilon \end{bmatrix} \tag{2.14}$$

where κ is a constant and it can be calculated as $\kappa=1/(l_{clo}R)$. Here, l_{clo} is the length of the transition stage, $h_{\max}$ and $h_{\min}$ are the initial and final super elevation value of the stage, respectively. Also, the length of the transition curve of straddle-type monorails shall not be less than the value calculated by the following formula that is specified by Technical Regulatory Standards on Japanese Railways, [Web 1, 2019].

$$l_{clo}=\frac{V^3}{14R} \tag{2.15}$$

Here, $V=4.62\sqrt{R}\sim 4.65\sqrt{R}$ is the maximum speed of the train travelling on the curve (unit: km/h) and R represent the curve radius (unit: m). In the circular curve stage, circular road components can be defined as [Shaltout et al., 2015],

$$p_C(\Upsilon)=\begin{bmatrix} x_{cir}(\Upsilon) \\ y_{cir}(\Upsilon) \\ z_{cir}(\Upsilon) \end{bmatrix}=\begin{bmatrix} \left(\sin(\Upsilon/R+\Phi_i)-\sin(\Phi_i)\right)R+x_i \\ \left(-\cos(\Upsilon/R+\Phi_i)+\cos(\Phi_i)\right)R+y_i \\ h_{t\max} \end{bmatrix} \tag{2.16}$$

The variable Φ_i is the clothoid angle at the end of the transition which is described by

$$\Phi(\Upsilon)=\arctan\left(\frac{dy/d\Upsilon}{dx/d\Upsilon}\right) \tag{2.17}$$

The ratio of superelevation for the straddle-type monorail also specified as the standard value calculated by the following formula, but it cannot be greater than 12 % [Web 1, 2019].

$$i = \frac{V'^2}{1.27R} \tag{2.18}$$

Here, i is the ratio of superelevation (unit: %), V' is the average speed of the train (unit: km/h). The commercial multibody software program (UM) can generate road profile by its related track geometry modules. In Figure 2.9, an example route, that, include 30 m straight, 20 m transition and 100 m circular road with 50 m radius was represented and compared to road horizontal alignment result of the UM software.

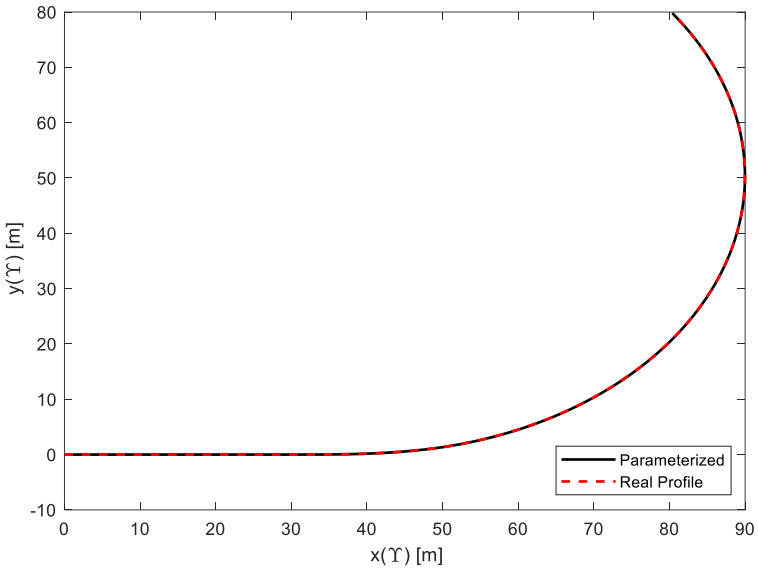

Figure 2.9: Top view of the designed road profile.

Road curvature and elevated road surface profile are given in Figure 2.10. The super-elevation and the radius of curvature are increased in the transition segment before the circular curve stage and decreased after the circular curve.

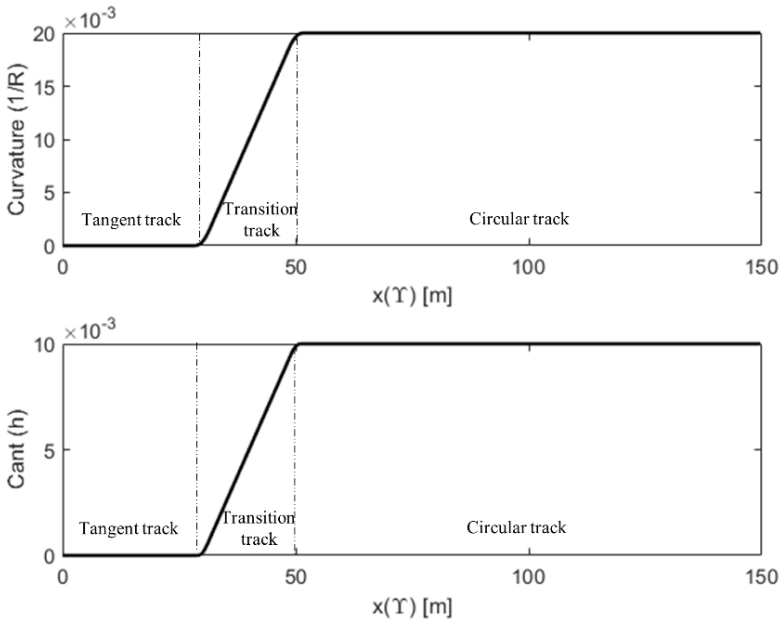

Figure 2.10: Curvature and cant of the road profile.

In the dynamic simulation of the monorail vehicles, lateral displacement on each tire contact surface due to superelevation should be taken into account in addition to horizontal alignment that is explained in the above section. The superelevation arises from bending of the guideway beam with respect to curve direction (e.g. positive cant for right-hand curve). In practice, there are two ways of forming superelevation as given in Figure 2.11. First one is formed by the rotating beam about its centre and the second one is formed by rotating-beam about track centreline as given in Figure 2.11.b). UM software uses the second mode to generate superelevation.

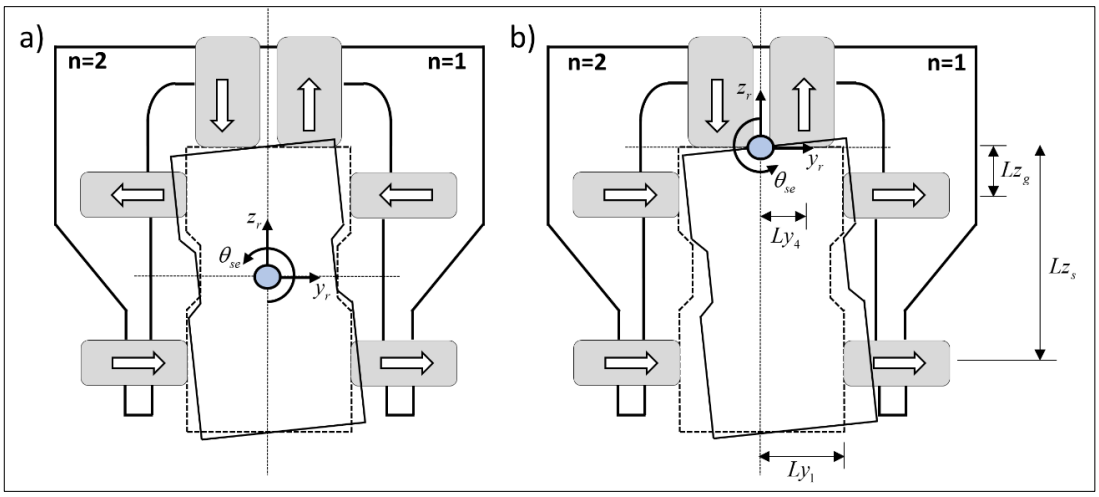

Figure 2.11: Track beam super elevation setting mode.

In the dynamic simulation, road input to the tire model should be defined for each step, regarding the selected mode. For the second mode given in Figure 2.11.b), road excitation for each tire can be defined as

$$z_w = z_r - (-1)^n L_{y4} \sin\theta_{se} + z_{ir}$$
$$y_w = y_r - L_{y4}(1 - \cos\theta_{se}) \tag{2.19}$$

$$z_g = z_r - (-1)^n \left\{ L_{y1} \sin\theta_{se} - (-1)^n L_{zg} (1 - \cos\theta_{se}) \right\}$$
$$y_g = y_r + L_{zg} \sin\theta_{se} + (-1)^n \left\{ L_{y1} \sin\theta_{se} (1 - \cos\theta_{se}) \right\} + y_{ig}$$
$$z_s = z_r - (-1)^n \left\{ L_{y1} \sin\theta_{se} - (-1)^n L_{zs} (1 - \cos\theta_{se}) \right\} \tag{2.20}$$
$$y_s = y_r + L_{zs} \sin\theta_{se} + (-1)^n \left\{ L_{y1} \sin\theta_{se} (1 - \cos\theta_{se}) \right\} + y_{is}$$

Here, subscript w, g and s indicate the running, guiding and stabilizing tire. z_r and y_r stand for horizontal and vertical beam alignment, z_{ir} and y_{ir} defines the road surface irregularities, n denotes the side of the bogie ($n = 1$, left side; $n = 2$, right side).

2.3.1. Guideway Surface Roughness

The surface irregularity profile for the track beam at the running, guiding and stabilizing tire contact surface is the essential excitation sources for the straddle-type monorail vehicles in addition to aforementioned beam movements. Therefore, these irregularity profiles should be defined more realistically for investigating the dynamic performance of the vehicle.

In defining surface irregularity, there are three ways to simulate road spectrum that are random sinusoidal, integral white noise, and noise-shaping filter method. In this study, the random sinusoidal approach is used. ISO 8608 specifies road

classification for longitudinal road profile with respect to the vertical displacement power spectral density (PSD). The drop-in magnitude is modelled by the waviness, w

$$G_d(n) = G_d(n_0)(n / n_0)^{-w} \tag{2.21}$$

the road surface in two-dimensional space is

$$z(x) = \sum_{i=0}^{N} \sqrt{2.G_d(n_0).(n / n_0).\Delta n} \cos(2\pi.n.x + \psi) \tag{2.22}$$

Equation (2.22) can be also written in below form

$$z(x) = \sum_{i=0}^{N} \sqrt{\Delta n}.2^k 10^{-3}(n_0 / n).\cos(2\pi.n.x + \psi) \tag{2.23}$$

where, $k = (\log_2(G_d(n_0)x10^6) + 1) / 2$, $G_d(n)$ is the PSD function, n is the spatial frequency, $n_0 = 0.1$ is the reference spatial frequency. ψ is the random phase angle uniformly distributed from 0 to 2π . G_d is the roughness coefficient that is defined according to the international standard [ISO 8608, Geneva] are given in Table 2.2.

Table 2.2: ISO road roughness classification.

Road Class	$G_d(n_0)(10^{-6}\text{m}^3/\text{cycles})$		Type of Road
	Range	Geometric mean	
A	<32	16	Smooth runway
B	32-128	64	Smooth highway
C	128-512	256	Highway with gravel
D	512-2048	1024	Rough runway
E	2048-8192	4096	Pasture

Typical road profiles can be grouped into classes from A to H and each class categorized by its reference value $G_d(n_0)$. PSDs of the generated random road profiles are given in Figure 2.12 with their related upper bound.

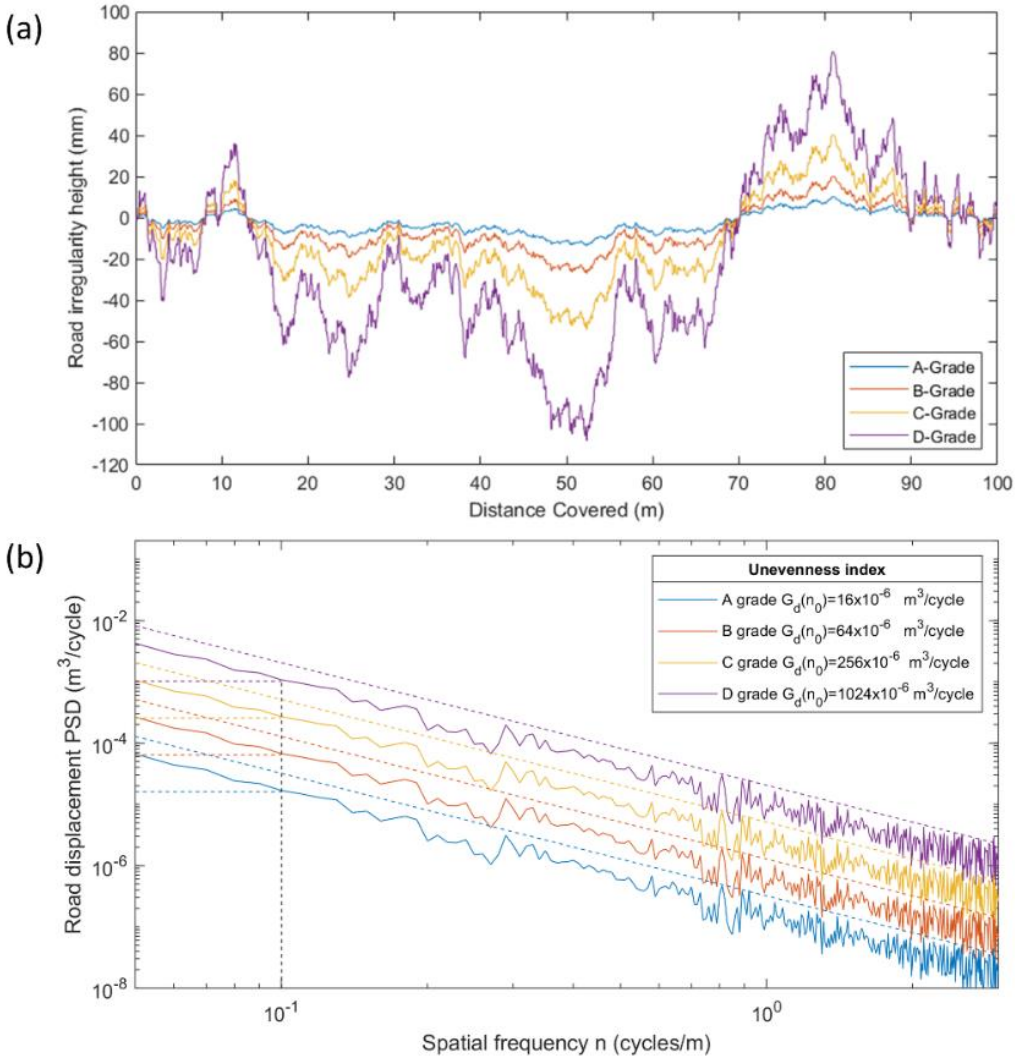

Figure 2.12: a) Simulated road profile, b) PSDs of the used road profiles (solid line) and upper bound (dotted line).

As in highways, to avoid wheel slip and ensure safe operating condition, monorail vehicles are operated on a track beam that should have up to some degree of roughness. International straddle monorail design specifications are still lack of the standard of beam surface irregularity but some studies [Wang, 2018] and [Cai, 2019] include experimental results of track roughness of track beam. In reference [Lee, 2005], the surface roughness of a 44 m steel-concrete composite bridge was measured and simulated by means of a Monte Carlo simulation method using a PSD function as given in equation (2.24).

$$G_d(\Omega) = \frac{\alpha}{\Omega^n + \beta^n} \tag{2.24}$$

Here Ω is the spatial frequency, α, β and n are the roughness coefficient, shape and the power distribution parameter, respectively. These parameters are given as follows,

- Surface of running tires: α = 0.0005, β = 0.35, n = 3.00;
- Surface of guiding tires: α = 0.0006, β = 0.50, n = 2.80;
- Surface of stabilizing tires: α = 0.0006, β = 0.50, n = 2.6.

When the PSD function that defined in equation (2.21) is used, $G_d(n)$ values should be $3x10^{-6}$, $2x10^{-6}$, $1.5x10^{-6}$ for running, stabilizing and the guiding surface, respectively. Simulated and experimentally measured track surface profiles are given in Figure 2.13, Figure 2.14 and Figure 2.15.

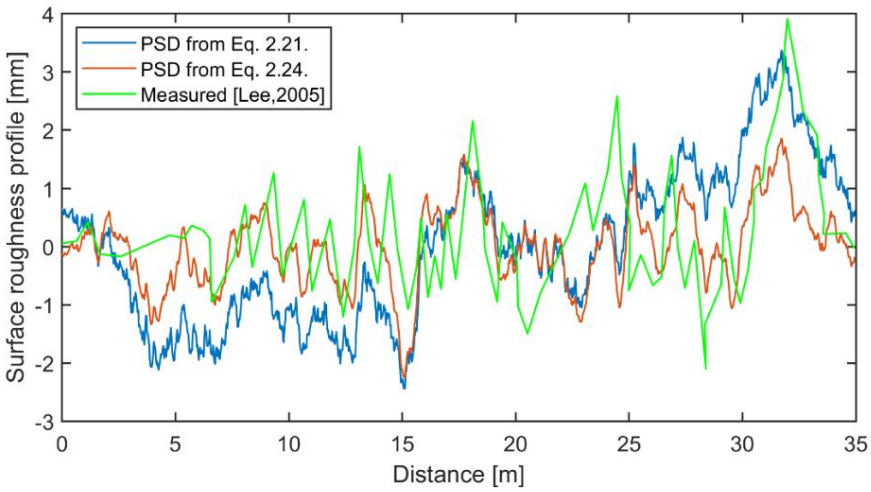

Figure 2.13: Track surface roughness for running tires.

If the results are examined regarding classification of ISO standard, the monorail track surface is in the smooth runway class. Also, using unrealistic road classes may lead to misleading expectations for evaluating the performance of the vehicle components such as secondary suspension or traction control methods. In this respect, modelling of road surface roughness becomes important for the dynamic model of a monorail vehicle.

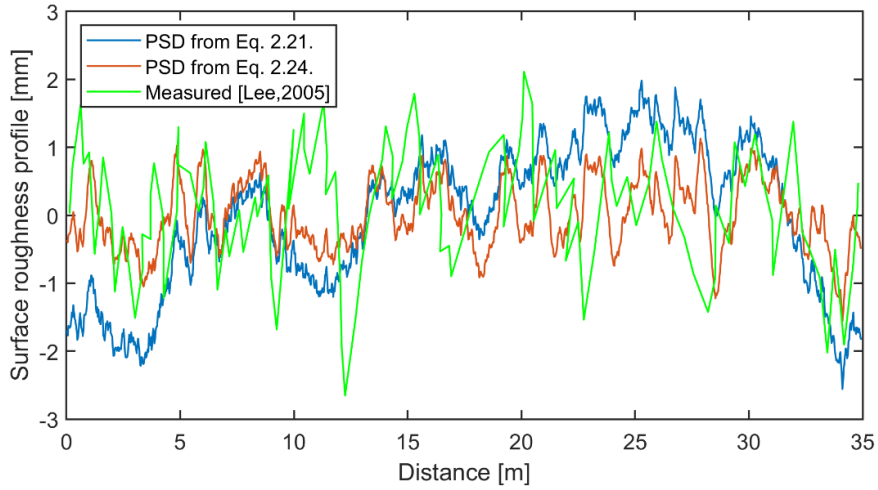

Figure 2.14: Track surface roughness for guiding tires.

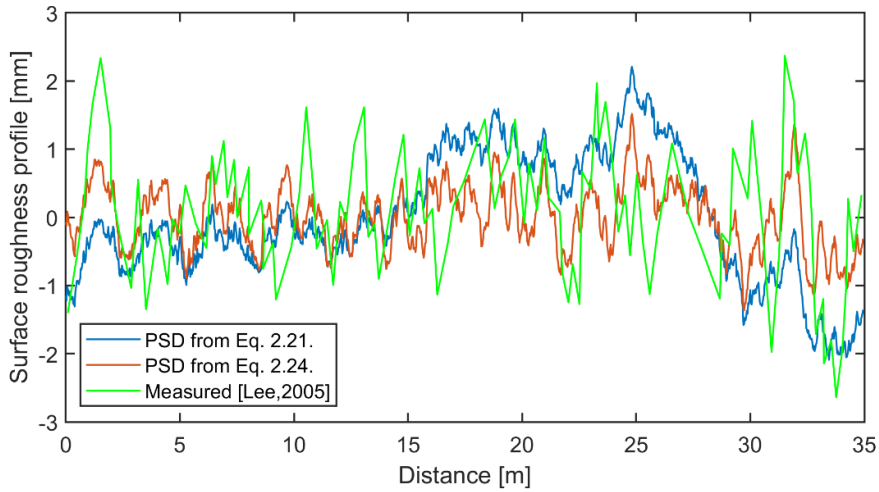

Figure 2.15: Track surface roughness for stabilizing tires.

2.4. The Dynamic Equations for Straddle Monorail Vehicle

The simplification of the vehicle model and the selection of vehicle degrees of freedom are a key issue, and different methods lead to large differences in computational effort and computational accuracy. In this study, it is assumed that the monorail vehicle body and bogies are rigid, and the centre of the masses have the coordinate systems $O_c y_c z_c$ and $O_b y_b z_b$, respectively. The DOF variables of the car body and bogies are presented, the parameters and their description used in the simulation are stated in Table 2.3. Also, the differential equations of motion for the straddle-type monorail vehicle are presented in this subsection. The schematic illustration of the constituted monorail vehicle model is shown in Figure 2.16.

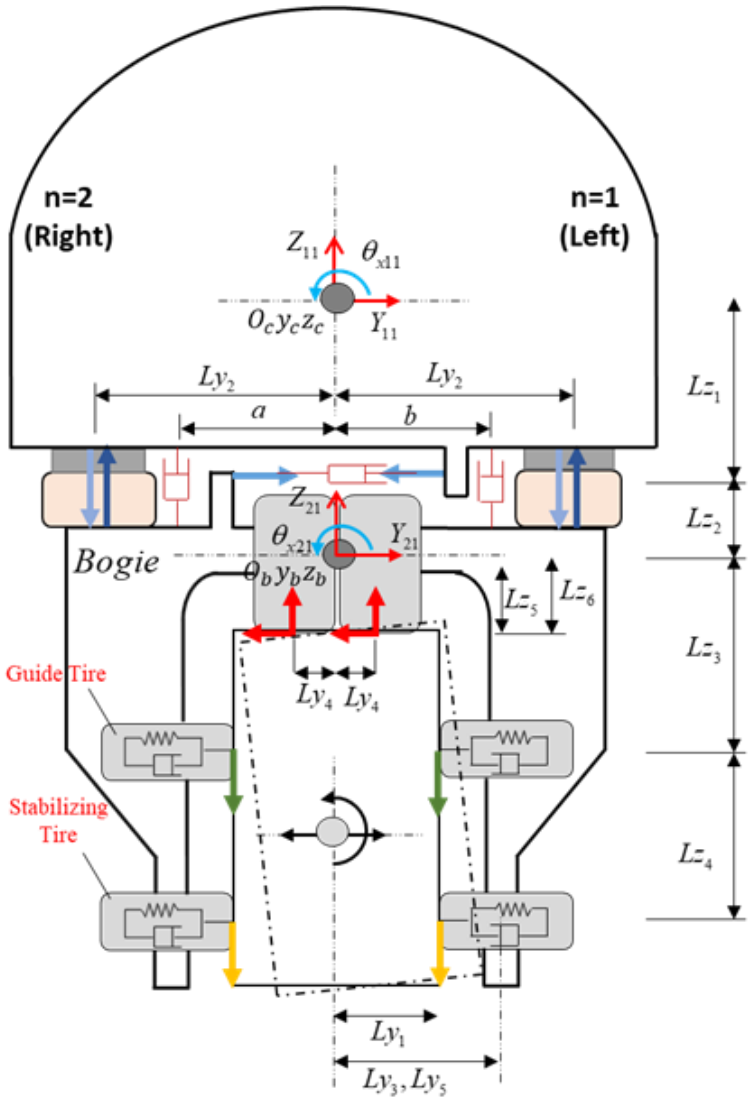

Figure 2.16: Schematic rear view of the idealized monorail vehicle.

Table 2.3: DOF of the vehicle index.

DOF	*Vertical*	*Lateral*	*Yaw*	*Pitch*	*Roll*
Vehicle body	z_{11}	y_{11}	θ_{z11}	θ_{y11}	θ_{x11}
Front Bogie	z_{21}	y_{21}	θ_{z21}	θ_{y21}	θ_{x21}
Rear Bogie	z_{22}	y_{22}	θ_{z22}	θ_{y22}	θ_{x22}

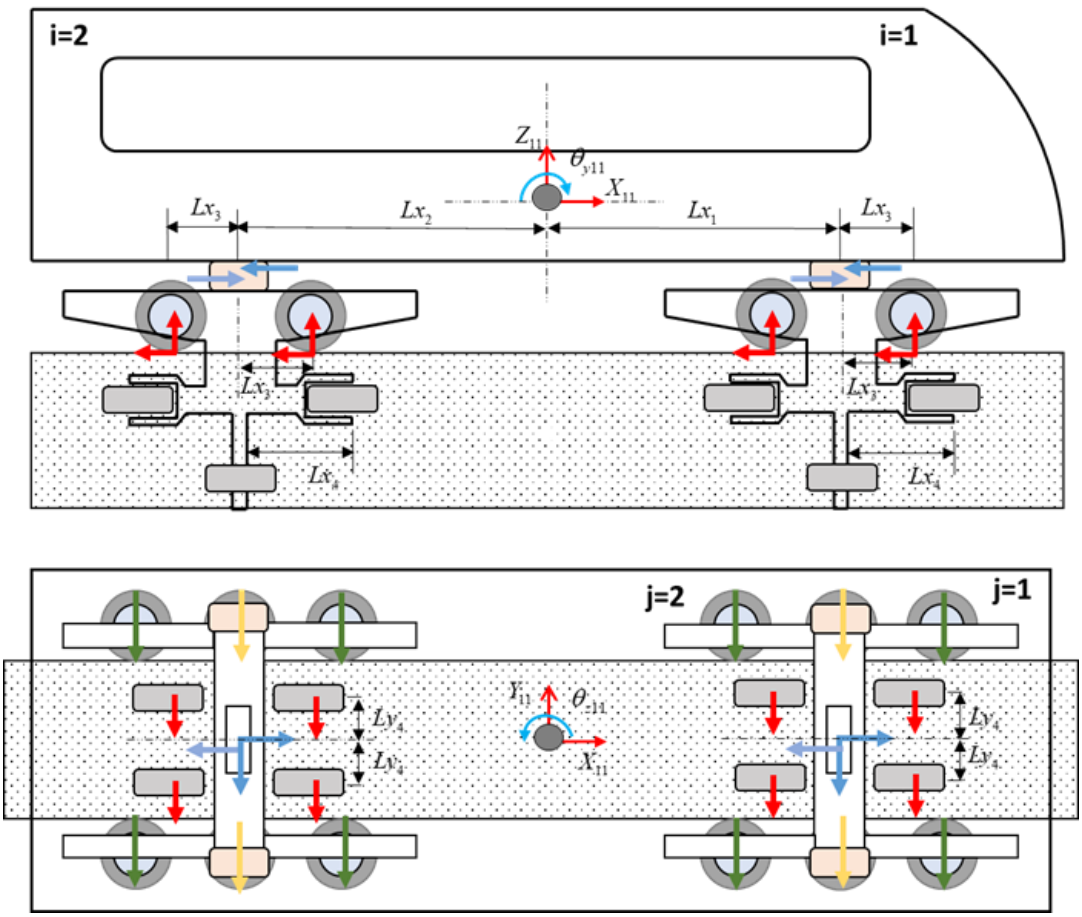

Figure 2.17: Schematic side and top views of the idealized monorail vehicle.

Vertical and lateral air suspensions, installed between the vehicle body and the bogies, are modelled as linear springs and dampers. The bogie frame of the monorail vehicle is connected to the guideway with the running, guide and stabilizing tires. These tires are modelled as stiffness and damping elements. It is assumed that tires and guideway maintain constant contact. To apply a semi-active control for suppressing the axial and rolling movements, a set of MR dampers are positioned next to air suspensions. The equations governing the motion of monorail vehicle body and bogies are obtained by using the Lagrange equation of motion, as shown in equation (2.25).

$$\frac{d}{dt}\left(\frac{\partial L}{\partial \dot{q}_i}\right)-\frac{\partial L}{\partial q_i}+\frac{\partial D_E}{\partial \dot{q}_i}=Q_i \tag{2.25}$$

where q_i is the generalized coordinate variable and $L=T_E-U_E$ is the Lagrangian equation. Also, Q_i shows the generalized forces and moments. T_E is the total kinetic

energy, U_E is the potential energy resulted from springs elements and U_D is the damping potential. The kinetic and potential energy and damping potential equations are derived as

$$T_E = \frac{1}{2}\begin{pmatrix} \left(m_{11}\dot{z}_{11}{}^2 + m_{11}\dot{y}_{11}{}^2 + I_{x11}\dot{\theta}_{x11}{}^2 + I_{y11}\dot{\theta}_{y11}{}^2 + I_{z11}\dot{\theta}_{z11}{}^2\right) \\ +\sum_{i=1}^{2} m_{2i}\dot{z}_{2i}{}^2 + m_{2i}\dot{y}_{2i}{}^2 + I_{vx2i}\dot{\theta}_{x2i}{}^2 + I_{vy2i}\dot{\theta}_{y2i}{}^2 + I_{vz2i}\dot{\theta}_{z2i}{}^2 \end{pmatrix} \tag{2.26}$$

$$U_E = \frac{1}{2}\left(\sum_{i=1}^{2}\sum_{j=1}^{2}\sum_{n=1}^{2} \begin{Bmatrix} K_{1ijn}R_{1ijn}{}^2\delta_{1j} + K_{2ijn}R_{2ijn}{}^2 \\ +K_{3ijn}R_{3ijn}{}^2 + K_{4ijn}R_{4ijn}{}^2\delta_{1j} \\ +K_{6ijn}R_{6ijn}{}^2\delta_{1j} + K_{\alpha 1ijn}\alpha_1{}^2 \\ +K_{\alpha 2ijn}\alpha_2{}^2 + K_{\alpha 3ijn}\alpha_3{}^2 \end{Bmatrix} + \sum_{i=1}^{2} K_{5i11}R_{5i11}{}^2 \right) \tag{2.27}$$

$$U_D = \frac{1}{2}\left(\sum_{i=1}^{2}\sum_{j=1}^{2}\sum_{n=1}^{2} \begin{Bmatrix} C_{1ijn}\dot{R}_{1ijn}{}^2\delta_{1j} + C_{2ijn}\dot{R}_{2ijn}{}^2 \\ +C_{3ijn}\dot{R}_{3ijn}{}^2 + C_{4ijn}\dot{R}_{4ijn}{}^2\delta_{1j} \\ +C_{6ijn}\dot{R}_{6ijn}{}^2\delta_{1j} \end{Bmatrix} + \sum_{i=1}^{2} C_{5i11}\dot{R}_{5i11}{}^2 \right) \tag{2.28}$$

where i is stating the suspension position ($i = 1$; front, $i = 2$; rear), the subscript j is the tire location in the bogie structure ($j = 1$; frontend, $j = 2$; backend), n is expressing the left and right side of the vehicle ($n = 1$; right side, $n = 2$; left side). Also, R_{1ijn} , R_{2ijn} , R_{3ijn} , R_{4ijn} and R_{5ijn} are the relative displacements at the tire and suspension locations. R_{6ijn} represents the air suspension horizontal displacement while vehicle running on a curved track. These deformations are described in equation (2.29) to (2.34).

$$R_{1ijn} = z_{11} - (-1)^n \theta_{x11}L_{vy2} + (-1)^i \theta_{y11}L_{vxi} - (z_{2i} - (-1)^n \theta_{x2i}L_{y2}) \tag{2.29}$$

$$R_{2ijn} = z_{2i} - (-1)^n \theta_{x2i}L_{vy4} + (-1)^j \theta_{y2i}L_{x3} - V_{2ijn} \tag{2.30}$$

$$R_{3ijn} = y_{2i} + \theta_{x2i}L_{z3} - (-1)^j \theta_{z2i}L_{x4} - V_{3ijn} \tag{2.31}$$

$$R_{4ijn} = y_{2i} + \theta_{vx2i}\left(L_{z3} + L_{z4}\right) - V_{4ijn} \tag{2.32}$$

$$R_{5ijn} = y_{11} + \theta_{x11}L_{z1} - (-1)^{i}\theta_{z11}L_{xi} - \left(y_{2i} - \theta_{x2i}L_{z2}\right) \tag{2.33}$$

$$R_{6ijn} = -\theta_{x11}L_{z1} + (-1)^{n}\theta_{z11}L_{y2} - (\theta_{y2i}L_{z2} + (-1)^{n}\theta_{z2i}L_{y2}) \tag{2.34}$$

Each tire in the bogie structure performs different slip ratios due to the nature of vehicle dynamics. These slip ratios should be defined properly for expressing the generated tire forces. Tire wheel centre velocities are needed to define tire slip angles. These wheel centre velocities cannot be measured directly but can be calculated by using the relationship between the fixed coordinate system at the vehicle centre of gravity and tire centre. These sideslip angles of the running tire α_2 , guiding tires α_3 and stabilizing tires α_4 can be written as

$$\alpha_2 = \frac{\dot{y}_{2i} - (-1)^{j}\dot{\theta}_{z2i}L_{x3} + \dot{\theta}_{x2i}\left(L_{z6} - L_{z5}\right)}{V_x} - \theta_{z2i} \tag{2.35}$$

$$\alpha_3 = \frac{-(-1)^{n}\dot{z}_{2i} - (-1)^{(j+n)}\dot{\theta}_{y2i}L_{x4} + \dot{\theta}_{x2i}\left(L_{y5} - L_{y1}\right)}{V_x} - (-1)^{n}\theta_{y2i} \tag{2.36}$$

$$\alpha_4 = \frac{-(-1)^{n}\dot{z}_{2i} + \dot{\theta}_{x2i}\left(L_{y5} - L_{y1}\right)}{V_x} - (-1)^{n}\theta_{y2i} \tag{2.37}$$

- Equations of motion for monorail body

Vertical motion:

$$\begin{aligned} m_{11}\ddot{z}_{11} = & \sum_{i=1}^{2}\sum_{j=1}^{1}\sum_{n=1}^{2}\left\{-K_{1ijn}R_{1ijn} - C_{1ijn}\dot{R}_{1ijn}\right\} \\ & -\left\{f_{MR_{FR}} + f_{MR_{FL}} + f_{MR_{RR}} + f_{MR_{RL}}\right\} + m_{11}\left\{\frac{V^2}{R_{11}}\sin\theta_{11} + g\left(1-\cos\theta_{11}\right) + Ly_4\ddot{\theta}_{se_{11}}\right\} \end{aligned} \tag{2.38}$$

Lateral motion:

$$m_{11}\ddot{y}_{11} = \sum_{i=1}^{2}\sum_{j=1}^{1}\sum_{n=1}^{1}\left\{-K_{5ijn}R_{5ijn} - C_{5ijn}\dot{R}_{5ijn}\right\} - f_{MR_{FM}} - f_{MR_{RM}}$$
$$-m_{11}\left\{\frac{V^2}{R_{11}}\cos\theta_{11} - g\sin\theta_{11} + H_{cog11}\ddot{\theta}_{se_{11}}\right\} \tag{2.39}$$

Roll motion:

$$I_{x11}\ddot{\theta}_{x11} = \sum_{i=1}^{2}\sum_{j=1}^{1}\sum_{n=1}^{2}\left\{\begin{matrix}(-1)^n Ly_2\left(K_{1ijn}R_{1ijn} + C_{1ijn}\dot{R}_{1ijn}\right)\\ -Lz_1\left(K_{5ijn}R_{5ijn} + C_{5ijn}\dot{R}_{5ijn}\right)\end{matrix}\right\}$$
$$-a\left(f_{MR_{FR}} + f_{MR_{RR}}\right) + b\left(f_{MR_{FL}} + f_{MR_{RL}}\right) - Lz_1\left(f_{MR_{FM}} + f_{MR_{RM}}\right) \tag{2.40}$$
$$+\ddot{y}_{11}Lz_1 - I_{x11}\ddot{\theta}_{se}$$

Pitch motion:

$$I_{y11}\ddot{\theta}_{y11} = \sum_{i=1}^{2}\sum_{j=1}^{1}\sum_{n=1}^{2}\left\{\begin{matrix}-(-1)^i Lx_i\left(K_{1ijn}R_{1ijn} + C_{1ijn}\dot{R}_{1ijn}\right)\\ +Lz_1\left(K_{6ijn}R_{6ijn} + C_{6ijn}\dot{R}_{6ijn}\right)\end{matrix}\right\} \tag{2.41}$$
$$- Lx_2\left(f_{MR_{RR}} + f_{MR_{RL}}\right) + Lx_1\left(f_{MR_{FR}} + f_{MR_{FL}}\right)$$

Yaw motion:

$$I_{z11}\left(\ddot{\theta}_{z11} + V\frac{d}{dt}\left(\frac{1}{R_{11}}\right)\right) = \sum_{i=1}^{2}\sum_{j=1}^{1}\sum_{n=1}^{1}\left\{\begin{matrix}(-1)^i Lx_i\left(K_{5ijn}R_{5ijn} + C_{5ijn}\dot{R}_{5ijn}\right)\\ -(-1)^n Ly_2\left(K_{hijn}R_{hijn} + C_{hijn}\dot{R}_{hijn}\right)\end{matrix}\right\} \tag{2.42}$$
$$- Lx_1 f_{MR_{FM}} + Lx_2 f_{MR_{RM}}$$

- Equations of motion of bogie frames ($i = 1,2$)

Vertical motion:

$$m_{11}\left(\ddot{z}_{2i}\right) = \sum_{i=1}^{1,2}\sum_{j=1}^{2}\sum_{n=1}^{2}\left\{\begin{matrix}\left(K_{1ijn}R_{1ijn} + C_{1ijn}\dot{R}_{1ijn}\right) - \left(K_{2ijn}R_{2ijn} + C_{2ijn}\dot{R}_{2ijn}\right)\\ -\left(Ky_{3ijn}\alpha_{3ijn}\right) - \left(Ky_{4ijn}\alpha_{4ijn}\right)\end{matrix}\right\} \tag{2.43}$$
$$+ f_{MR_{FR}} + f_{MR_{FL}} + m_{2i}\left\{\frac{V^2}{R_{2i}}\sin\theta_{2i} + g\left(1-\cos\theta_{2i}\right) + Ly_4\ddot{\theta}_{se_{2i}}\right\}$$

Lateral motion:

$$m_{11}\left(\ddot{y}_{2i}\right)=\sum_{i=1}^{1,2}\sum_{j=1}^{2}\sum_{n=1}^{2}\left\{\begin{array}{l}\left(K_{5ijn}R_{5ijn}+C_{5ijn}\dot{R}_{5ijn}\right)-\left(K_{3ijn}R_{3ijn}+C_{3ijn}\dot{R}_{3ijn}\right)\\-\left(K_{4ijn}R_{4ijn}+C_{4ijn}\dot{R}_{4ijn}\right)\delta_{1j}-\left(Ky_{2ijn}\alpha_{2ijn}\right)\\-\left(K_{3ijn}\dfrac{Lx_4^{\ 2}}{2R_{2i}}\right)-\left(K_{4ijn}\dfrac{Lx_4^{\ 2}}{2R_{2i}}\right)\\-\left(C_{3ijn}\dfrac{Lx_4^{\ 2}}{2\dot{R}_{2i}}\right)-\left(C_{4ijn}\dfrac{Lx_4^{\ 2}}{2\dot{R}_{2i}}\right)\end{array}\right\}$$
$$+\ f_{MR_{FM}}-m_{2i}\left\{\frac{V^2}{R_{2i}}\cos\theta_{2i}-g\sin\theta_{2i}+H_{cog\,2i}\ddot{\theta}_{se_{2i}}\right\} \tag{2.44}$$

Roll motion:

$$I_{x2i}\ddot{\theta}_{x2i}=\sum_{i=1}^{1,2}\sum_{j=1}^{2}\sum_{n=1}^{2}\left\{\begin{array}{l}-\left(-1\right)^n Ly_2\left(K_{1ijn}R_{1ijn}+C_{1ijn}\dot{R}_{1ijn}\right)-Lz_2\left(K_{5ijn}R_{5ijn}+C_{5ijn}\dot{R}_{5ijn}\right)\delta_{1j}\\+\left(-1\right)^n Ly_4\left(K_{2ijn}R_{2ijn}+C_{2ijn}\dot{R}_{2ijn}\right)-Lz_3\left(K_{3ijn}R_{3ijn}+C_{3ijn}\dot{R}_{3ijn}\right)\\-\left(Lz_3+Lz_4\right)\left(K_{4ijn}R_{4ijn}+C_{4ijn}\dot{R}_{4ijn}\right)-Lz_6\left(Ky_{2ijn}\alpha_{2ijn}\right)\\+\left(-1\right)^n Ly_1\left(Ky_{3ijn}\alpha_{3ijn}\right)+\left(-1\right)^n Ly_1\left(Ky_{4ijn}\alpha_{4ijn}\right)\delta_{1j}\\-Lz_3\left(K_{3ijn}\dfrac{Lx_4^{\ 2}}{2R_{2i}}\right)-Lz_3\left(C_{3ijn}\dfrac{Lx_4^{\ 2}}{2\dot{R}_{2i}}\right)-\left(Lz_3+Lz_4\right)\left(K_{4ijn}\dfrac{Lx_4^{\ 2}}{2R_{2i}}\right)\\-\left(Lz_3+Lz_4\right)\left(C_{4ijn}\dfrac{Lx_4^{\ 2}}{2\dot{R}_{2i}}\right)\end{array}\right\}$$
$$+\left(bf_{MR_{FL}}-af_{MR_{FR}}-Lz_3 f_{MR_{FM}}\right)+\ddot{y}_{2i}Lz_6-I_{x2i}\ddot{\theta}_{se} \tag{2.45}$$

Pitch motion:

$$I_{y2i}\ddot{\theta}_{y2i}=\sum_{i=1}^{1,2}\sum_{j=1}^{2}\sum_{n=1}^{2}\left\{\begin{array}{l}-\left(-1\right)^j Lx_3\left(K_{2ijn}R_{2ijn}+C_{2ijn}\dot{R}_{2ijn}\right)\\+\left(-1\right)^j Lx_4\left(Ky_{3ijn}\alpha_{3ijn}\right)\\-Lz_2\left(K_{6ijn}R_{6ijn}+C_{6ijn}\dot{R}_{6ijn}\right)\end{array}\right\} \tag{2.46}$$

Yaw motion:

$$I_{z2i}\left(\ddot{\theta}_{z2i}+V\frac{d}{dt}\left(\frac{1}{R_{2i}}\right)\right)=\sum_{i=1}^{1,2}\sum_{j=1}^{2}\sum_{n=1}^{2}\left\{\begin{array}{l}\left(-1\right)^j Lx_4\left(K_{3ijn}R_{3ijn}+C_{3ijn}\dot{R}_{3ijn}\right)\\+\left(-1\right)^j\left(Ky_{2ijn}\alpha_{2ijn}\right)+\left(-1\right)^n Ly_2\left(K_{6ijn}R_{6ijn}+C_{6ijn}\dot{R}_{6ijn}\right)\\+Ktz_{ijn}\alpha_{2ijn}-Lx_4\left(K_{3ijn}\dfrac{Lx_4^{\ 2}}{2R_{2i}}\right)-Lx_4\left(C_{3ijn}\dfrac{Lx_4^{\ 2}}{2\dot{R}_{2i}}\right)\end{array}\right\} \tag{2.47}$$

when equation (2.38) – (2.47) are rearranged in matrix form

$$\ddot{x}_s = M^{-1}C\dot{x}_s + M^{-1}Kx_s + M^{-1}Hf + M^{-1}LF_{dist} \tag{2.48}$$

Here, M , C and K matrices represent the mass, damping and stiffness properties of the model subcomponents, respectively. H matrix stands for the location of the MR dampers. Road inputs due to guideway geometry and surface irregularities are applied to the system by the L vector. The state vector of the system is selected as,

$$x_s = [z_{11} \quad y_{11} \quad \theta_{z11} \quad \theta_{y11} \quad \theta_{x11} \quad z_{21} \quad y_{21} \quad \theta_{z21} \quad \theta_{y21} \quad \theta_{x21} \quad z_{22} \quad y_{22} \quad \theta_{z22} \quad \theta_{y22} \quad \theta_{x22}]^T \tag{2.49}$$

Each force terms of the MR damper in the f vector is selected as,

$$f = \begin{bmatrix} f_{MR_{FR}} & f_{MR_{FM}} & f_{MR_{FL}} & f_{MR_{RR}} & f_{MR_{RM}} & f_{MR_{RL}} \end{bmatrix}^T \tag{2.50}$$

Finally, equation (2.48) can be written as a state space equation as follows

$$\begin{aligned} \dot{x} &= Ax + Bu + WF_{dist} \\ &= \begin{bmatrix} 0_{15x15} & I_{15x15} \\ M^{-1}K & M^{-1}C \end{bmatrix} x + \begin{bmatrix} 0_{15x6} \\ M^{-1}H \end{bmatrix} f + \begin{bmatrix} 0_{15x46} \\ M^{-1}L \end{bmatrix} F_{dist} \end{aligned} \tag{2.51}$$

The horizontal road profile used to validate the modelling study that runs in MATLAB consists of 50 m straight segment and circular curve series that have a radius of 350 m, 200 m and 150 m. Also, the super elevation values are selected as, 2.92 %, 5.1 % and 6.8 % for the corresponding circular curves. The vehicle speed is kept constant at 10 m/s. The rest of the model parameters are given in Appendix B. When Figures 2.18 to Figure 2.22 are examined, constructed model and the multi-body software simulation results of displacement responses are in close agreement leading to the conclusion that the constructed model can be used in control design studies.

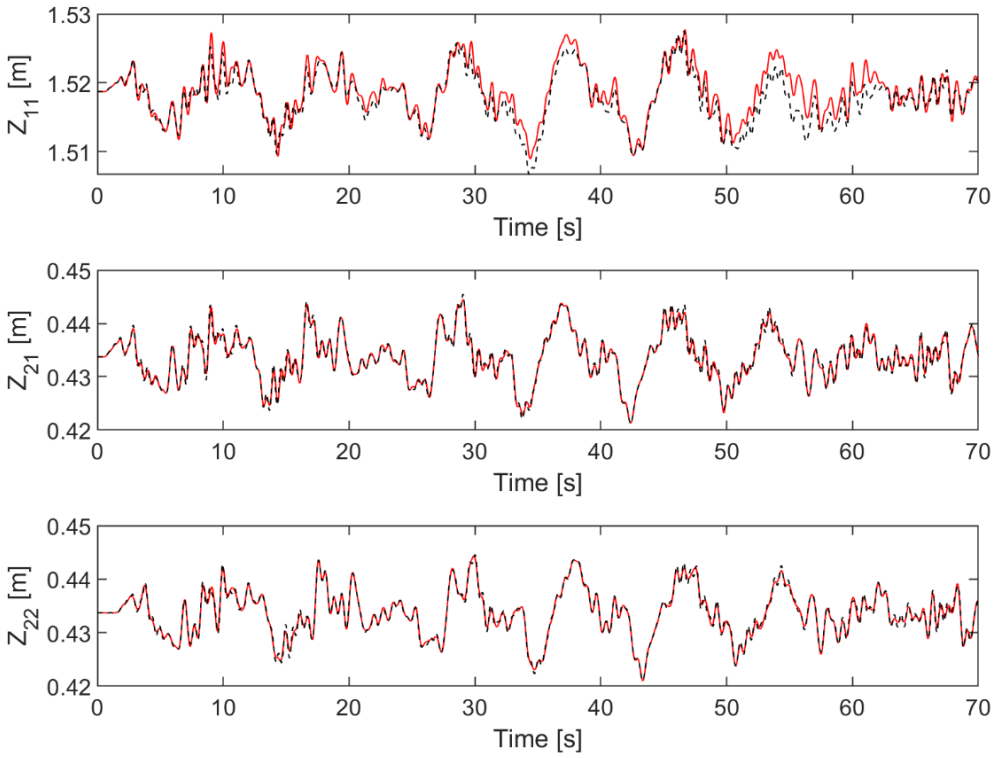

Figure 2.18: Vertical displacements of the bogies vehicle body (dotted black: UM, solid red: MATLAB).

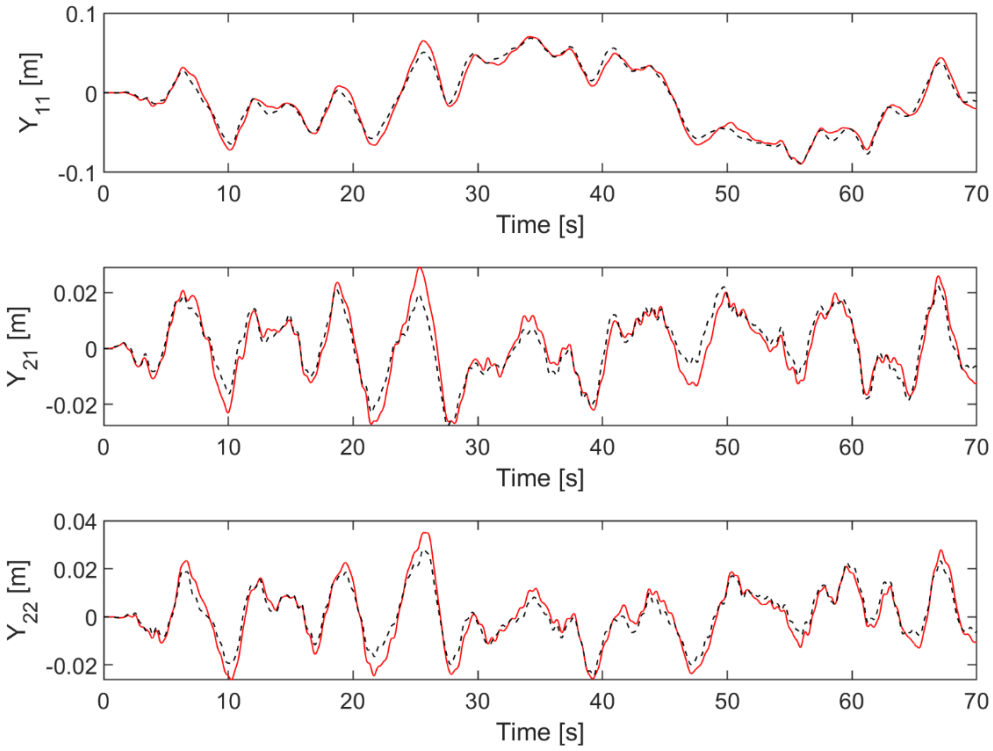

Figure 2.19: Lateral displacements of the bogies vehicle body (dotted black: UM, solid red: MATLAB).

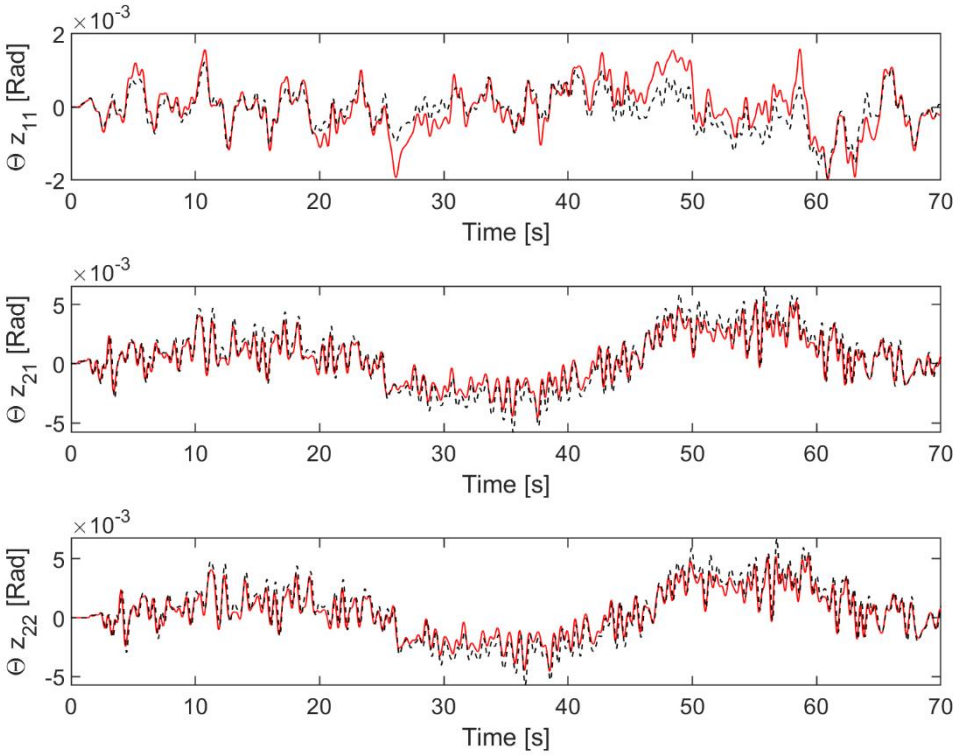

Figure 2.20: Yaw displacements of the bogies vehicle body (dotted black: UM, solid red: MATLAB).

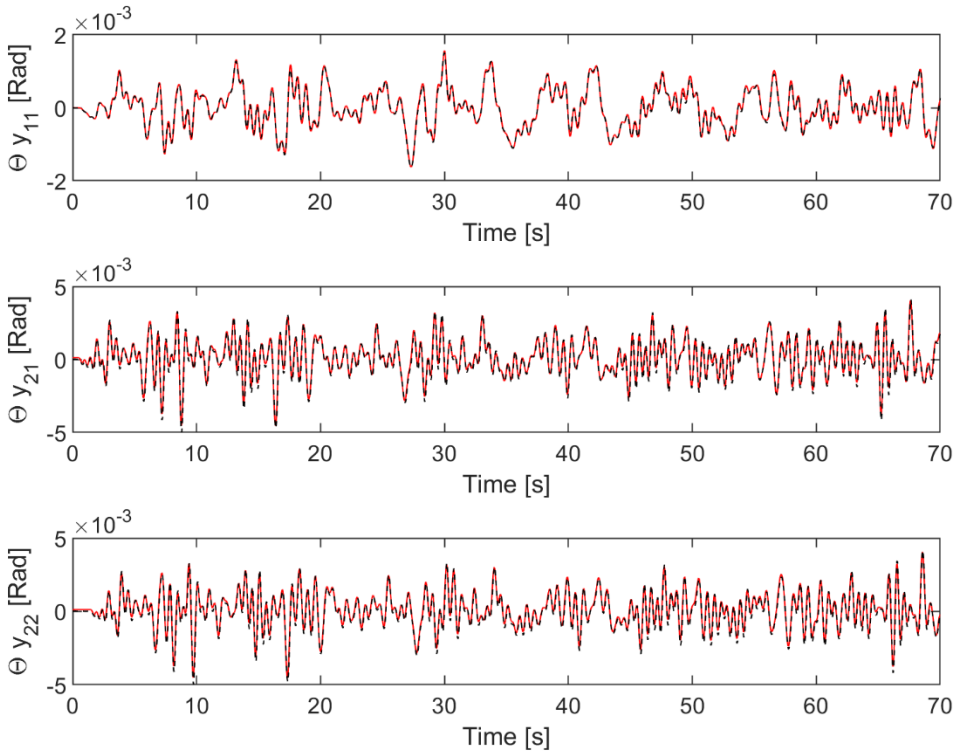

Figure 2.21: Pitch displacements of the bogies vehicle body (dotted black: UM, solid red: MATLAB).

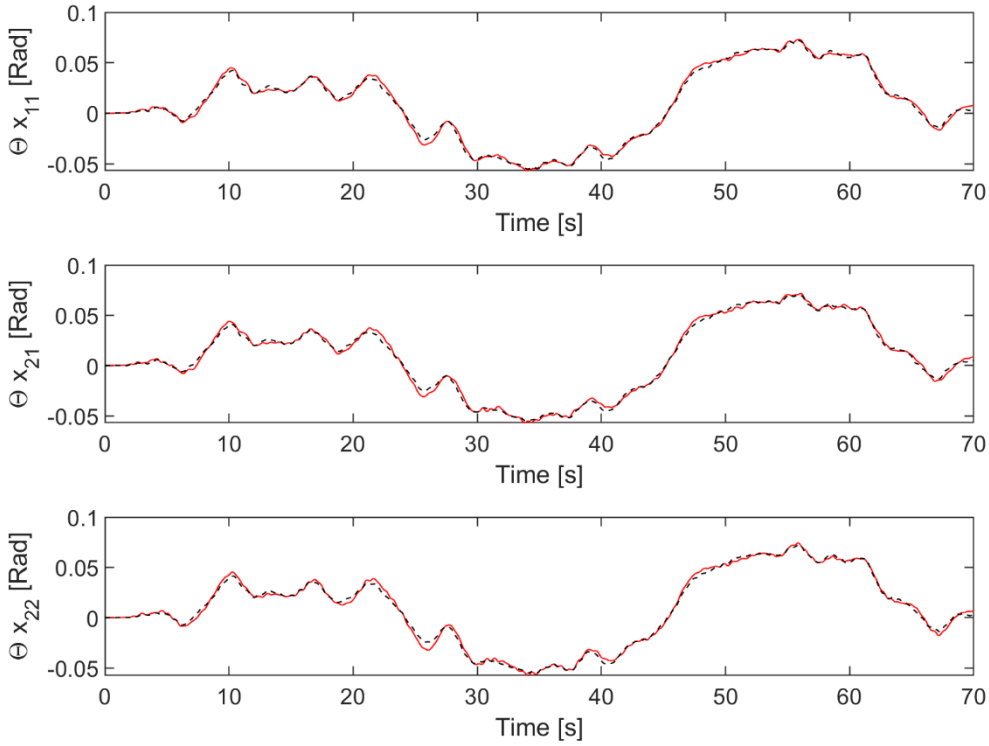

Figure 2.22: Roll displacements of the bogies vehicle body (dotted black: UM, solid red: MATLAB).

2.5. Assessment of the Critical Design Parameters

The dynamic performance of railway vehicles mainly includes three aspects: vehicle stability, driving comfort and curve passing ability. As in the rail vehicles, monorails are exposed to strong lateral influences during the curve negotiation. In addition, the small lateral span of the running wheel of the straddle type monorail vehicle cannot provide sufficient anti-overturning capacity. To eliminate this deficiency the stabilization wheels are added to both sides of the bogie. Also, an initial preload pressure is applied to all guiding tires and stabilizing tires to ensure consistent contact condition between the guideway and tires.

In the selection of the reasoned value of pre-pressure on stabilizing tires, there is a trade-off between uncompensated lateral acceleration a_{nc}, and anti-overturning capacity. Excessive pre-pressure leads to rapid tire wear and increase lateral acceleration. It should be noted that passengers experience no obvious feelings of acceleration when $a_{nc} \leq 0.5$ ms^{-2} and do not tolerate uncompensated lateral accelerations that exceeding the $1 \sim 1.2$ ms^{-2} [Yuanjin Ji, 2018], [Brenna, 2018]. Also,

insufficient preload reduces the rolling stiffness and cause structural damage. In this subsection, the relation between required tire pre-pressure and the critical lateral force is established. When the preload pressure of the stabilizing wheels is determined, the maximum and minimum negotiation speeds at curves can be set to ensure the required anti-overturning capacity of the vehicles. Neglecting the vertical, pitching and yawing motion system dynamic equation given in equation (2.51) can be rewritten as,

$$\begin{bmatrix} s_{11} & s_{12} & s_{13} & s_{14} & s_{15} & s_{16} \\ s_{21} & s_{22} & s_{23} & s_{24} & s_{25} & s_{26} \\ s_{31} & s_{32} & s_{33} & s_{34} & s_{35} & s_{36} \\ s_{41} & s_{42} & s_{43} & s_{44} & s_{45} & s_{46} \\ s_{51} & s_{52} & s_{53} & s_{54} & s_{55} & s_{56} \\ s_{61} & s_{62} & s_{63} & s_{64} & s_{65} & s_{66} \end{bmatrix} \begin{bmatrix} y_{11} \\ y_{21} \\ y_{22} \\ \theta_{x11} \\ \theta_{x21} \\ \theta_{x22} \end{bmatrix} = \begin{bmatrix} F_c \\ 2F_{gl} - 2F_{gr} + F_{sl} - F_{sr} \\ 2F_{gl} - 2F_{gr} + F_{sl} - F_{sr} \\ F_c\left(Lz_1 + Lz_2\right) \\ 2Lz_3\left(F_{gl} - F_{gr}\right) + \left(Lz_3 + Lz_4\right)\left(F_{sl} - F_{sr}\right) \\ 2Lz_3\left(F_{gl} - F_{gr}\right) + \left(Lz_3 + Lz_4\right)\left(F_{sl} - F_{sr}\right) \end{bmatrix} \quad (2.52)$$

Also, equation (2.52) can be arranged as

$$x_p = S^{-1} F_{ext} \quad (2.53)$$

Here, F_{ext} is the external force that exerted on the vehicle body, F_{gl}, F_{gr}, F_{sl}, F_{sr} are the pre-pressure on the guiding and stabilizing tires, respectively. Since the lateral displacement at the stabilizing tire location is greater than the guiding tires under the rolling motion of the bogie, they lose their contact with the guideway much earlier stage and the preload on the corresponding tire becomes zero. The stabilizing tire displacement at the same side of the applied force can be written as

$$\begin{aligned} y_{s21} &= y_{21} + \theta_{x21}\left(Lz_3 + Lz_4\right) \\ y_{s22} &= y_{22} + \theta_{x22}\left(Lz_3 + Lz_4\right) \end{aligned} \quad (2.54)$$

Due to the external force acting on the monorail body F_c, the stabilizing tire at the critical side loses contact with the guideway surface right after the amount of

compressed tire deflection, which is defined by the equality of $y_{cr} = \left(F^{preload} / R_{4ijn}\right)$, is exceeded. Thus, the initial pressure value can be written by using the equality of $y_{cr} = y_{sij}$,

$$F^{preload} = K_{4ijn}\left\{y_{21} + \theta_{x21}\left(Lz_3 + Lz_4\right)\right\} \tag{2.55}$$

the relation between tire initial pressure and the external force can be written by using the equation (2.54) and (2.55),

$$F^{preload} = \bar{a}F_c + \bar{b} \tag{2.56}$$

Here a and b are the system constant that depends on the monorail vehicle parameters such as suspension stiffness or geometric values. When the external force F_c is due to the lateral acceleration $F_c = ma_{nc}$, critical lateral acceleration that causes the tire contact losing can be written as,

$$a_{nc} = \frac{F^{preload} - \bar{b}}{m_{11}\bar{a}} \tag{2.57}$$

According to Table 2.4, one can be concluded that the 30 mm pre-displacement that corresponding to 9.75 kN preload is suitable for the considered monorail vehicle.

Table 2.4: Critical value of centrifugal acceleration.

Pre-load (mm)	Corresponding preload (kN)	Critical value of unbalanced acceleration (ms^{-2})
5	1.625	0.1456
10	3.250	0.2912
20	6.500	0.5824
30	9.750	0.8737
40	13.000	1.1649

When the monorail vehicle negotiating a curve track, lateral unbalanced acceleration can be written as,

$$a_{nc} = \frac{V^2}{R} - g\theta_{se} \tag{2.58}$$

After equation (2.57) substitute into the left side of equation (2.58), the relation between tire preload that ensure the contact condition and the vehicle speed can be written as

$$V = \sqrt{\left(\frac{F^{preload} - \bar{b}}{m_{11}\bar{a}} \pm g\theta_{se} \right) R} \tag{2.59}$$

Table 2.5 summarizes the critical speed condition under different super elevation when the 13 kN preload is applied to guiding and stabilizing wheels. Also, a dynamic simulation study is performed to compare the results.

Table 2.5: Maximum curving speed (m/s) with 13 kN preload.

Curve Radius	Curve super elevation rate							
	% 3		% 5		% 8		% 12	
	(2.59)	UM	(2.59)	UM	(2.59)	UM	(2.59)	UM
R-50	8.72	9.15	9.26	9.70	10.02	10.42	10.96	11.30
R-100	12.33	12.6	13.10	13.40	14.18	14.45	15.50	15.75
R-150	15.10	15.4	16.05	16.35	17.37	17.65	18.99	19.22
R-200	17.44	17.8	18.53	18.85	20.05	20.35	21.92	22.19
R-300	21.36	21.6	22.69	23.00	24.57	24.95	26.87	27.20

It can be concluded that the vehicle running speed can be adjusted by the equation (2.59) which considers the vehicle parameters such as the weight of vehicle, stiffness of the tire and suspension componenets instead of limits specifed by international standards.

3. ROBUST CONTROL DESIGN

H_∞ control approach has been widely applied in suspension control of railway vehicles [Yıldız et al., 2015], [Orvnäs et al., 2011]. In H_∞ control design, it is desired to synthesize a controller $K_\infty(s)$ that the closed-loop system with the input w and output y is stabilized, and the performance output z is minimized for a given class of disturbance. The transfer matrix from the system disturbance w to the controlled output z is obtained as

$$z = T_{zw}(s)w \tag{3.1}$$

The H_∞ control design objective is to obtain a controller that minimizes the infinity norm of the closed-loop transfer matrix such as

$$\|T_{zw}(s)\|_\infty < \gamma \tag{3.2}$$

where $\gamma > 0$. The generalized control design block structure of the H_∞ control is shown in Figure 3.1.

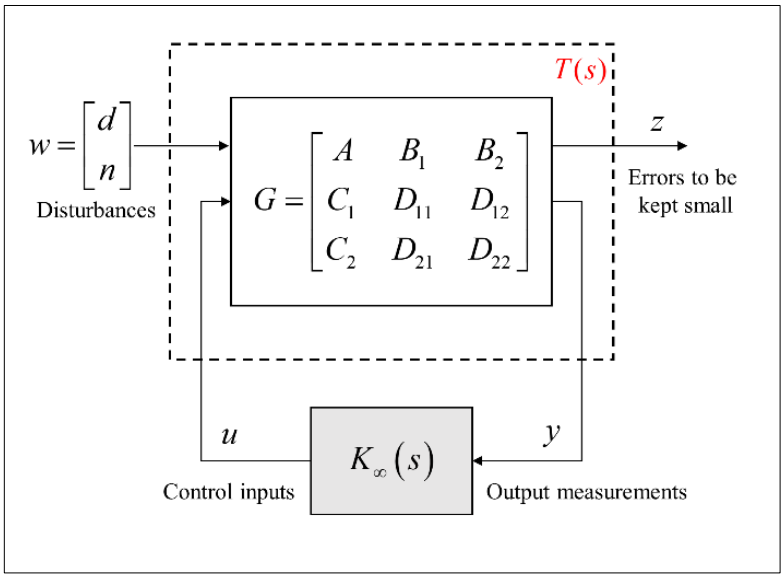

Figure 3.1: Generalized system structure.

3.1. Monorail Vehicle with Uncertainties in Model Parameters

In robust control system design, the inevitable uncertainties, which are caused by both sensor noises and the discrepancy between the mathematical model and the actual dynamics of the system, should be modelled to increase the performance and robustness of the closed-loop system. The inconsistency between actual and modelled dynamic can be classified into two categories as *Unstructured* and *Parametric* uncertainties.

The unstructured dynamics uncertainty usually covers unmodelled or neglected high-frequency dynamics in the system such as reduced-order model. Similarly, real system parameters may change over some ranges, such as the changing weight of the monorail vehicle according to number of passengers. These changes affect the low-frequency range performance. In monorail vehicles, travelling on rubber tires causes tire abrasion. Also, existing uncertainties in a monorail vehicle influence the performance of suspension systems. Therefore, system parameters related to tire dynamics, weight changes and the actuator unmodelled dynamics should be modelled considering these uncertainties. Open-loop block diagram of the uncertain monorail vehicle model is given in Figure 3.2.

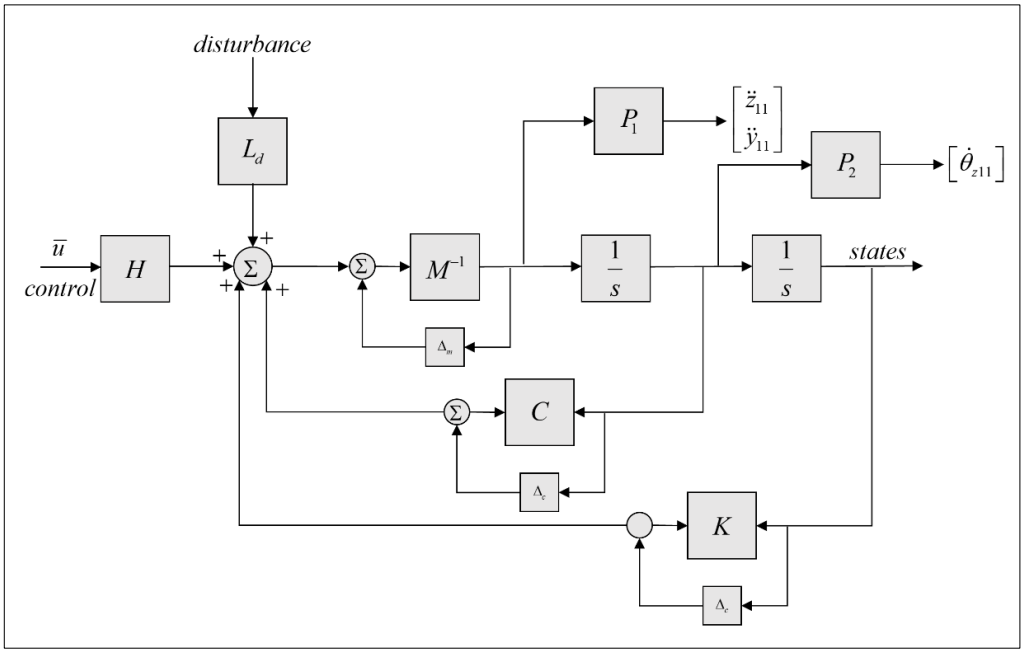

Figure 3.2: Open-loop block diagram model including structured uncertainties.

In the H_∞ control design, it is assumed that the running tire parameters (both damping and stiffness properties) include 15% uncertainties, also, vehicle body and the bogies include 10% uncertainties in mass properties corresponding to the weight of 20 people. The uncertain frequency responses of the open-loop monorail vehicle model, which are sampled at 22 values, from the running tire placed at the front bogie left side to the vehicle vertical acceleration, is given in Figure 3.3 with its nominal value.

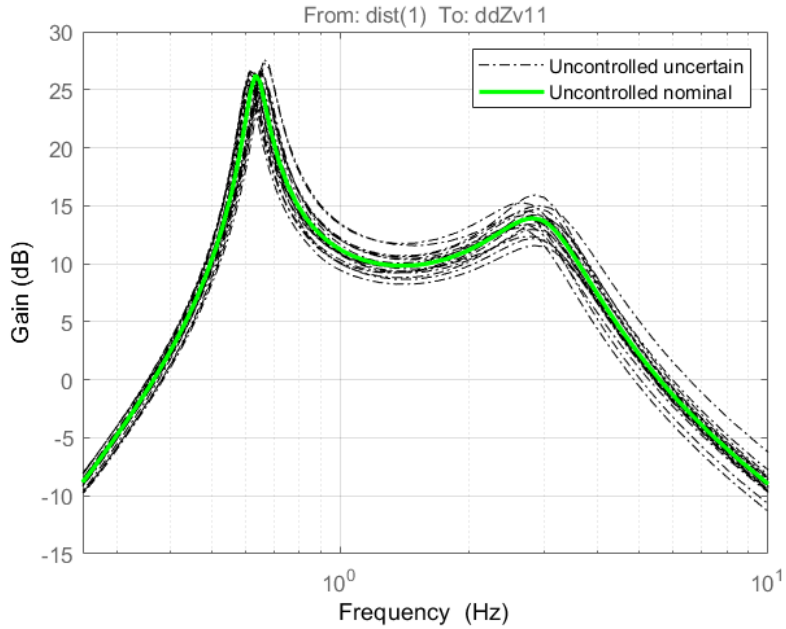

Figure 3.3: Uncertain frequency responses of the monorail vehicle.

3.2. MR Damper Model with Multiplicative Uncertainty

The mathematical model of the MR damper used in this study has a nonlinear characteristic. To incorporate the suspension model into system dynamics, the nominal model of the MR dampers is assumed as a first-order phase-lag model, the transfer function which is given as

$$G_m(s) = \frac{\mathrm{N}}{\mathrm{D}.s+1} = 10\frac{1360}{0.001s+1} \tag{3.3}$$

By using the transfer function approach, it is possible to realize the nonlinear force output of the MR damper at an acceptable level throughout the road profile as

seen in Figure 3.4. Here, it is presumed that both N and D parameters include 20 % uncertainties. This assumption corresponding to parameter variation of the MR damper due to heating or deterioration in time.

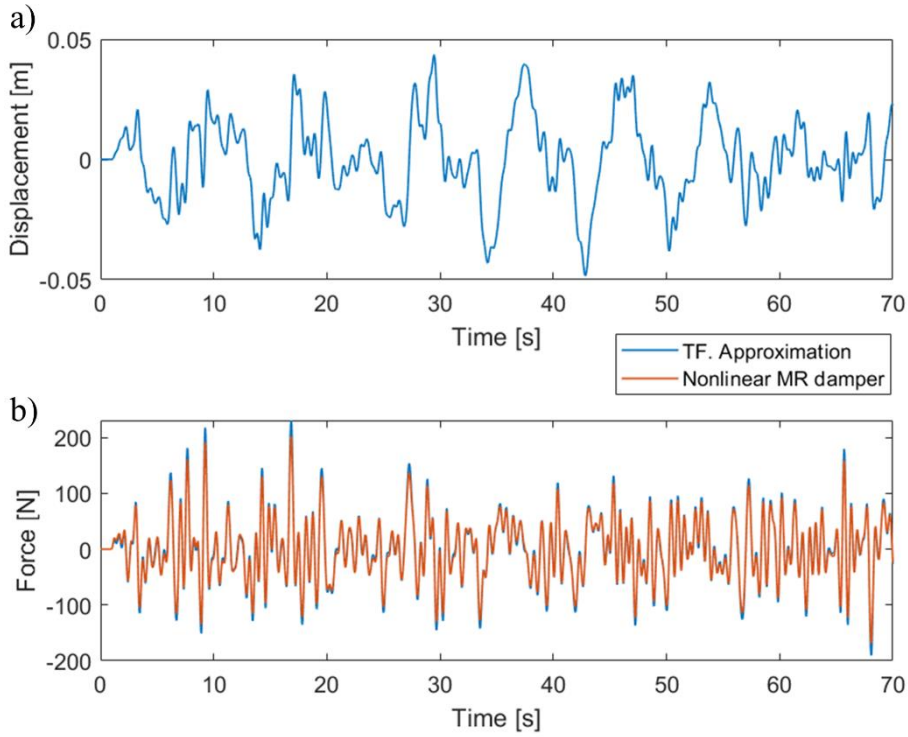

Figure 3.4: Transfer function approximation: a) Input displacement, b) Force output.

By assuming uncertainties in MR dampers, nonlinear effects and variations of the model parameters due to in-service conditions can be modelled more realistically. Existing uncertainties can be approximated by input multiplicative uncertainties for each actuator as given in Equation 3.4 and depicted in Figure 3.5.

$$T(s) = T_m(s)\left(1 + W_m(s)\Delta_m(s)\right) \tag{3.4}$$

where T is the transfer function of the perturbed model, Δ_m is the diagonal normalised uncertainty, W_m is the diagonal weighting function matrix.

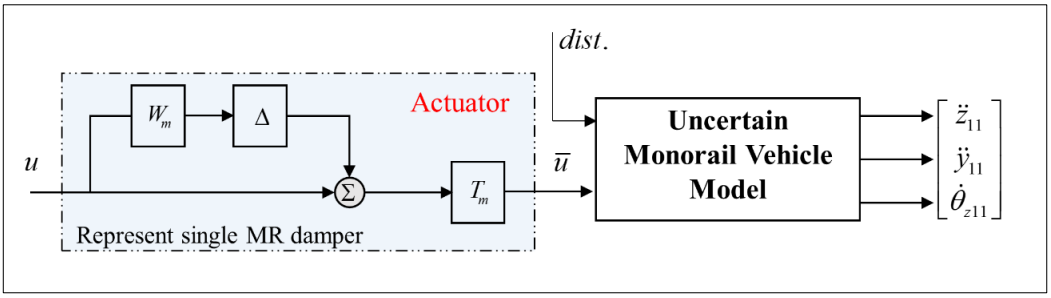

Figure 3.5: Open loop vehicle model including uncertain actuator model.

Determining $W_m(j\omega)$ is equivalent to finding an upper bound for the magnitude response of relative error. The filter $W_m(j\omega)$ is designed as

$$W_m(s) = \frac{0.5146s^2 + 10220s + 4.92\text{x}10^6}{s^2 + 20050s + 2.345\text{x}10^7} \tag{3.5}$$

The frequency response of the uncertain transfer function approximation by multiplicative uncertainty and the filter W_m is given Figure 3.6.

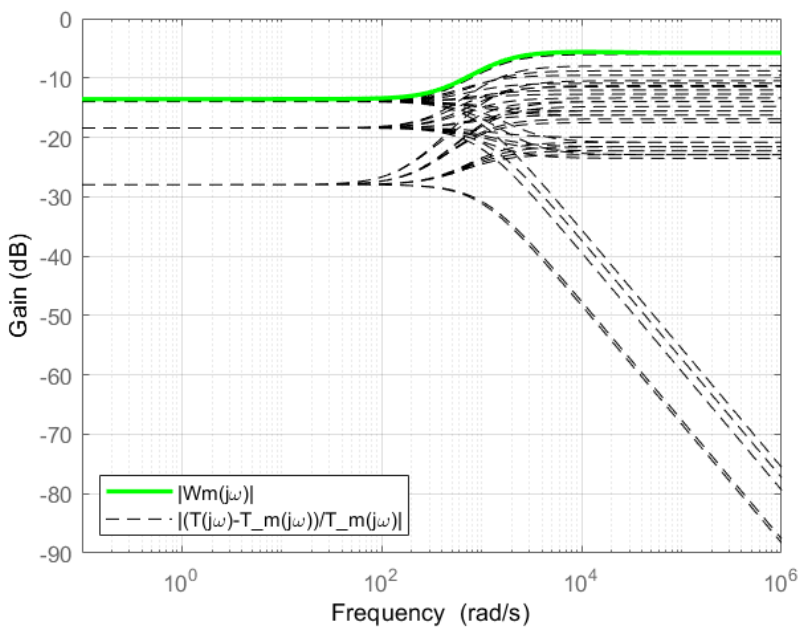

Figure 3.6: Frequency response transfer function.

3.3. Weighting Transfer Function for Sensor Noises

In robust control applications, sensor noises, that are unavoidable in practice, should also be considered to improve the output performance of the control system. The transfer function of the weighting filter for the sensor noise is selected as a high-pass filter and arranged in diagonal form for each measurement channel. By selecting transfer function as given in equation (3.6), the magnitude of the measurement error can be calculated by "dB-Gain" conversion, in this case, the measurement error about 0.001 is constructed in the low-frequency range and 0.0995 measurement error in the high-frequency range, The filter for shaping sensor noise can be constructed by W_n, $W_n(s) = \text{diag}(1/w_n, 1/w_n, 1/w_n, 1/w_n, 1/w_n, 1/w_n)$.

$$w_n(s) = 1\text{x}10^{-3}\frac{10s+1}{0.1s+1} \tag{3.6}$$

3.4. Selection of the Performance Filters

In H_∞ control design, weighting functions are applied to the input and output signals of the system to define the amount of influence. Each signal should have in the calculation of the controller. In this section, two cases including different performance filter are considered. In the first control design, the objectives of the controller are reducing the vertical and lateral acceleration of the monorail vehicle to enhance passenger comfort, also a reduction in vehicle yaw rate is aimed to satisfy driving safety criteria. In the second design, the objectives of the controller are aimed to reduce vertical and lateral displacement of the monorail vehicle COG.

For this purpose, three performance weighting filters matrix with nonzero off-diagonal elements are introduced in the control design, $W_p = \text{diag}\left(1/w_{p11} \quad 1/w_{p22} \quad 1/w_{p33}\right)$. The weighting filter w_{p11} is designed for the vehicle vertical acceleration, w_{p22} and w_{p33} are designed for lateral acceleration and the vehicle body yaw rate, respectively.

$$\left.\begin{aligned} w_{p11}(s)^{-1} &= \frac{s^2+23.62s+175}{31.36s^2\ +673.9s+1726} \\ w_{p22}(s)^{-1} &= \frac{0.1s^2+0.1753s+0.164}{9.747s^2\ +9.53s+7.115} \\ w_{p33}(s)^{-1} &= \frac{0.9s^2+2.447s+2.82}{0.2019s^2\ +0.4346s+0.3009} \end{aligned}\right\} case\ 1 \tag{3.7}$$

$$\left.\begin{aligned} w'_{p11}(s)^{-1} &= \frac{s^2+23.62s+175}{3.136s^2\ +67.39s+172.6} \\ w'_{p22}(s)^{-1} &= \frac{0.1s^2+0.1753s+0.164}{0.9747s^2\ +0.953s+0.7115} \\ w'_{p33}(s)^{-1} &= \frac{0.9s^2+2.447s+2.82}{0.02019s^2\ +0.04346s+0.03009} \end{aligned}\right\} case\ 2 \tag{3.8}$$

The control force in the high-frequency range could not be easily followed by the MR damper because of the time delay, thus a first-order transfer function is introduced for the weighting control force as $W_u = \mathrm{diag}(1/w_{uV}, 1/w_{uL}, 1/w_{uV}, 1/w_{uV}, 1/w_{uL}, 1/w_{uV})$ for both cases. Frequency responses of these filters selected for case 1 are given in Figure 3.7.

$$w_{uV}(s) = \frac{0.08395s+110.4}{s+7.353} \tag{3.9}$$

$$w_{uL}(s) = \frac{0.08395s+110.4}{s+7.353} \tag{3.10}$$

In addition to performance weighting filters, the road disturbance inputs are shaped by the constant weight function W_r by taking their maximum amplitudes into consideration. After having an augmented system matrix using the system state space and frequency shaping filters , the multi-objective controller H_∞ is designed using *hinfsyn* command in Matlab. In the control system structure, weighting filters are shown for better understanding of the implementation. This approach is summarized in Figure 3.8.

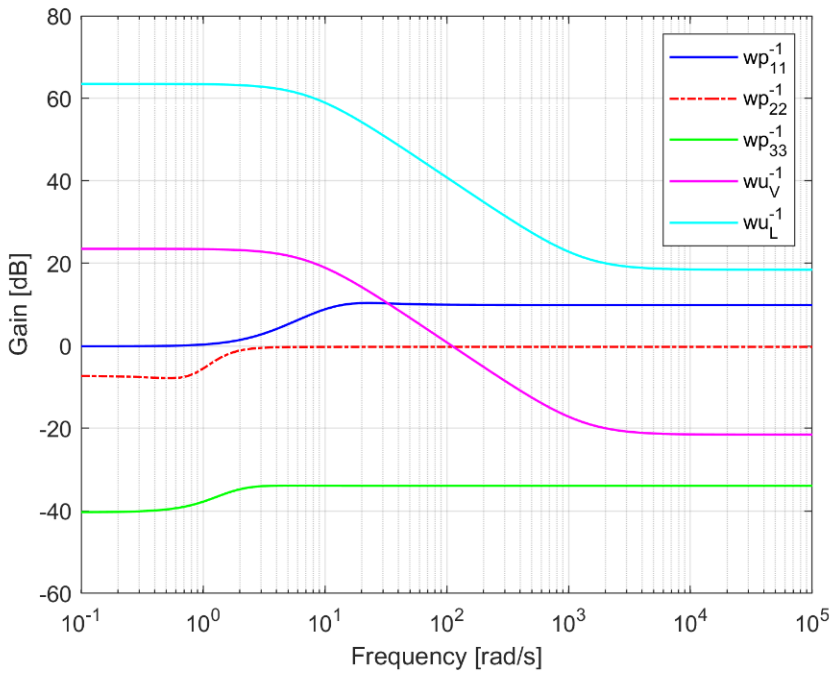

Figure 3.7: Inverse performance weighting functions for case 1.

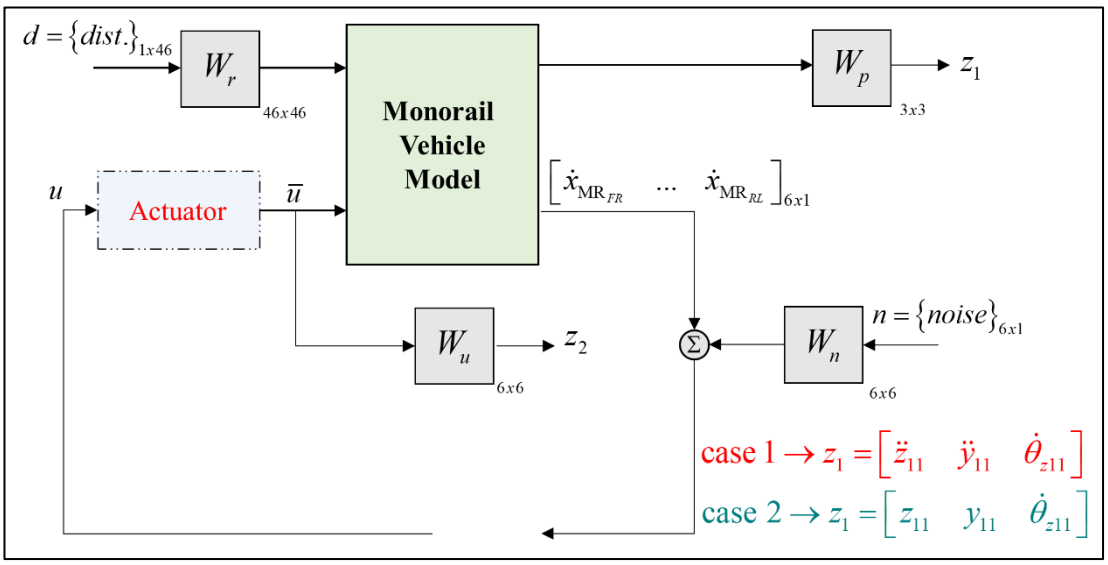

Figure 3.8: Open-loop interconnection.

The closed-loop frequency response, from the running tire placed at the front bogie left side to the vehicle vertical acceleration, is given in Figure 3.9.a). Also, the frequency response from the guiding tire placed at the front bogie left side to the vehicle lateral acceleration is given in Figure 3.10.b).

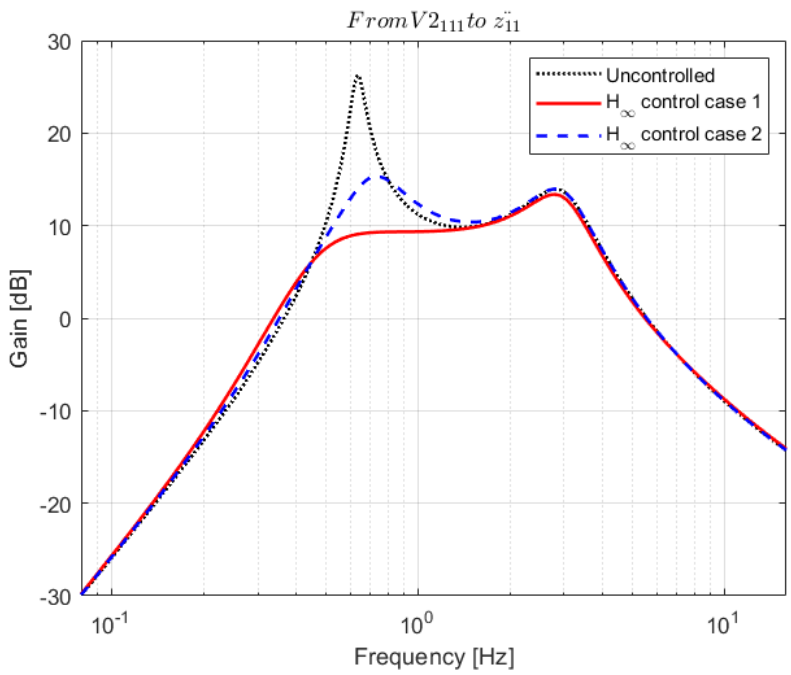

a)

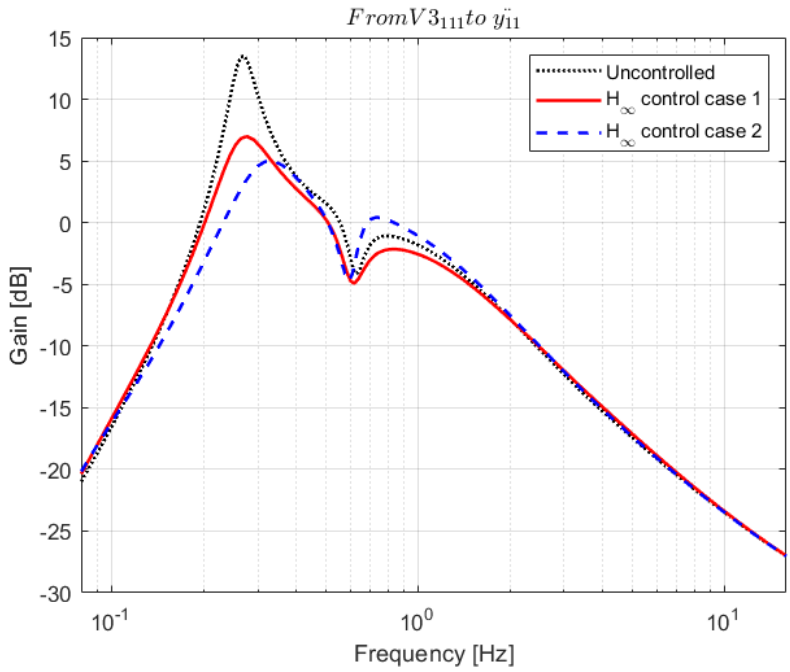

b)

Figure 3.9: Frequency response of the controllers: a) Vertical acceleration, b) Lateral acceleration.

4. ADAPTIVE CONTROL DESIGN

In this section, two different adaptive control schemes are presented for the vibration suppression of the straddle-type monorail vehicle suspension system equipped with magnetorheological damper. In the controller design, parametric uncertainties related to vehicle parameter and the semi-active actuator are considered. Also, the MR damper characteristic changing with applied voltage is taken into consideration in controller design. In the first control design which is based on QLF, the controller tries to minimize the tracking errors that are selected as all translational and rotational dynamics, but it is not guaranteed the required performance constraints such as suspension rattle space usage that should be restricted in practice to avoid mechanical damage and deterioration in comfort. To ensure this restriction, a BLF based constrained adaptive backstepping control design is also presented.

4.1. Adaptive Control Design Based on QLF

In a previous research study of [Yıldız et al., 2015], a nonlinear adaptive controller was designed, and its application was performed experimentally on a suspension system of the quarter car vehicle model. In the mentioned study, only a single MR damper was used and just the vertical dynamics was considered. Same control framework was extended for the monorail vehicle suspension structure in [Yıldız et al. 2019], thus all MR dampers placed on both front and rear bogies in vertical and lateral direction had been controlled at the same time. The control design begins by defining a position tracking error variable $e(t) \in \Re^{n\times 1}$, the control objective is to make $e(t) \to 0$ as $t \to \infty$

$$e = x_s - x_{sd} \tag{4.1}$$

Here, x_{sd} is the desired position of all states, and it is assumed to equal zero. In addition, a filtered tracking error signal denoted by $r(t) \in \Re^{n\times 1}$ is introduced to incorporate the monorail equation of motion defined equation (2.48).

$$r = \dot{e} + \alpha e \tag{4.2}$$

Here $\alpha \in \Re^{n \times n}$ is a constant, diagonal and positive definite gain matrix. The main objective of the controller is regulation of $r(t)$ to adjust both $x_s(t)$ and $\dot{x}_s(t)$. When the system equations are given in equation (2.48) is incorporated into the derivative of equation (4.2), the error dynamics can be obtained as follows

$$\begin{aligned} M\dot{r} &= M\left(\ddot{x}_s + \alpha \dot{x}_s\right) = M\alpha \dot{x}_s + C\dot{x}_s + Kx_s + LF_{dist} + Hf \\ &= \psi\phi + Hf \end{aligned} \tag{4.3}$$

where $\psi \in \Re^{n \times p}$ is a matrix and consists of known and measurable signals and ϕ is the unknown system parameter vector includes mass, inertia, stiffness and damping coefficients of the system

$$\psi = \begin{bmatrix} \psi_m & \psi_c & \psi_k \end{bmatrix} \quad \phi = \begin{bmatrix} \phi_m & \phi_c & \phi_k \end{bmatrix} \tag{4.4}$$

The unknown parameters are constructed as below equation

$$\begin{aligned} \phi_m &= \begin{bmatrix} m_{ii} & I_{zii} & I_{yii} & I_{xii} \end{bmatrix}^T \\ \phi_c &= \begin{bmatrix} C_{1ijn} & C_{2ijn} & C_{3ijn} & C_{4ijn} & C_{5ijn} & C_{6ijn} \end{bmatrix}^T \\ \phi_k &= \begin{bmatrix} K_{1ijn} & K_{2ijn} & K_{3ijn} & K_{4ijn} & K_{5ijn} & K_{6ijn} & Ky_{2ijn} & Ky_{3ijn} & Ky_{4ijn} \end{bmatrix}^T \end{aligned} \tag{4.5}$$

The MR damper force equation given in equation (2.9) contains unknown parameters hence it cannot be used directly. In order to do so, the error dynamic equation can be rewritten as in equation (4.6) by adding and subtracting the estimated force expression $H\hat{f}$ that is defined in equation (2.13).

$$\begin{aligned} M\dot{r} &= \psi\phi + H\chi + Hu + H\left(\rho_1\theta_1 + \rho_2\theta_2 - \hat{\rho}_1\hat{\theta}_1 - \rho_2\hat{\theta}_2\right) \\ &= \psi\phi + H\chi + Hu + H\rho_2\tilde{\theta}_2 + \\ &\quad H\left(\theta_{11}z - \hat{\theta}_{11}\hat{z} + \theta_{12}\nu z - \hat{\theta}_{12}\nu\hat{z} - \theta_{13}\left|\dot{x}_{mr}\right|z + \hat{\theta}_{13}\left|\dot{x}_{mr}\right|\hat{z}\right) \end{aligned} \tag{4.6}$$

For calculation simplicity, χ and u are defined as

$$\chi = \hat{\theta}_{11}\hat{z} - \hat{\theta}_{13}\left|\dot{x}_{mr}\right|\hat{z} + \hat{\theta}_{21}\dot{x}_{mr} \tag{4.7}$$

$$u = \left(\hat{\theta}_{12}\hat{z} + \hat{\theta}_{22}\dot{x}_{mr}\right)\nu \tag{4.8}$$

From the result of the stability analysis that explained detailed in the study of (Yıldız et al., 2015), the control input u was designed in the form of

$$Hu = -\left\{Kr + H\chi + \psi\hat{\phi} - H\left(-\hat{\theta}_{11}\zeta_1 - \hat{\theta}_{12}\zeta_2\nu + \hat{\theta}_{13}\left|\dot{x}_{mr}\right|\zeta_3\right)\right\} \tag{4.9}$$

Input voltages to each MR damper can be calculated by using equation (4.8) and (4.9).

$$H\nu = -\frac{Kr + H\chi + \psi\hat{\phi} + H\left(\hat{\theta}_{11}\zeta_1 - \hat{\theta}_{13}\left|\dot{x}_{mr}\right|\zeta_3\right)}{\left(\hat{\theta}_{12}\hat{z} + \hat{\theta}_{22}\dot{x}_{mr} + \hat{\theta}_{12}\zeta_2\right)} \tag{4.10}$$

The effectiveness of the adaptive controller is tested in the MATLAB-Simulink environment under the smooth curved track condition. The performance of the designed controllers is compared with the uncontrolled (MR damper is not connected) and the passive (MR damper is connected but no electricity is supplied) cases. Since a single MR damper cannot produce a sufficient damping force, a set of two MR dampers are used. The parameters used in simulations of the monorail vehicle are taken from the study conducted by [Lee et al., 2005].

As it can be seen in Figure 4.1 and Figure 4.2, monorail vehicle firstly runs on $\sigma = 50$ m straight segment, then $\sigma = 50$ m a clothoid curve is used to enable a gradual transition in lateral acceleration. After that, the vehicle negotiates 206 m circular curve with a radius of 150 m.

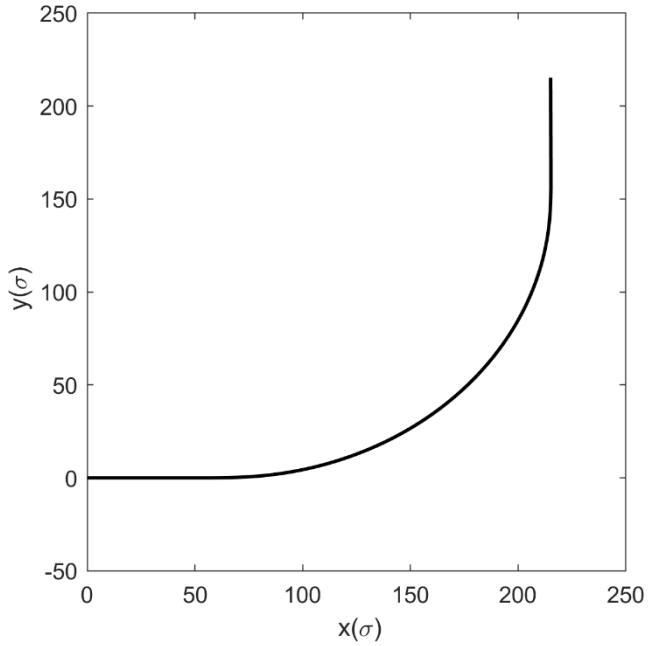

Figure 4.1: Top view of the designed road profile for simulations.

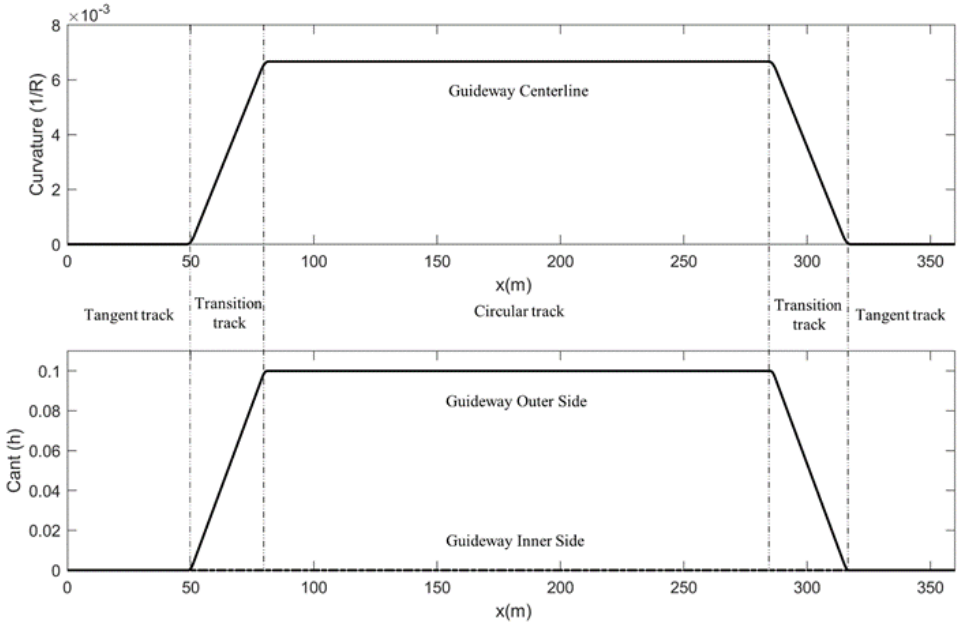

Figure 4.2: Curvature and cant of the road profile.

The root-mean-square and peak-to-peak values of the monorail body accelerations during the curving are obtained for the H∞ control, adaptive control and passive case and the results are shown in Table 4.1. Also, the reduction is given in per cent relative to the uncontrolled case. Negative reduction means the deterioration in the performance index. RMS value for the vehicle body acceleration is given in equation (4.11)

$$J_1 = \sqrt{\frac{1}{N}\sum_{n=1}^{N}\left|\ddot{z}_{11}(t)\right|^2},\ J_2 = \sqrt{\frac{1}{N}\sum_{n=1}^{N}\left|\ddot{y}_{11}(t)\right|^2},\ J_3 = \sqrt{\frac{1}{N}\sum_{n=1}^{N}\left|\ddot{\theta}_{x,z11}(t)\right|^2} \quad (4.11)$$

According to Table 4.1, it is observed that the adaptive controller reduced the RMS value of the roll acceleration to 115 % as compared to the uncontrolled case but increased vertical acceleration peak to peak (global minimum to global maximum) value to 60 %. This is due to the fact that the adaptive controller is designed to minimize displacement which causes undesirable peak acceleration.

Table 4.1: RMS and peak to peak values of the monorail body accelerations.
(unit: vertical, lateral- m/s^2; roll- rad/s^2; yaw- rad/s^2)

	RMS values			Peak to peak values		
	Passive	H∞	Adaptive	Passive	H∞	Adaptive
$\ddot{z}_{11}$	0.014	0.011	0.019	0.112	0.149	0.377
$\ddot{y}_{11}$	0.195	0.152	0.142	3.933	3.921	4.058
$\ddot{\theta}_{x11}$	0.173	0.123	0.113	1.563	1.524	1.306
$\ddot{\theta}_{z11}$	0.014	0.014	0.014	0.221	0.215	0.247
Reduction ($\ddot{z}_{11}$) %	49.47	79.66	6.036	32.88	-0.83	-60.60
Reduction ($\ddot{y}_{11}$)%	34.09	73.23	85.04	0.57	0.88	-2.54
Reduction ($\ddot{\theta}_{x11}$)%	41.13	97.87	115.47	7.32	10.06	28.50
Reduction ($\ddot{\theta}_{z11}$)%	2.27	2.32	2.52	2.43	4.86	-8.45

As seen in Figure 4.3 and Figure 4.4, vibration reduction ability of the semi-active suspension with the proposed control approaches is better than that of the passive suspension. Also, the adaptive controller can reduce the car body roll acceleration better than the passive and H∞ control cases as given in Table 4.1. Also, oscillations after the circular curve are eliminated. Improvement in the lateral motion of the vehicle also affects positively the vehicle rolling motion. This effect can be seen in Figure 4.3. Reduction in both rolling and lateral acceleration improve curving performance of the monorail vehicle.

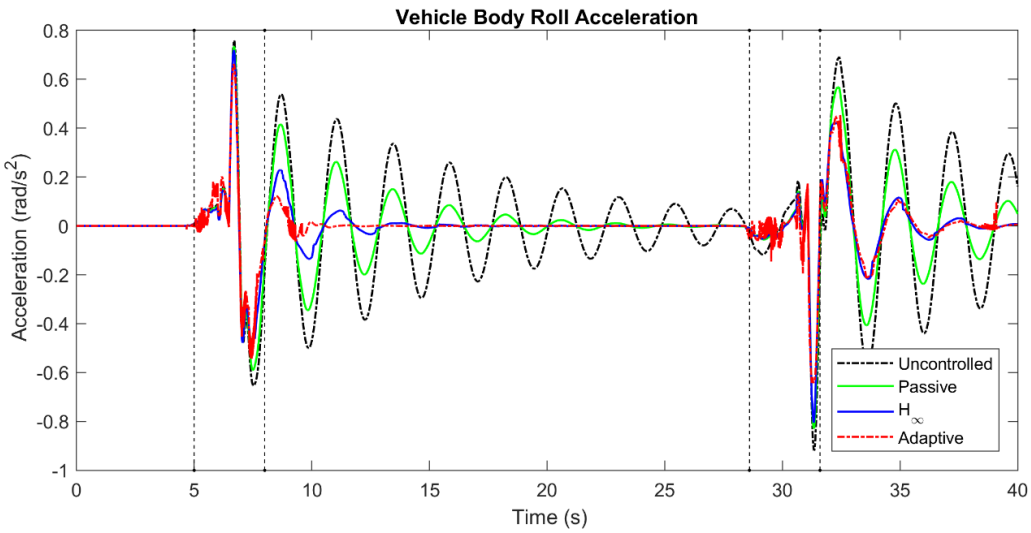

Figure 4.3: Vehicle body roll acceleration.

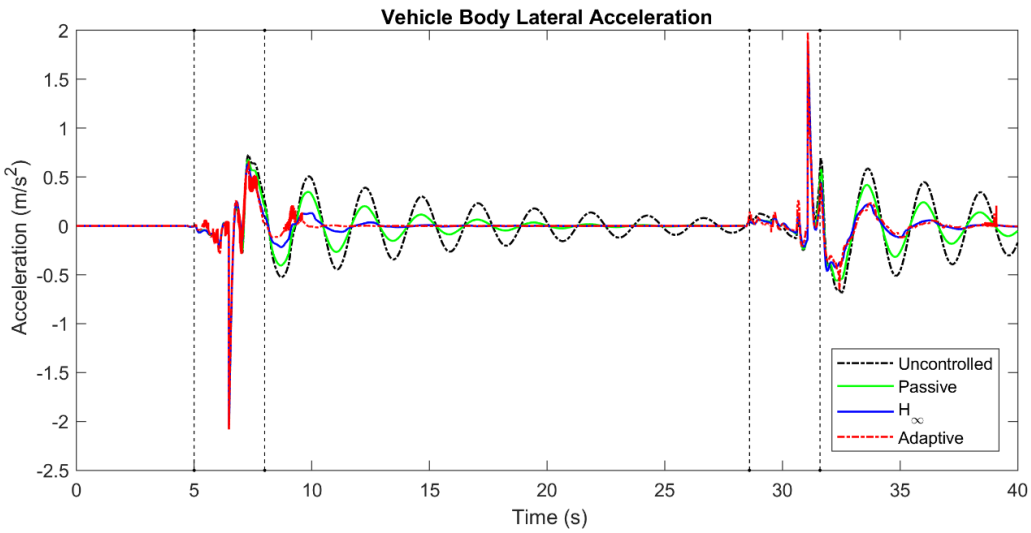

Figure 4.4: Vehicle body lateral acceleration.

The proposed control approaches reduce the vertical displacement of the monorail body displacements both entering the curve and the leaving curve as shown in Figure 4.5. Also, vibrations during the circular curve occur between 8th and 28.8th second are diminished. This improvement ends up with deterioration in vertical peak acceleration as seen in Table 4.1, also the same adverse effect can be seen in the vertical comfort value. However, H∞ control decreases both displacement and comfort index values.

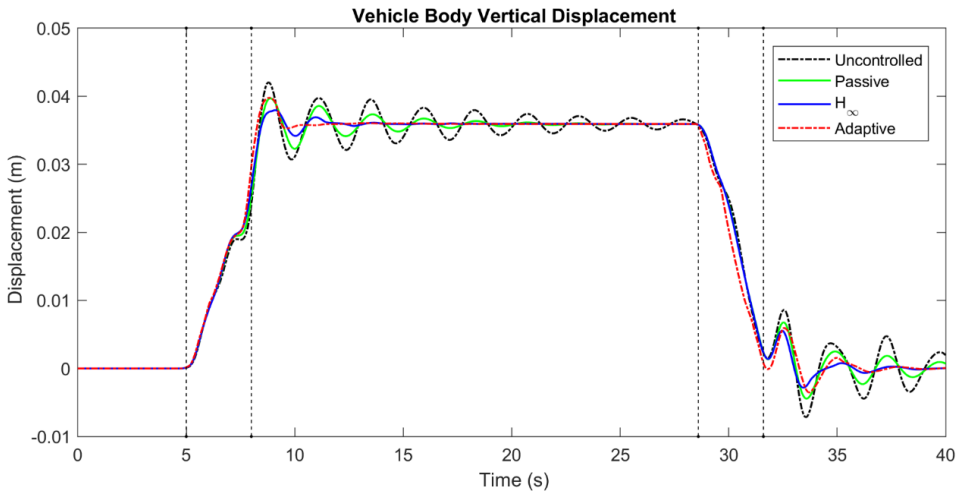

Figure 4.5: Vehicle body vertical displacement.

Figure 4.6 shows the time histories of the desired and actual forces of the H∞ control. The desired force is the force output of the reference system with optimal static feedback gain as defined in Appendix A, A2. It can be seen in Figure 4.6 that required force (expressed by a black dash-dot line) and the force produced by MR dampers with the H∞ controller is the same. It means that the required force is reproducible by the MR dampers. Also, the adaptive controller achieves better performance with almost the same force level.

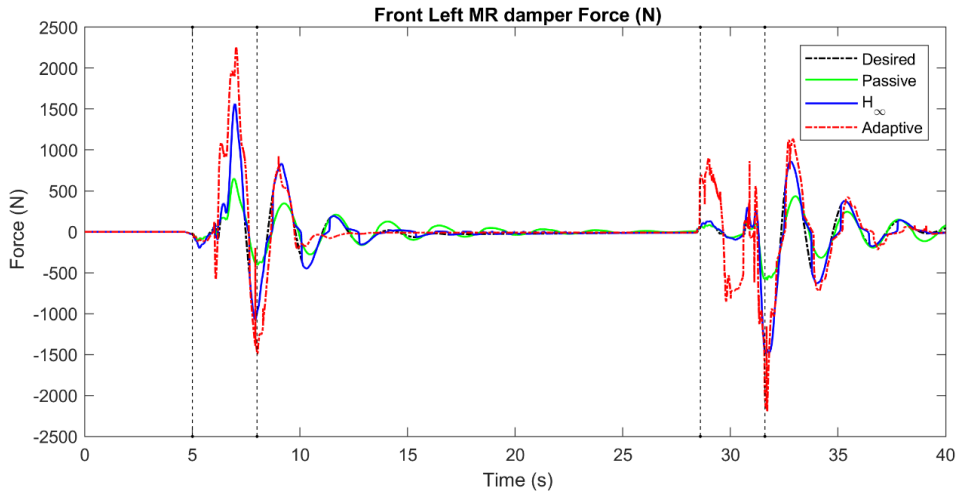

Figure 4.6: Force output of the MR damper placed at the left side of the front bogie.

4.1.1. Comparison of Ride Comfort

Ride comfort is measured by some specific indices by considering acceleration level, frequency, direction, and location. The International Standard [ISO 2631-1, 1997] specifies a method of evaluation of the effect exposure to vibration on humans by weighting RMS acceleration with human vibration-sensitivity curves.

$$a_w = \left[\frac{1}{T} \int_0^T a_w^{\,2}(t)\, dt \right]^{\frac{1}{2}} \tag{4.12}$$

where, a_w is the weighted acceleration as a function of time in meters per second squared (m/s^2) and T is the duration of the measurement in seconds. In this study, road roughness is not considered therefore all cases are in the *comfortable* limit of the scale defined by ISO 2631. The weighted RMS values of the overall comfort index are summarized in Table 4.2. As seen in Table 4.2, the adaptive control serves better comfort in the lateral direction but results in deterioration in the vertical comfort value.

Table 4.2: Effect of control approaches on ride comfort: weighted RMS values (m/s^2).

	Uncontrolled	Passive	H∞ Control	Adaptive Control
Vertical	0.0085	0.0058	0.0055	0.0081
Lateral	0.1951	0.1466	0.1141	0.1032

Figure 4.7. shows the vertical and lateral comfort index that calculated at 1s intervals. Both vertical and lateral comfort indices are majorly influenced by the transition track segment. One can see that the H∞ control provides better vertical comfort when compared to other cases, but the adaptive control achieves better comfort in lateral direction.

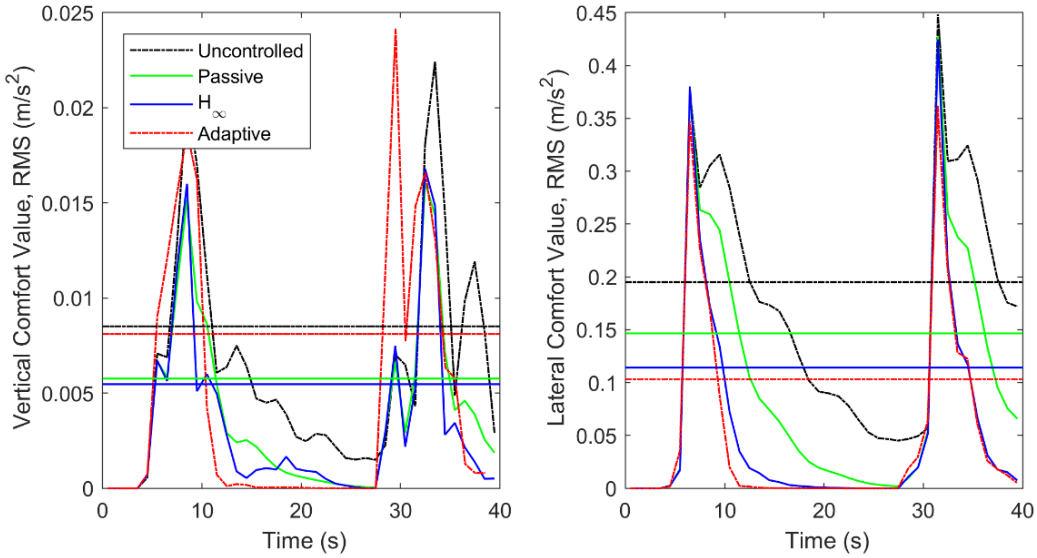

Figure 4.7: Vertical and lateral comfort values.

4.1.2. Comparison of Curving Performance

Curving performance is evaluated by using the bogie lateral displacement. As seen in Figure 4.8, the peak value of the front bogie lateral displacement is decreased with the designed controllers. This decrement may also provide an extended service life to running tires because the lower lateral displacements cause lower abrasion on tires. Also, the vertical load acts on the tyre contact surface is a rational cause of wear. Higher loads make greater deformations on tire treads which causes wear. Figure 4.9 shows the decrement in vertical tire force.

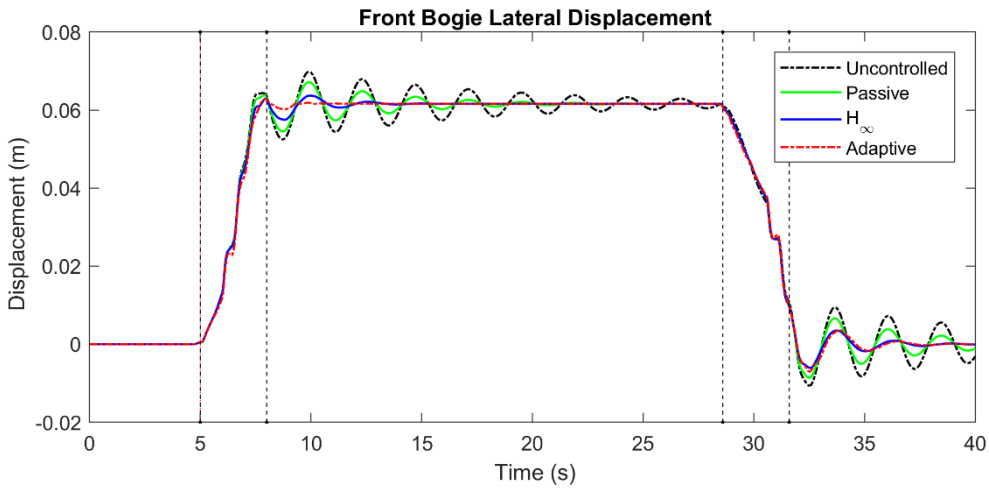

Figure 4.8: Front bogie inner side running tire lateral displacement.

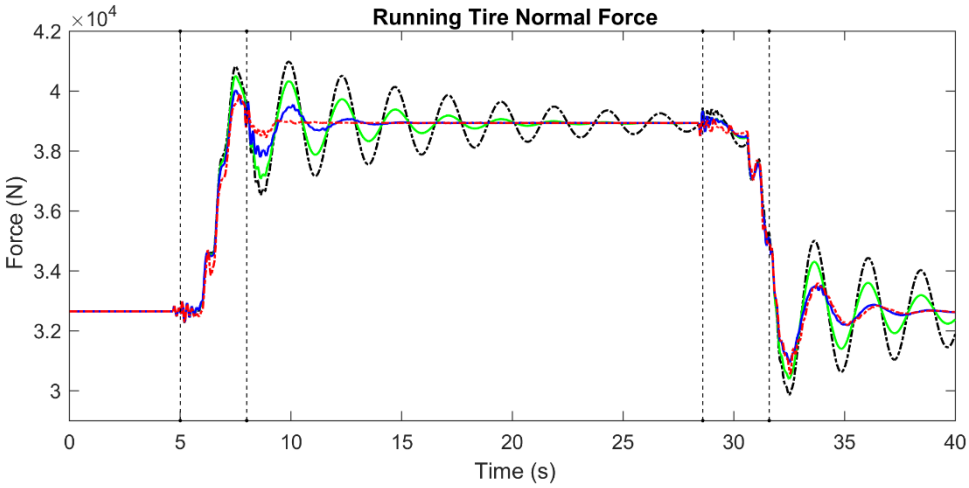

Figure 4.9: Front bogie inner side running tire vertical force.

4.1.3. Parameter Adaptation Performance

In monorail vehicles, running on rubber tires causes abrasion. Also, existing uncertainties in a monorail vehicle influence the performance of suspension systems. Therefore, system parameters related to tire dynamics should be modelled by considering these uncertainties. In the designed adaptive control, mass, damping and stiffness parameters are guaranteed to converge to their true value under a persistent excitation condition when associated adaptation gain adjusted. In the adaptive control and H_∞ control design, we assume 10 % uncertainties in mass properties of the vehicle which corresponding to full load and no passenger cases. Also, 15 % uncertainties in running tire parameters is assumed (both damping and stiffness properties) because of running tires runs under higher abrasion condition. The convergence behaviour is summarized in Figure 4.10 and Figure 4.11.

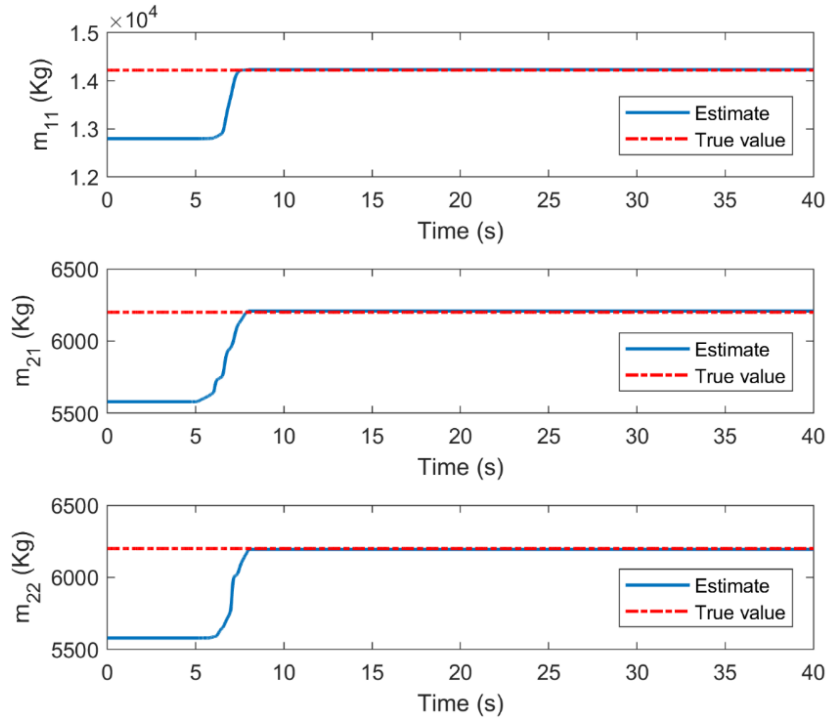

Figure 4.10: Estimation behavior of the monorail mass values to their true values.

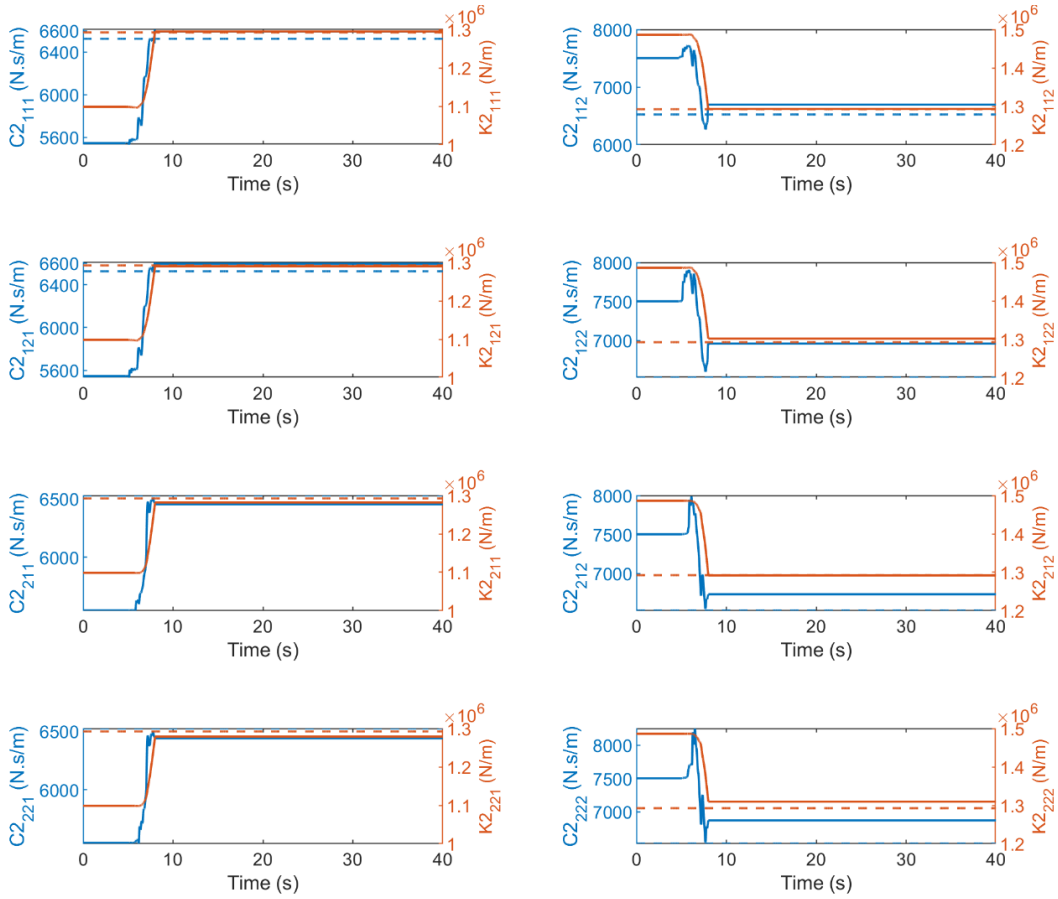

Figure 4.11: Estimation of the damping and stiffness parameters to their real values.

4.2. Adaptive Backstepping Control Design Based on BLF

In this subsection, the proposed constrained adaptive backstepping control approach that deals with uncertain suspension parameter are explained. The control strategy is performed for a single MR damper that may be placed next to the vertical or lateral air suspensions while the rest are assumed to be stationary. By this way, six separate control strategies for the MR dampers are coupled to each other. When the displacement of the upper and lower attachment points of the MR damper are denoted by x_1 and x_3 , respectively, the backstepping control strategy is presented as follows, Firstly, the regulated variable is selected as;

$$z_1 = x_1 - \bar{x}_3 \tag{4.13}$$

where, $\bar{x}_3$ stands for the filtered version of the lower attachment point displacement. This filter can be considered a first-order lowpass filter as given in equation (4.14) whose cut-off frequency h , changes with respect to a positive constant ε , a positive scale factor K_1 , and a function $\varphi(S)$ depends on the suspension working space S , as given in equation (4.15),

$$\bar{x}_3 = \frac{h}{s+h} x_3 \tag{4.14}$$

Also, the filter can be written in the time domain by using the inverse Laplace transform,

$$\dot{\bar{x}}_3 = \underbrace{\left(\varepsilon + K_1 \varphi(S)\right)}_{h} \left(x_3 - \bar{x}_3\right) \tag{4.15}$$

Here, for the high values of the h most of the high-frequency component of the x_3 passes the filter then the regulated variable, z_1 , converges to the suspension travel, $(x_1 - x_3)$. In the case of the small value of h , most of the signal is eliminated by the filter and regulated variable gets closer to sprung mass displacement signal, x_1 . By this

means, a compromise between the ride quality and suspension deflection is provided by a single variable [Lin and Huang, 2003]. The nonlinear function is defined as

$$\varphi(S)=\begin{cases}\left(\dfrac{S-m_1}{m_2}\right)^2 & S\geq m_1\\ 0 & |S|\leq m_1\\ \left(\dfrac{S+m_1}{m_2}\right)^2 & S\leq -m_1\end{cases} \tag{4.16}$$

A filter design example for the MR damper which has a maximum working space of ± 25 mm is given in Figure 4.12 with the parameter influence on the filter response. As it can be seen in Figure 4.12.a), the m_1 value specifies the dead-zone of the function where the only ε has an effect on the filter response. In this region, comfort-oriented design can be provided with the selection of small ε value. Also, the reaction characteristic of the filter, when the specified limit is exceeded, can be determined by the m_2 value. For the small value of m_2, controller tries to keep rattle space usage within its limits aggressively as seen in Figure 4.12.b). In addition, the effective bandwidth of the filter can be scaled by K_1 when the dead-zone is exceeded. Also, the small value of m_1 and m_2 should not be selected unless the vehicle runs on an unpredictable severe road condition to avoid discomfort.

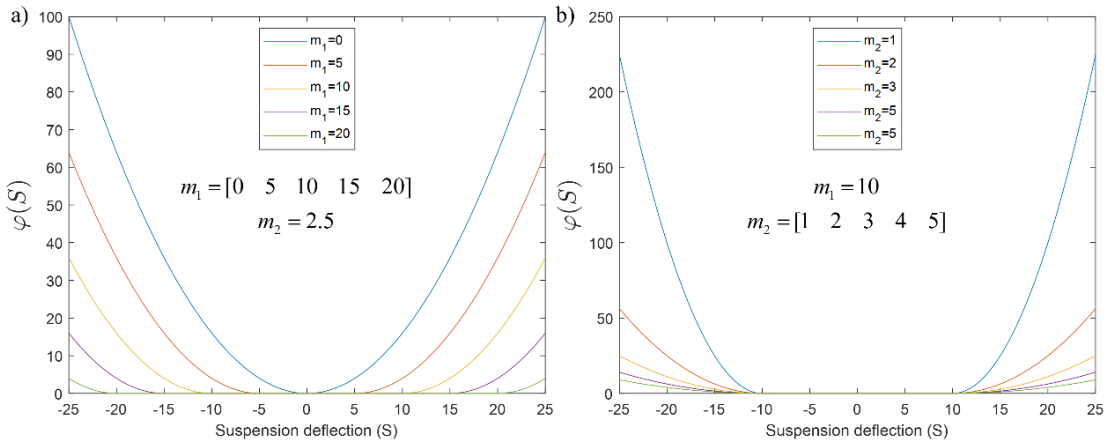

Figure 4.12: Nonlinear filter function response: a) Effect of the dead zone and b) Effect of the exceeded limits.

Derivative of the regulated variable can be written as,

$$\dot{z}_1 = \dot{x}_1 - \dot{\bar{x}}_3$$
$$\dot{z}_1 = x_2 - \left(\varepsilon + K_1\varphi\left(S\right)\right)\left(x_3 - \bar{x}_3\right) \tag{4.17}$$

If x_2 that represents the velocity of the upper attachment point is considered as a virtual control variable, the corresponding error variable is defined as

$$z_2 = x_2 - \alpha \tag{4.18}$$

Here z_2 can be assumed as an error variable representing the difference between the actual and virtual control and α is a stabilizing function to be designed. The Barrier Lyapunov Function candidate is chosen as follows

$$V_1 = \frac{1}{2}\log\left(\frac{m_1^{\ 2}}{m_1^{\ 2} - z_1^{\ 2}}\right) \tag{4.19}$$

Derivative of the Lyapunov function becomes,

$$\dot{V}_1 = \frac{z_1\dot{z}_1}{m_1^{\ 2} - z_1^{\ 2}} = \frac{z_1}{m_1^{\ 2} - z_1^{\ 2}}\left(\left(z_2 + \alpha\right) - h\left(z_1 - S\right)\right) \tag{4.20}$$

Here the stabilizing function α is designed as

$$\alpha = h\left(z_1 - S\right) - \kappa_1 z_1\left(m_1^{\ 2} - z_1^{\ 2}\right) \tag{4.21}$$

where κ_1 is a positive value, then substituting the stabilizing function signal of equation (4.21) into (4.20), derivative of the Lyapunov function becomes as

$$\dot{V}_1 = -\kappa_1 z_1^{\ 2} + \frac{z_1 z_2}{m_1^{\ 2} - z_1^{\ 2}} \tag{4.22}$$

Apparently, if $z_2 = 0$, then $\dot{V}_1 = -\kappa_1 z_1^{\ 2} \le 0$ and the regulated variable asymptotically converges to zero. In order to ensure this condition, the control input should be selected properly manner. The acceleration expression for the upper suspension connection point on the vehicle frame can be written by using equation (2.29) and (2.33) as follows

$$\begin{aligned} \dot{x}_2 &= \underbrace{\ddot{z}_{11} - (-1)^n \ddot{\theta}_{x11} L_{vy2} + (-1)^i \ddot{\theta}_{y11} L_{vxi}}_{Y\phi + hf} \qquad \text{for vertical dampers} \\ \dot{x}_2 &= \underbrace{\ddot{y}_{11} + \ddot{\theta}_{x11} L_{z1} - (-1)^i \ddot{\theta}_{z11} L_{xi}}_{Y\phi + hf} \qquad \text{for lateral dampers} \end{aligned} \tag{4.23}$$

Using equation (4.23), the time derivative of the error variable that defined in (4.18) can be written as

$$\begin{aligned} \dot{z}_2 &= \dot{x}_2 - \dot{\alpha} \\ &= Y\phi + hf - \dot{\alpha} \end{aligned} \tag{4.24}$$

Here force expression f cannot be used directly because of the containing uncertain parameter. Adding and subtracting estimated force expression $h\hat{f}$ term to the right side of the derivative of the $\dot{z}_2$ leads to

$$\dot{z}_2 = Y\phi - \dot{\alpha} + h\hat{f} + h\left(f - \hat{f} \right) \tag{4.25}$$

rewriting the equation (4.25) with equation (2.9) leads to

$$\dot{z}_2 = Y\phi - \dot{\alpha} + h\gamma + hu + h\left(\rho_1\theta_1 + \rho_2\theta_2 - \hat{\rho}_1\hat{\theta}_1 - \rho_2\hat{\theta}_2 \right) \tag{4.26}$$

For the sake of simplicity, $\gamma = \hat{\theta}_{11}\hat{z} - \hat{\theta}_{13}\left|\dot{S}\right|\hat{z} + \hat{\theta}_{21}\dot{S}$ and $u = \left(\hat{\theta}_{12}\hat{z} + \hat{\theta}_{22}\dot{S}\right)\nu$ is defined. Above form can be rewritten more clearly as given in equation (4.27).

$$\dot{z}_2 = Y\phi - \dot{\alpha} + h\gamma + hu + h\rho_2\tilde{\theta}_2 + h\left(\theta_{11}z - \hat{\theta}_{11}\hat{z} + \theta_{12}vz - \hat{\theta}_{12}v\hat{z} - \theta_{13}\left|\dot{S}\right|z + \hat{\theta}_{13}\left|\dot{S}\right|\hat{z} \right) \tag{4.27}$$

Considering subsequent stability analysis the control input is designed as

$$hu = -\left\{\kappa_2 z_2 + h\gamma + Y\hat{\phi} - h\left(-\hat{\theta}_{11}\zeta_1 - v\hat{\theta}_{12}\zeta_2 + \left|\dot{S}\right|\hat{\theta}_{13}\zeta_3\right)\right\} + \dot{\alpha} - \frac{z_1}{m_1^{\,2} - z_1^{\,2}} \tag{4.28}$$

The control voltage to the MR damper v, can be derived from equation (4.28) as defined in equation (4.29). Here the denominator of equation (4.29) should be artificially removed from zero to avoid irrationality.

$$hv = \frac{-\kappa_2 z_2 - h\gamma - Y\hat{\phi} - h\hat{\theta}_{11}\zeta_1 + h\left|\dot{S}\right|\hat{\theta}_{13}\zeta_3 + \dot{\alpha} - \dfrac{z_1}{m_1^{\,2} - z_1^{\,2}}}{\left(\hat{\theta}_{12}\hat{z} + \hat{\theta}_{22}\dot{S} + \hat{\theta}_{12}\zeta_2\right)} \tag{4.29}$$

Substituting the control input signal of equation (4.29) into the error defined in equation (4.27) yields

$$\begin{aligned}\dot{z}_2 = &-\kappa_2 z_2 + Y\tilde{\phi} + h\rho_2\tilde{\theta}_2 + h\left[\theta_{11}z - \hat{\theta}_{11}\left(\hat{z} - \zeta_1\right)\right] + h\left[v\theta_{12}z - v\hat{\theta}_{12}\left(\hat{z} - \zeta_2\right)\right] \\ &- h\left[\theta_{13}\left|\dot{S}\right|z - \hat{\theta}_{13}\left|\dot{S}\right|\left(\hat{z} - \zeta_3\right)\right] - \frac{z_1}{m_1^{\,2} - z_1^{\,2}}\end{aligned} \tag{4.30}$$

Adding and subtracting, $\pm h\left[\theta_{11}\left(\hat{z} + \zeta_1\right)\right]$, $\pm h\left[v\theta_{12}\left(\hat{z} + \zeta_2\right)\right]$, $\pm h\left[\left|\dot{S}\right|\theta_{13}\left(\hat{z} + \zeta_3\right)\right]$ terms to the right-hand side of equation (4.30), and rearranging the terms. The final form of the error signal becomes as follows

$$\begin{aligned}\dot{z}_2 = &-\kappa_2 z_2 + Y\tilde{\phi} + h\rho_2\tilde{\theta}_2 - \frac{z_1}{m_1^{\,2} - z_1^{\,2}} + h\left[\theta_{11}\left(\tilde{z} - \zeta_1\right) + \tilde{\theta}_{11}\left(\hat{z} + \zeta_1\right)\right] \\ &+ h\left[\theta_{12}v\left(\tilde{z} - \zeta_2\right) + \tilde{\theta}_{12}v\left(\hat{z} + \zeta_2\right)\right] - h\left[\theta_{13}\left|\dot{S}\right|\left(\tilde{z} - \zeta_3\right) + \tilde{\theta}_{13}\left|\dot{S}\right|\left(\hat{z} + \zeta_3\right)\right]\end{aligned} \tag{4.31}$$

- ***Observer formulation***

To express the predicted force, it is necessary to define an observer for the inner variable z.

If the positive parameter a_0 defined in equation (2.7) is assumed to be known, the following observer is defined for the $z(t)$

$$\dot{\hat{z}} = \dot{S} - a_0 \left|\dot{S}\right| \hat{z} \tag{4.32}$$

And the observation error can be defined as $\tilde{z} = z - \hat{z}$,

$$\dot{\tilde{z}} = -a_0 \left|\dot{S}\right| \tilde{z} \tag{4.33}$$

- ***Stability Analysis***

Firstly, we should define a candidate Lyapunov function that includes all states and error dynamics in the closed-loop system. The Lyapunov function is selected as

$$\begin{aligned} V_2 &= V_1 + \frac{1}{2} z_2^{\,2} + \frac{1}{2}\tilde{z}^2 + \frac{1}{2}\tilde{\phi}^T \Gamma_1^{\,-1} \tilde{\phi} + \frac{1}{2}\theta_2^{\,T} \Gamma_2^{\,-1} \theta_2 + \frac{1}{2\gamma_1}\theta_{11}^{\,2} \\ &+ \frac{1}{2\gamma_2}\theta_{12}^{\,2} + \frac{1}{2\gamma_3}\theta_{13}^{\,2} + \frac{1}{2}\theta_{11}\left(\tilde{z} - \zeta_1\right)^2 + \frac{1}{2}\theta_{12}\left(\tilde{z} - \zeta_2\right)^2 + \frac{1}{2}\theta_{13}\left(\tilde{z} - \zeta_3\right)^2 \end{aligned} \tag{4.34}$$

where Γ_1 and Γ_2 are positive definite diagonal adaptation gain matrices; γ_1 , γ_2 and γ_3 are the positive adaptation gains. When the equation (4.22) is substituted into the derivative of the Lyapunov function it becomes,

$$\begin{aligned} \dot{V}_2 &= -\kappa_1 z_1^{\,2} + \frac{z_1 z_2}{m_1^{\,2} - z_1^{\,2}} + z_2 \dot{z}_2 + \tilde{z}\,\dot{\tilde{z}} + \tilde{\phi}^T \Gamma_\phi^{\,-1} \dot{\tilde{\phi}} + \tilde{\theta}_2^T \Gamma_2^{\,-1} \dot{\tilde{\theta}}_2^{\,T} \\ &+ \frac{1}{\gamma_1}\tilde{\theta}_{11}\dot{\tilde{\theta}}_{11} + \frac{1}{\gamma_2}\tilde{\theta}_{12}\dot{\tilde{\theta}}_{12} + \frac{1}{\gamma_3}\tilde{\theta}_{13}\dot{\tilde{\theta}}_{13} \\ &+ \theta_{11}\left(\tilde{z} - \zeta_1\right)\left(\dot{\tilde{z}} - \dot{\zeta}_1\right) + \theta_{12}\left(\tilde{z} - \zeta_2\right)\left(\dot{\tilde{z}} - \dot{\zeta}_2\right) + \theta_{13}\left(\tilde{z} - \zeta_3\right)\left(\dot{\tilde{z}} - \dot{\zeta}_3\right) \end{aligned} \tag{4.35}$$

If the final form of the error signal defined in equation (4.31) and the observation error defined in equation (4.33) substituted into equation (4.35), it is obtained that

$$\dot{V}_2 = -\kappa_1 z_1^{\ 2} + z_2^{\ T} \begin{Bmatrix} -\kappa_2 z_2 + Y\tilde{\phi} + h\rho_2\tilde{\theta}_2 + h\left[\theta_{11}\left(\tilde{z}-\zeta_1\right)+\tilde{\theta}_{11}\left(\hat{z}+\zeta_1\right)\right] \\ +h\left[\theta_{12}v\left(\tilde{z}-\zeta_2\right)+\tilde{\theta}_{12}v\left(\hat{z}+\zeta_2\right)\right] \\ -h\left[\theta_{13}\left|\dot{S}\right|\left(\tilde{z}-\zeta_3\right)+\tilde{\theta}_{13}\left|\dot{S}\right|\left(\hat{z}+\zeta_3\right)\right] \end{Bmatrix} \tag{4.36}$$
$$+\tilde{z}.\left\{-a_0\left|\dot{S}\right|\tilde{z}\right\} + P'$$

For the sake of clarity, P' is defined as given in equation (4.37).

$$\begin{aligned} P' &= \tilde{\phi}^T\Gamma_{\phi}^{\ -1}\dot{\tilde{\phi}} + \tilde{\theta}_2^T\Gamma_2^{\ -1}\dot{\tilde{\theta}}_2^{\ T} + \frac{1}{\gamma_1}\tilde{\theta}_{11}\dot{\tilde{\theta}}_{11} + \frac{1}{\gamma_2}\tilde{\theta}_{12}\dot{\tilde{\theta}}_{12} + \frac{1}{\gamma_3}\tilde{\theta}_{13}\dot{\tilde{\theta}}_{13} \\ &+\theta_{11}\left(\tilde{z}-\zeta_1\right)\left(\dot{\tilde{z}}-\dot{\zeta}_1\right)+\theta_{12}\left(\tilde{z}-\zeta_2\right)\left(\dot{\tilde{z}}-\dot{\zeta}_2\right)+\theta_{13}\left(\tilde{z}-\zeta_3\right)\left(\dot{\tilde{z}}-\dot{\zeta}_3\right) \end{aligned} \tag{4.37}$$

To ensure the error signal converges to zero, gradient-based update laws chosen

$$\begin{aligned} \dot{\tilde{\phi}} &= -\dot{\hat{\phi}} = -\Gamma_{\phi}Y^T z_2 \\ \dot{\tilde{\theta}}_2 &= -\dot{\hat{\theta}}_2 = -\Gamma_2\rho_2^{\ T} h\, z_2 \\ \dot{\tilde{\theta}}_{11} &= -\dot{\hat{\theta}}_{11} = -\gamma_1\left(\hat{z}+\zeta_1\right)h\, z_2 \\ \dot{\tilde{\theta}}_{12} &= -\dot{\hat{\theta}}_{12} = -\gamma_2 v\left(\hat{z}+\zeta_2\right)h\, z_2 \\ \dot{\tilde{\theta}}_{13} &= -\dot{\hat{\theta}}_{13} = \gamma_3\left|\dot{S}\right|\left(\hat{z}+\zeta_3\right)h\, z_2 \end{aligned} \tag{4.38}$$

If the adaptation terms put into equation (4.36), it becomes

$$\begin{aligned} \dot{V}_2 &= -\kappa_1 z_1^{\ 2} - \kappa_2 z_2^{\ 2} - a_0\left|\dot{S}\right|\tilde{z}^2 \\ &+z_2^{\ T}\left\{h\left[\theta_{11}\left(\tilde{z}-\zeta_1\right)\right]+h\left[\theta_{12}v\left(\tilde{z}-\zeta_2\right)\right]-h\left[\theta_{13}\left|\dot{S}\right|\left(\tilde{z}-\zeta_3\right)\right]\right\} \\ &+\theta_{11}\left(\tilde{z}-\zeta_1\right)\left(\dot{\tilde{z}}-\dot{\zeta}_1\right)+\theta_{12}\left(\tilde{z}-\zeta_2\right)\left(\dot{\tilde{z}}-\dot{\zeta}_2\right)+\theta_{13}\left(\tilde{z}-\zeta_3\right)\left(\dot{\tilde{z}}-\dot{\zeta}_3\right) \end{aligned} \tag{4.39}$$

Then the auxiliary filters can be designed according to the following formulation

$$
\begin{aligned}
\dot{\zeta}_1 &= h\, z_2 - a_0 \left|\dot{S}\right| \zeta_1 \\
\dot{\zeta}_2 &= v\, h\, z_2 - a_0 \left|\dot{S}\right| \zeta_2 \\
\dot{\zeta}_3 &= -\left|\dot{S}\right| h\, z_2 - a_0 \left|\dot{S}\right| \zeta_3
\end{aligned}
\tag{4.40}
$$

Substituting auxiliary filters in the derivative of Lyapunov function defined in equation (4.39), finally, we have

$$
\begin{aligned}
\dot{V}_2 = -\kappa_1 z_1^{\,2} - \kappa_2 z_2^{\,2} - a_0 \left|\dot{S}\right| \tilde{z}^2 - a_0 \left|\dot{S}\right| \theta_{11} \left(\tilde{z} - \zeta_1\right)^2 \\
- a_0 \left|\dot{S}\right| \theta_{12} \left(\tilde{z} - \zeta_2\right)^2 - a_0 \left|\dot{S}\right| \theta_{13} \left(\tilde{z} - \zeta_3\right)^2
\end{aligned}
\tag{4.41}
$$

The last four terms in equation (4.41) are always negative, we can further upper bound the time derivative of $V_2\left(t\right)$ to have the form

$$
\dot{V}_2 \le -\kappa_1 z_1^{\,2} - \kappa_2 z_2^{\,2} \tag{4.42}
$$

As a result, if the control gains κ_1 and κ_2 are selected positive definite, the right side of the equation (4.42) is always negative. When we consider the Lyapunov function defined in equation (4.34) and its derivative in equation (4.42), since $V_2 \in L_\infty$ is a bounded function, terms that are related to this function $z_1(t)$, $z_2(t)$, $\tilde{z}$, $\tilde{\phi}$ and $\tilde{\theta} \in L_\infty$ are also bounded. By signal tracking, it is shown that all the signals in the closed-loop system are bounded. The expression in equation (4.42) guarantees the global asymptotic convergence of tracking error and the boundedness of all signals. The QLF based adaptive control approach for the comparison purpose was explained in Appendix A, A4.

4.2.1. A Numerical Study of the Proposed Control Approaches

Proposed control methods are implemented in MATLAB environment by using the vehicle model which is established in Section 2. The horizontal road profile used in comparative control study that runs in MATLAB consists of 50 m straight segment

and circular curve radius of 350 m, 200m and 150 m. Also, the superelevation values are selected as, 2.92 %, 5.1 % and 6.8 % for the corresponding circular curves. Also, the track beam surface irregularity is constituted by ISO 8608 classification.

It can be observed from Table 4.3 that H∞ control can attenuate the vertical acceleration better than the adaptive controllers. However, BLF based backstepping control performs better displacement performance when compared to other cases as seen in Figure 4.13. This can be explained by the fact that both adaptive and backstepping controllers aimed to reduce displacement related dynamics. Therefore, acceleration related dynamics are disregarded. However, % 6.6 and % 5.8 improvements are achieved in the vertical acceleration of the monorail vehicle in case of QLF and BLF based controller when compared to uncontrolled case. Also, the proposed BLF controller achieved the best performance in terms of lateral acceleration as % 66 improvement is achieved. Detailed simulation study will be conducted by experimentally in Section 5 and the co-simulation tool will be utilized to take into consideration the nonlinear tire model in Section 6.

Table 4.3: RMS values of the monorail body accelerations.

(unit: vertical, lateral- m/s^2)	RMS values			
	H∞ position	H∞ acc.	QLF	BLF
$\ddot{z}_{11}$	0.0375	0.0361	0.0459	0.0462
$\ddot{y}_{11}$	0.0656	0.0586	0.0880	0.0586
Reduction ($\ddot{z}_{11}$) %	30.203	35.537	6.589	5.842
Reduction ($\ddot{y}_{11}$) %	48.294	65.977	10.564	66.137

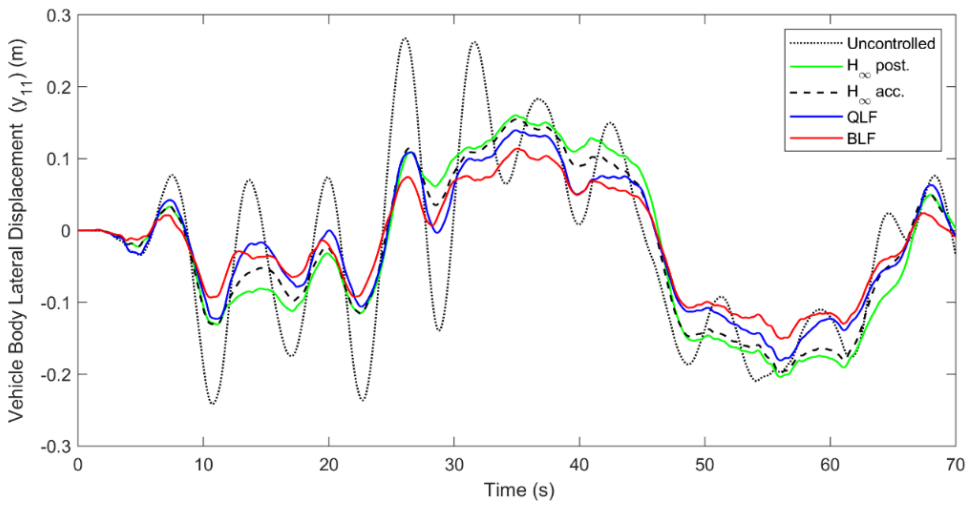

Figure 4.13: Monorail body lateral displacement on the route.

5. VALIDATION OF THE PROPOSED CONTROL APPROACHES ON TEST SETUP

In this section, constrained adaptive backstepping control design is implemented experimentally for the vibration suppression of the quarter-vehicle system equipped with magnetorheological damper. The test-rig cannot give idea about the curving performance of the monorails. By this test-rig, only the vertical oscillating behavior of the vehicle model can be investigated for each suspension system, and this simplified model gives intuitive insights into suspension control performance of the monorail vehicle. The quarter-vehicle system has been used for the control performance evaluation of the rail vehicles suspension system [Orvnäs et al., 2011], [Atray et al., 2004]. Also, the effectiveness of the proposed control designs has been validated in experimental studies through comparisons with uncontrolled, passive and adaptive control based on QLF cases. Here, uncontrolled correspond to the suspension system without MR damper and passive stands for the case when the MR damper is supplied with constant 1.5 V. Experimental results show that the adaptive controllers are able to achieve good performance in road holding and driving comfort despite uncertainties in model parameters.

5.1. Experimental System

The quarter car test system that was used for the experimental control study is shown in Figure 5.1 with its components. Displacement information of each masses and the road surface profile are provided by the Waycon SM series LVDT's (Linear Variable Differential Transformer) and Brüel&Kjaer 4507-B-002 series accelerometer are used for the investigating ride comfort measures of the controllers. Also, the data flow between the attached devices such as the sensors, actuators with the controller is schematically shown in Figure 5.2. Electrical signals generated by the sensors were transmitted to the signal conditioning unit then acquired by the Quanser Q8-USB via analogue-to-digital (A/D) converters.

The designed multi-objective controller is implemented in the Quanser Q8-USB control card. The proposed control approach calculates command voltage directly. This signal is sent to the MR damper via an MR damper driver. The sampling rate is

chosen as 250 Hz (4ms) for all signals. To create a road profile, a servo motor (Panasonic MSME 750W AC) was used, also, for the raising output torque, a gearbox (1:5) was mounted to the servo motor. Also, a ball-screw mechanism was used to convert rotational motion to linear motion. The system parameters of the quarter-car test system are given in Table 5.1.

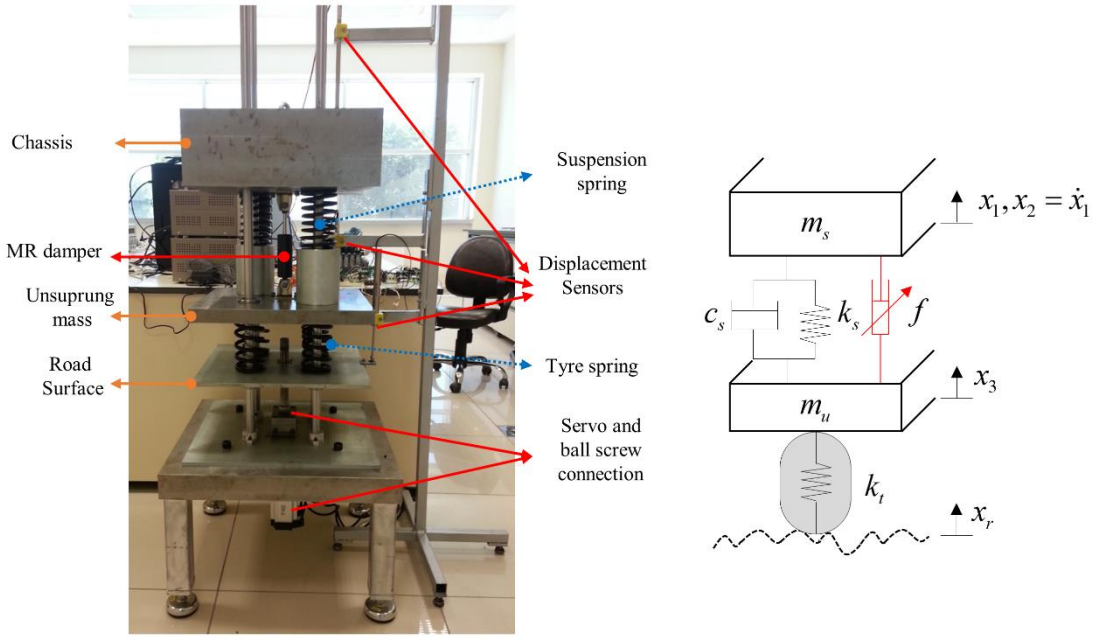

(a) (b)

Figure 5.1: Experimental Quarter car setup.

Table 5.1: Parameters of the quarter car model.

Symbol	Description	Values	Initial BLF	Initial QLF	Units
m_s	Sprung mass	248	-	210.8	Kg
m_u	Unsprung mass	70.1	-	59.5850	Kg
c	Structural damping	250	287.5	287.5	Ns/m
k_s	Suspension stiffness coefficient	18144	15422	20866	N/m
k_t	Tire stiffness coefficient	203860	-	234439	N/m

In order to evaluate the controller performance in different road excitation, three types of road profiles are constructed as given in Figure 5.3. In the first scenario, it is assumed that the vehicle runs on a road profile of ISO B-grade at speed of 10 m/s. After the steep ramp stage, a bump input adopted to investigate the transient response.

It can be noticed that the high-frequency components of the random road cannot be realized exactly by the test rig because of its mechanical limitations

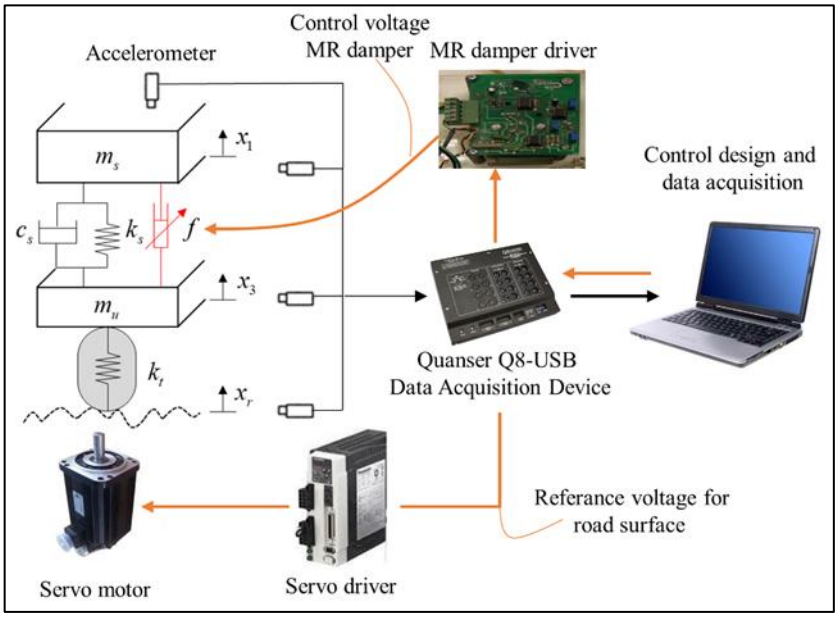

Figure 5.2: Schematic diagram of the experimental setup.

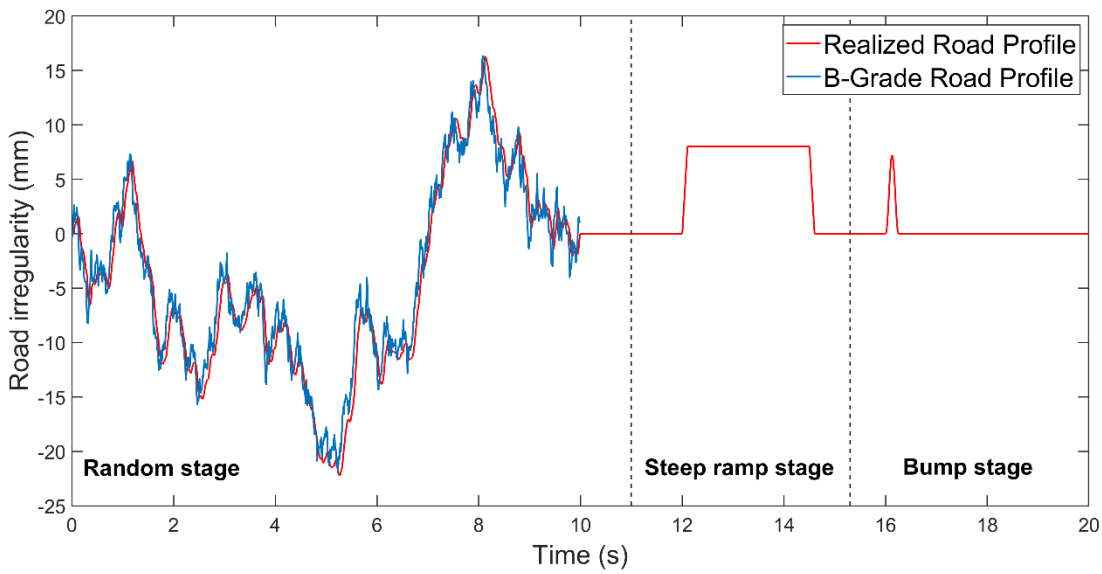

Figure 5.3: Experimentally realized the road profile and B-grade road profile.

To confirm the selected nominal value of system parameters and the MR damper parameter, power spectral density (PSD) of the sprung mass acceleration was compared as given in Figure 5.4, the results are in close agreement leading to the conclusion that the constructed model can be used in control design studies.

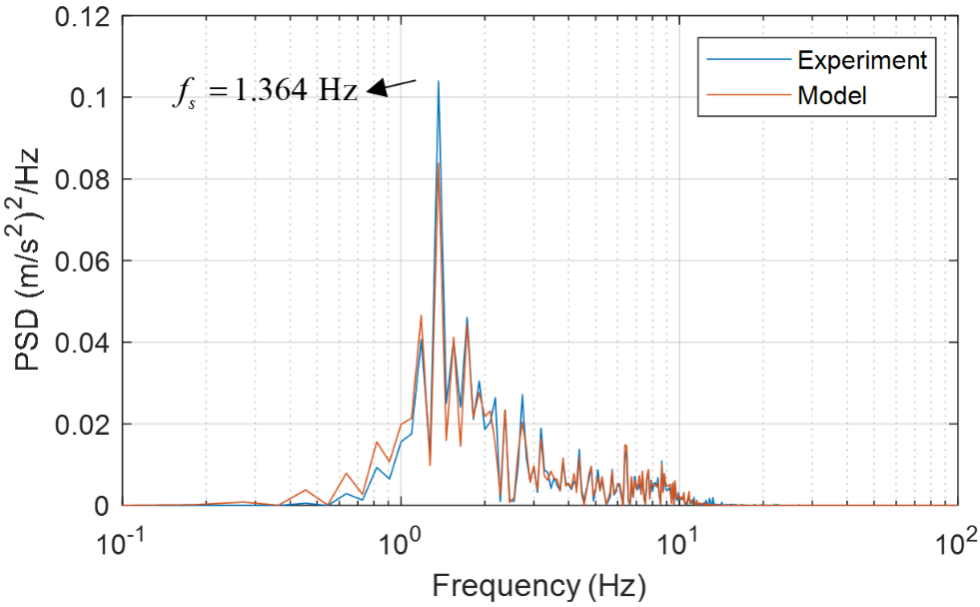

Figure 5.4: Vertical acceleration spectrum of the simulated model and the experimental system.

As shown in Figure 5.5, the adaptive controller (QLF) provides a better result in terms of overshoot on the steep ramp and bump stages but oscillations of after the sudden input is absorbed faster by the backstepping controller. In addition, QLF based controller is not guaranteed the required performance constraints such as suspension rattle space usage. Also, it can be observed that BLF control reduces the chassis vertical displacement in the random stage when compared to QLF control and passive case.

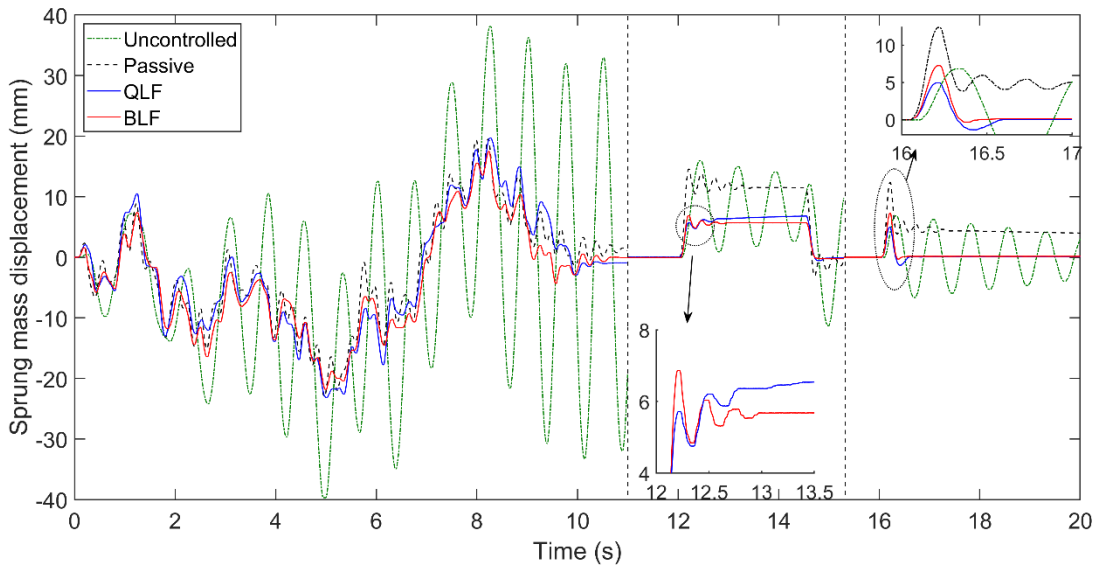

Figure 5.5: Vehicle body displacement.

In the vehicle dynamic, it is important to decrease the unsprung mass vibration for ensuring the tire-road contact while driving on an uneven road. Also, there is a trade-off between comfort and handling. As it can be seen in Figure 5.6, the backstepping control produces better vibration attenuation performance when compared to its counterparts.

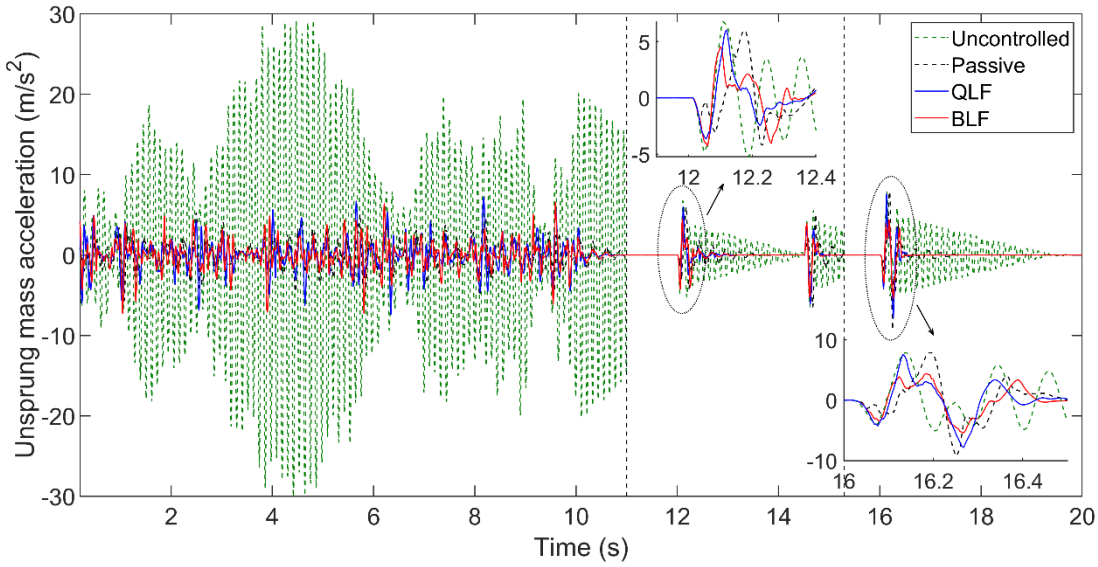

Figure 5.6: Unsprung mass acceleration.

To make a conclusive judgment about the effectiveness of the proposed semi-active control strategy, the frequency domain analysis is also considered. The area of envelope curve given in Figure 5.7 represents the total power of chassis vertical acceleration.

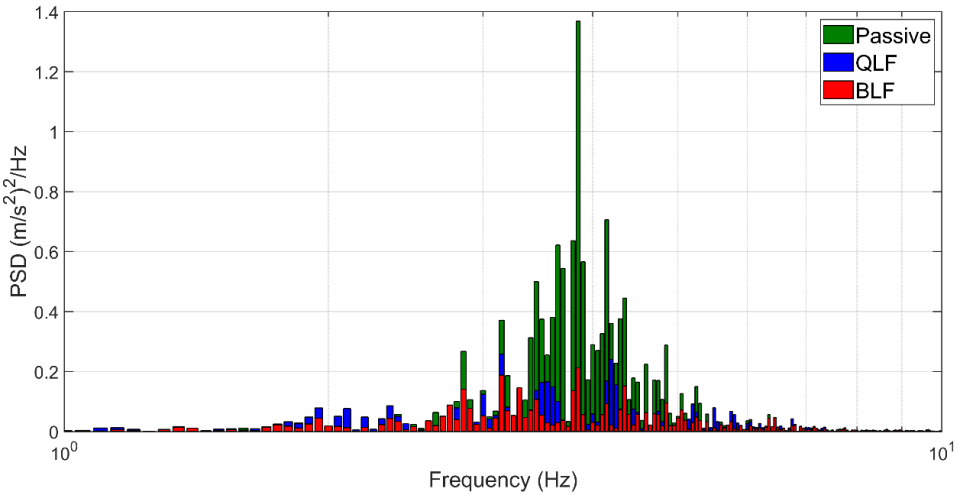

Figure 5.7: Sprung mass vertical acceleration output spectrum.

As summarized in Table 5.2, BLF control achieves the best performance in terms of all the selected comfort and safety criteria except the peak to peak (PTP) value of normalized suspension deflection (NSD).

The suspension deflection should be within the limit of MR damper working space. Passengers feel uncomfortable when the limit of suspension is exceeded. This case also causes mechanical damage to suspension components. Due to the mechanical limitation of the experimental setup, controllers are not tested under the condition of extreme road irregularities, but however, proposed controllers decrease suspension rattle space as given in Table 5.2 and 5.3 when compared to uncontrolled case. Also, it is noticed that uncontrolled suspension exceeds the MR damper working limits. In addition, it can be noticed that the tire keeps contact with the road surface in all cases as indicated by the lower dynamic load coefficient (DLC) values [Múčka, 2017].

Table 5.2: Summary of experimental results for the random road.

	Random Stage			
	Uncontrolled	Passive	QLF	BLF
RMS $\ddot{x}_1$	1.0306	1.1513	0.7353	0.6423
RMS $\ddot{x}_3$	11.771	2.3842	2.4360	2.3206
PTP NSD	1.3799	0.1207	0.2723	0.2010
DLC	0.1941	0.1186	0.0836	0.0757

As given in Table 5.3, the BLF control can suppress unsprung mass acceleration better than QLF control with less usage of suspension working space in both steep ramp and bump stages. In comparison with the BLF control, QLF control reduces chassis acceleration.

Table 5.3: Summary of experimental results in steep ramp and bump stages.

	Steep Ramp Stage				Bump Stage			
	Unc.	Passive	QLF	BLF	Unc.	Passive	QLF	BLF
RMS $\ddot{x}_1$	0.344	0.639	0.225	0.274	0.245	0.491	0.219	0.322
RMS $\ddot{x}_3$	1.922	1.132	0.912	0.882	1.903	1.132	0.997	0.802
PTP NSD	0.468	0.129	0.230	0.188	0.305	0.218	0.211	0.191
DLC	0.042	0.069	0.033	0.036	0.036	0.058	0.035	0.041

5.2. Power Consumption Analysis

There are some methods such as Heaviside step function or inverse polynomial [Choi et al., 2001], [Karkoub et al., 2006]. To synchronize actual force with desired control force calculated by the control algorithm, but this step needs a force sensor and increases the implementation cost. In addition, it may affect the control performance without considering the MR damper dynamics. The proposed backstepping controller directly calculates the required input voltage to the MR damper to meet control objectives without need of measuring the actual force. Figure 5.8 shows measured instantaneous current, it can be noticed that BLF control has an intense characteristic.

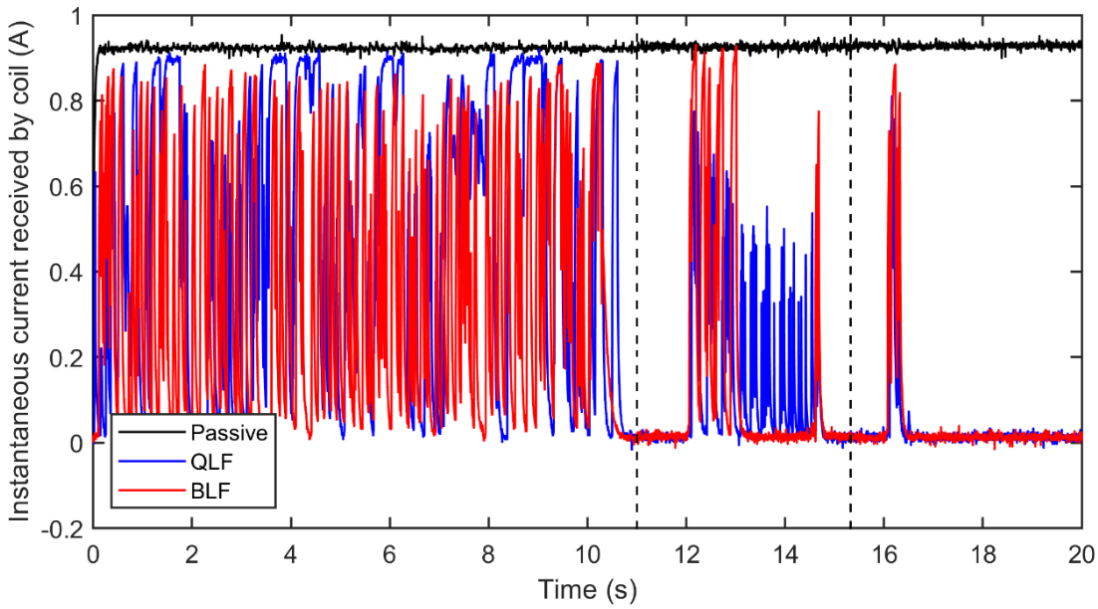

Figure 5.8: Measured instantaneous current.

Due to its intense switching characteristic, the control signal cannot be considered conclusive. Therefore, the total consumed energy was calculated. The net energy consumed is found by integrating the instantaneous power consumption as given in Equation (5.1).

$$W = \int_{t_1}^{t_2} v(t)\, i(t) \tag{5.1}$$

Here t_1 and t_2 are the start and final time of each stage, respectively.

As seen in Figure 5.9, after vertical oscillations are absorbed, controllers cut the voltage to the MR damper. As given in Table 5.4, BLF based control consumes less energy compared to QLF in the random stage.

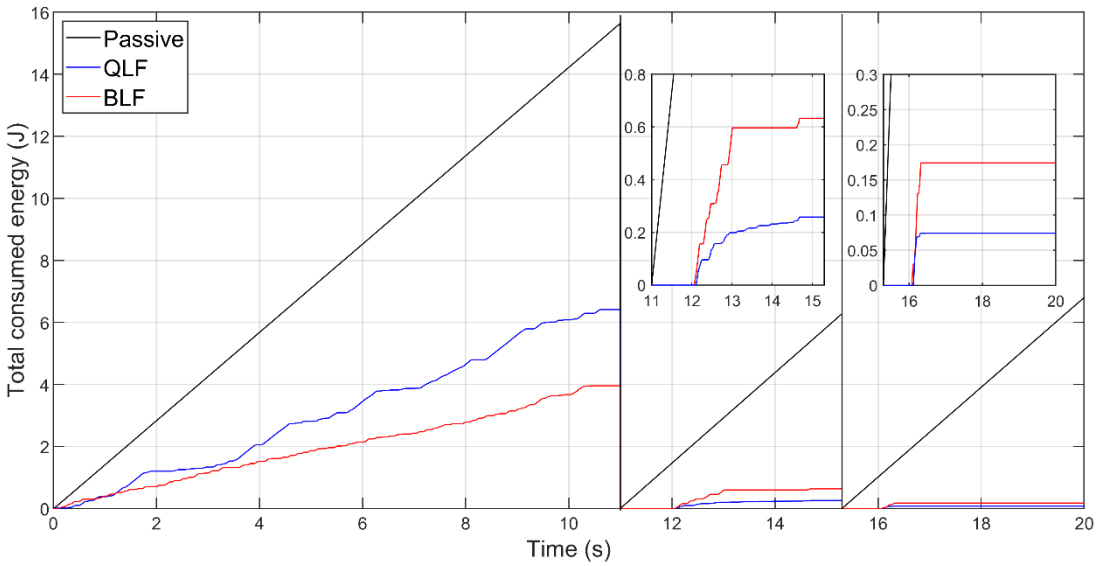

Figure 5.9: Total consumed power.

Table 5.4: Total energy consumption results (Joule).

	Random Stage	Steep Ramp Stage	Bump Stage
Passive	15.640	6.278	6.807
QLF	6.414	0.258	0.074
BLF	3.956	0.633	0.174

5.3. Parameter Adaptation Performance

Existing uncertainties in vehicle parameters influence the performance of suspension systems. Therefore, system parameters should be modelled considering these uncertainties. Also, the control performance can be enhanced when the related parameters are converged to their actual values [Na et al., 2017]. Figure 5.10 shows the parameter adaptation performance of the controllers under the road surface condition defined in subfigure when the 10 % uncertainties in mass properties (both damping and stiffness properties) and 15 % uncertainties in MR damper properties are assumed. Suspension parameters are guaranteed to converge to their true value under a persistent excitation condition when associated adaptation gain adjusted. In addition,

initial parameters of the system and MR damper are needed to be assigned by the designer. These values are given in Table 2.1 and Table 5.1. The convergence behaviour summarized in Figure 5.10. Model parameters of the uncertain MR damper model are obtained by adaptation rules. Almost all estimated MR damper parameters converge to those obtained experimentally in reference [Yıldız et al., 2014].

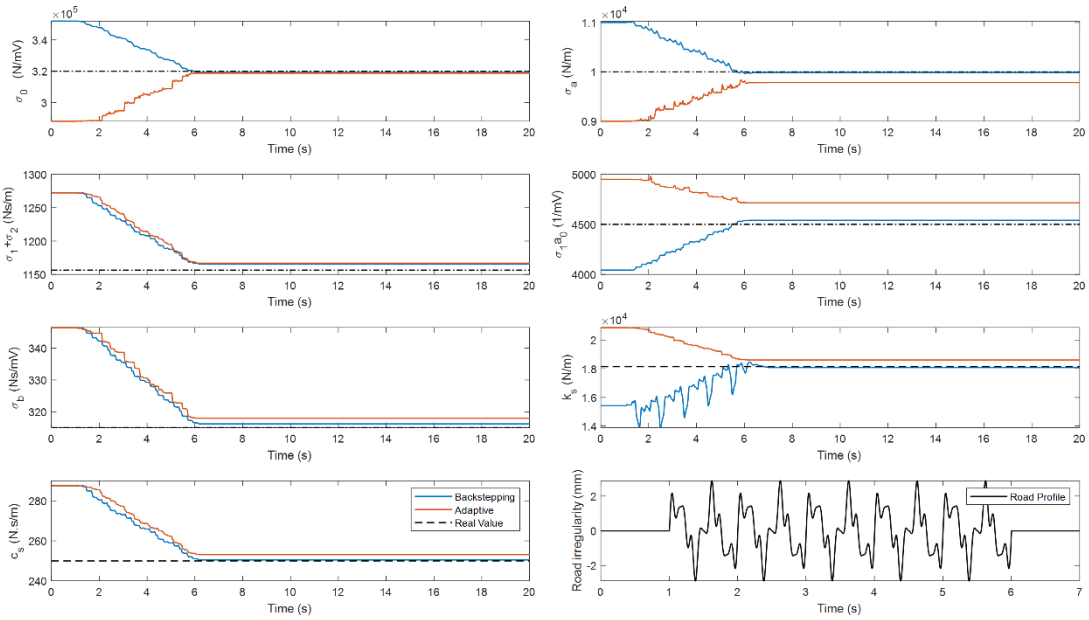

Figure 5.10: Estimation of the damping and stiffness parameters to their real values.

5.4. Control Performance Under Varying Operating Conditions

In this subsection, the quarter-vehicle model is tested on the designed road profiles that are stated in Section 2.3.1, by using different speed levels. The comfort values of the cases are calculated according to ISO 2631-1 and summarized in Figure 5.11. In the simulation study, all system parameters are assumed to be known and the parameters of the controller are given in Table 5.5

Table 5.5: The controller parameter of the semi-active controller.

Parameter	κ_1	κ_2	K_1	ε	m_1	m_2	v_{max}
Value	800	800	100	0.01	17.5	5	2

When the achieved comfort levels given in Figure 5.11 are evaluated by taking into consideration the suspension travel given in Figure 5.12, BLF based controller

provides better comfort in smoother road surfaces (A and B) where there is no restriction on suspension travel. For the poor-quality roads (C and D), BLF based controller sacrifices the performance in terms of comfort in order to restrict suspension deflection.

Also, one can note that ISO road classes A and B (Smooth runway, highway) are acceptable for higher velocities, C (Highway with gravel) for specific limits and D (Rough runway) is suitable for velocities below the speed of 30 km/h when the comfort is considered. In addition, proposed control methods increase the maximum achievable speed under various road and speed conditions.

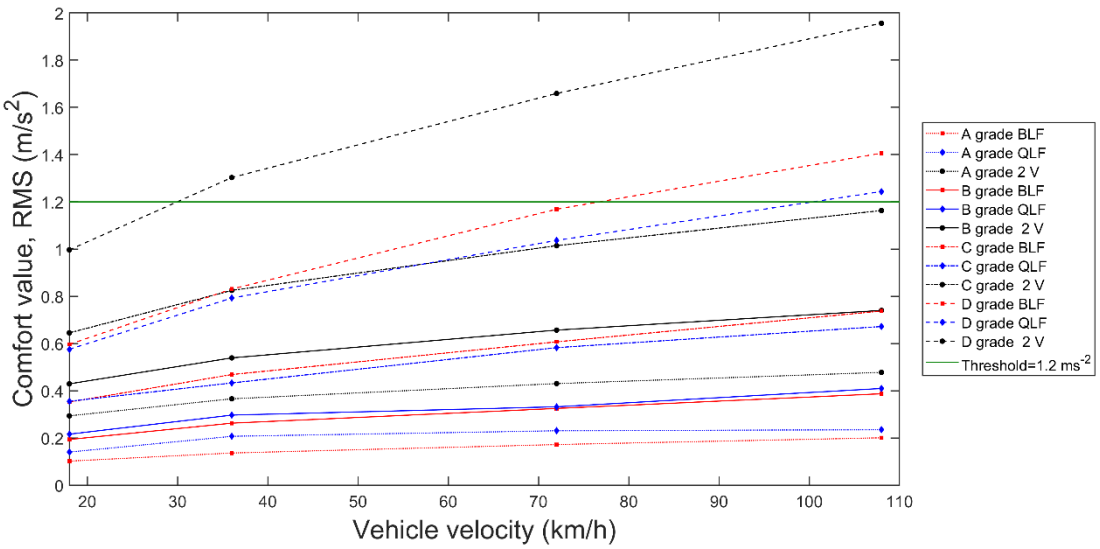

Figure 5.11: RMS value of the frequency-weighted acceleration of the sprung mass.

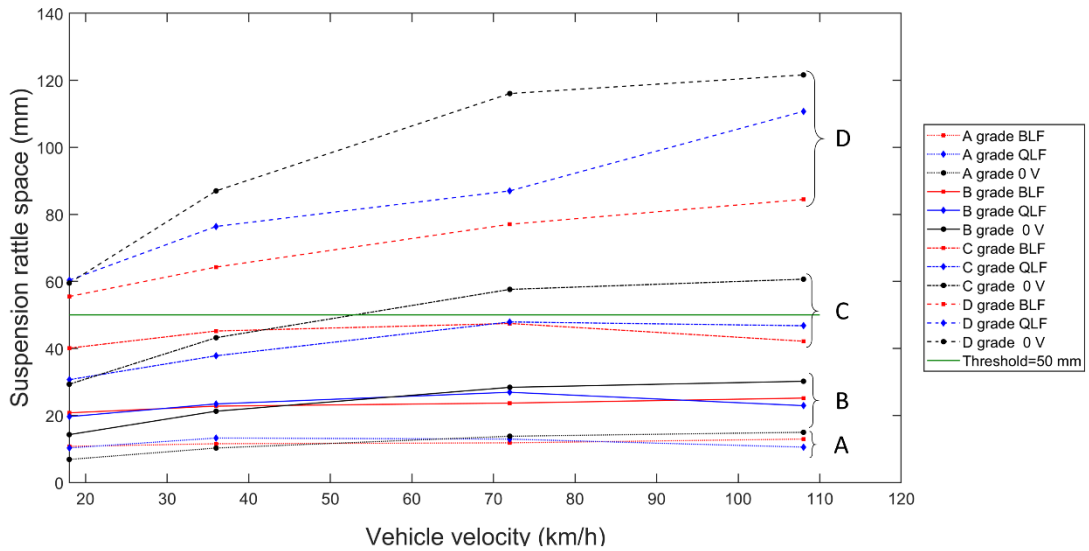

Figure 5.12: Peak to peak values of suspension rattle space at different speed levels.

The DLC values of the controllers are increased with the increment in vehicle speed and road roughness. In other words, the fluctuation magnitude of dynamic loads changes with increasing speed. Also, it can be seen in Figure 5.13 that the designed controller increases the road-holding ability with extending achievable speed value when compared to QLF based controller.

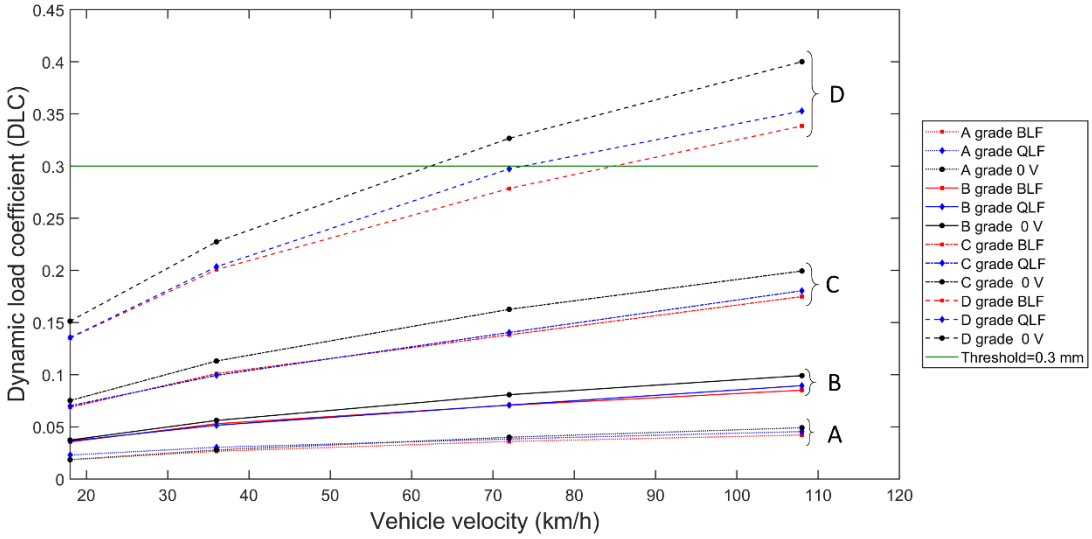

Figure 5.13: Dynamic load coefficient.

As a conclusion, numerical simulations are utilized to demonstrate the feasibility of the proposed control technique under various road and speed conditions. The effectiveness of the proposed controller has been validated through comparisons with uncontrolled, passive and separately designed adaptive control using a QLF case. According to the simulation and experimental results, the proposed control approach improves ride comfort and ride safety without violating suspension rattle space constraint, and despite the uncertainties in parameters. In addition, no force sensor is needed in both control method and, also sensor requirement to measure road profile is eliminated by backstepping control design.

6. VALIDATION OF THE PROPOSED CONTROL APPROACHES USING CO-SIMULATION TOOL

In this section, the effectiveness of the proposed semi-active control strategies will be tested by co-simulation tool. Firstly, the UM -MATLAB co-simulation model and its environment, where all physical phenomena can be integrated, were introduced. After that, the evaluation criteria for assessing the effectiveness of control methods were presented considering practical operation conditions.

A 38 DOF nonlinear full-scale vehicle model, that comprise nonlinear tire models and three rigid body that stand for vehicle car body and bogies were built up in the *input module* of multibody system simulation tool Universal Mechanism as given in Figure 6.1. The secondary suspension for the built monorail vehicle consists of two air springs in the vertical direction and a lateral spring component that represents the lateral stiffness effect of vertical air springs per bogie. For each bogie, the constructed model has virtual MR damper implementation points next to secondary suspension to link the model with MATLAB environment in which designed controller runs. After the model components are created, the working conditions such as vehicle speed, track beam roughness, wind speed are designated by using the *simulation module* of the UM software [Web 3, 2019]. To import the UM model into MATLAB/Simulink, it is required to use S-Functions that provide data exchange between MATLAB/Simulink and UM models. The input signals of the S-Function are assigned as all MR damper force component in the vertical and lateral direction for both front and rear bogie, that calculated at the MATLAB/Simulink side according to control algorithms. The output signals of the S-Function are assigned as the measured variables of the vehicle dynamic states including displacement and acceleration terms.

Such a co-simulation structure provides an opportunity to investigate dynamic system response under various working conditions of the monorail vehicle. The monorail vehicle co-simulation model is shown in Figure 6.2 and the parameters used in the simulation are given in Appendix B.

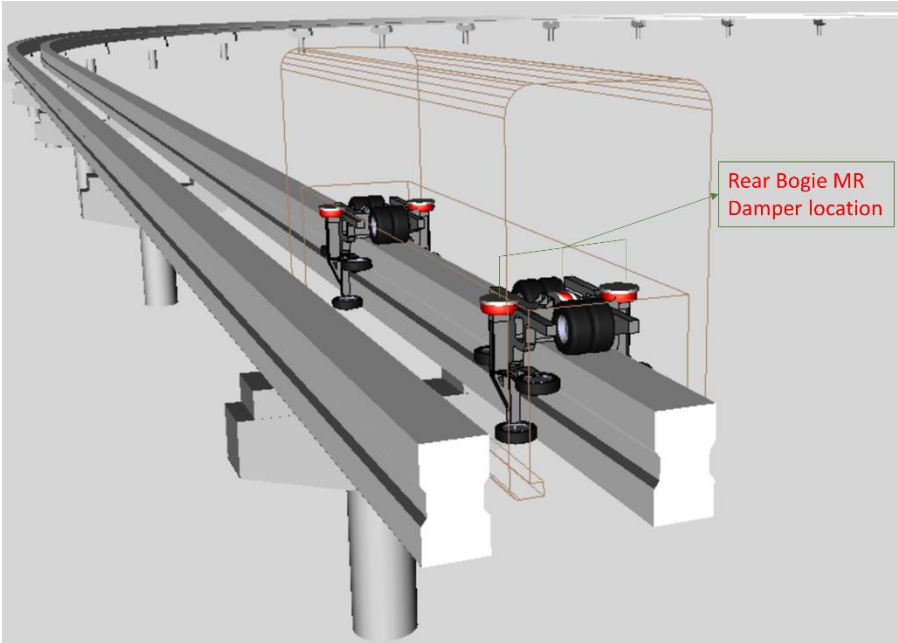

Figure 6.1: Illustration of the straddle type monorail vehicle.

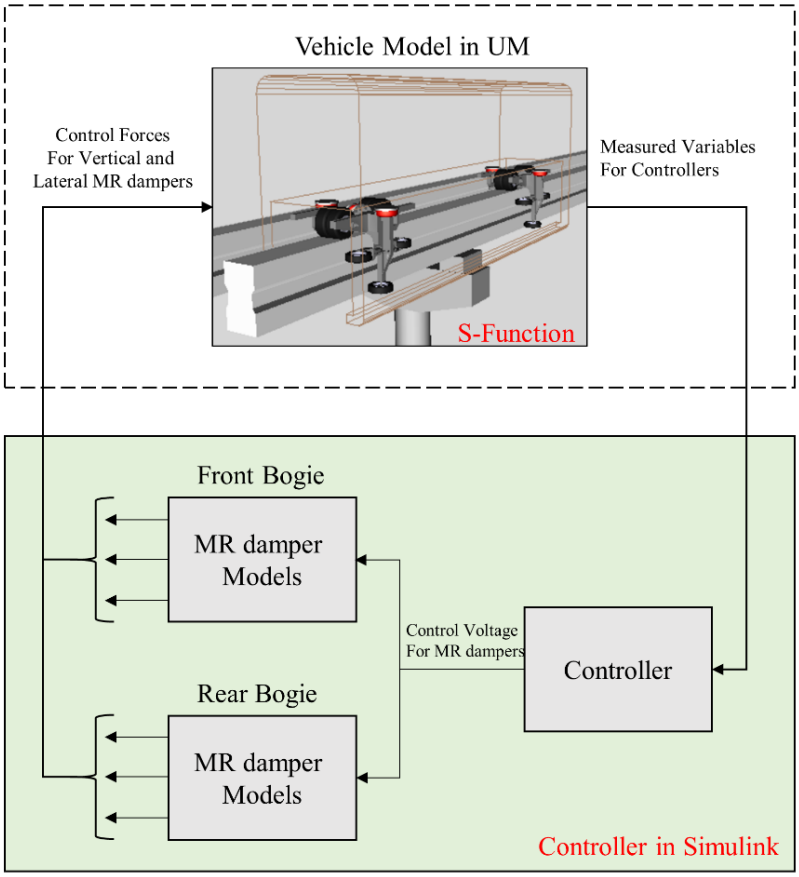

Figure 6.2: Co-simulation system with semi-active control strategy.

6.1. Comparison of Curving Performance

Track surface roughness was created regarding the ISO 8608 standard that explained in Section 2., the road surface profile is given in Figure 6.3. Also, different roughness levels are prescribed for the tires placed at left and right sides of the bogies. The horizontal ($x-y$ plane) road profile used in co-simulation studies is designed such that it has 100 m straight segment, 30 m transition curve and a circular curve of 300 m whose radius changes from 60 m to 300 m. Also, the same order is preserved after the circular curve. The superelevation in the curved section is selected as 5 % and it increased or decreased linearly in the transition stages. The monorail vehicle speed is kept constant at a value of 15 m/s during the designed route and it is assumed that there is no force acting on the monorail vehicle due to crosswind condition. The crosswind forces and moments on the monorail vehicle are investigated in Section 6.2.

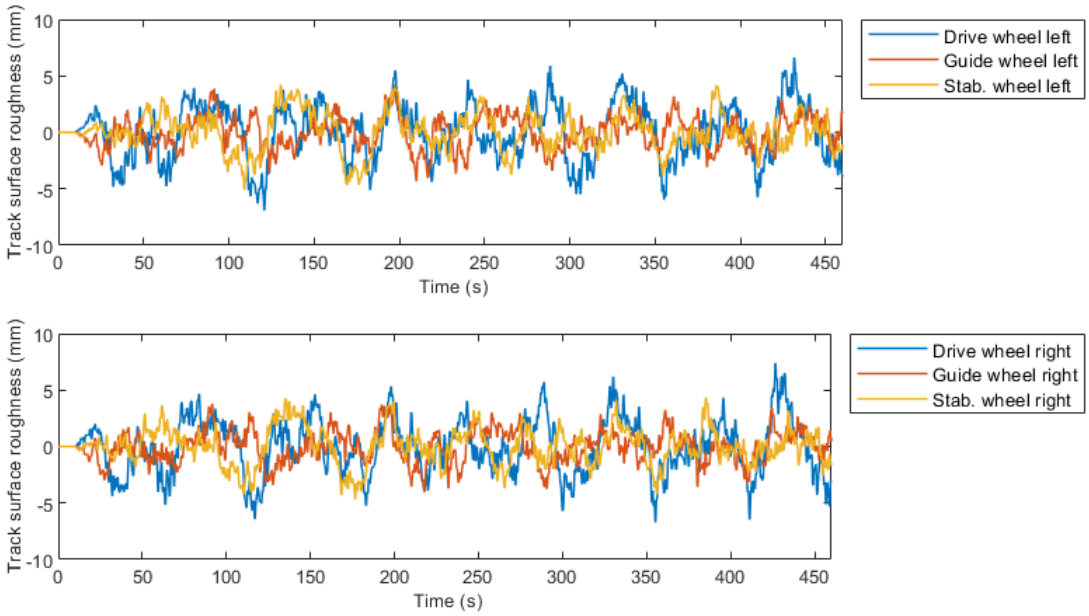

Figure 6.3: Track beam surface roughness.

To demonstrate the effectiveness of the presented methods, the assessment criteria need to be defined. Due to the structural difference of the bogie components of the monorail vehicles, performance evaluation criteria's such as derailment coefficient, wheel load reduction rate or overturning coefficient cannot be conclusive, therefore, bogie lateral displacement and the roll angle between the track plane and the monorail body frame are selected as a performance index during curve negotiation.

In addition, the vertical load change on the running tires, which is closely related to tire wear, can be associated with the roll motion of the bogie structure.

The effect of the radius of curvature of the guideway on front bogie lateral displacement is given in Figure 6.4. As seen in the bar graph, BLF based backstepping controller provides better lateral stability in all radius of curvature ranges when compared to QLF based control and passive cases. In addition, it can be seen that the speed level is so high for the radius of curvature below 200 m. More specifically, the guideway with radius of 150m curve can barely handle the speed of 15 m/s as summarized in Section 2.5.

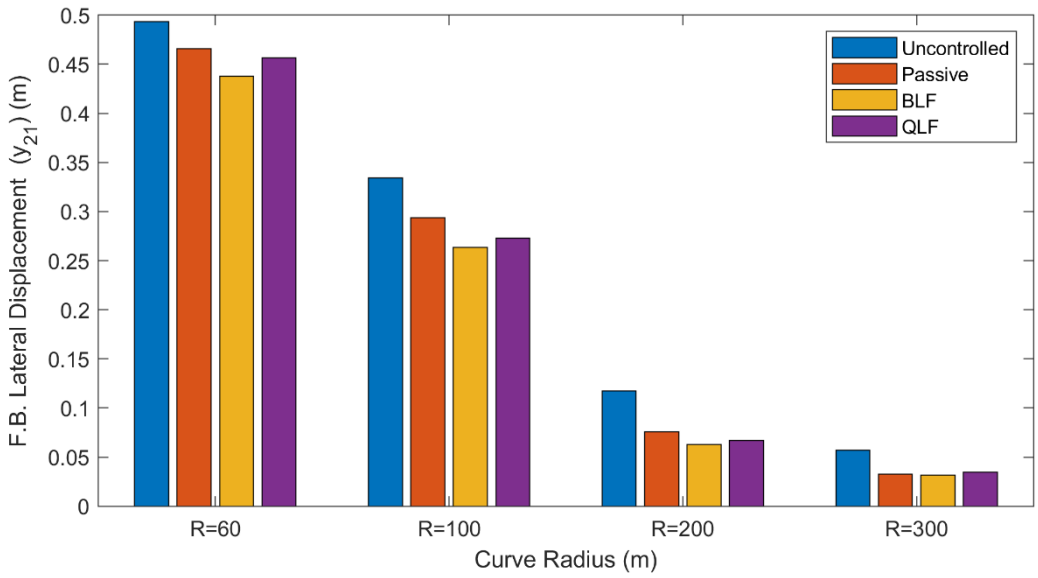

Figure 6.4: Front Bogie COG lateral deflection with various curve radius.

As it can be observed in Table 6.1, BLF based control shows considerable improvement over the uncontrolled case in all curve radius. Also, compared to the passive suspension, the peak to peak value of the lateral displacement is reduced by 17.4 % to 62.8 mm.

Table 6.1: Peak to peak values of the front bogie lateral displacement.

Radius (m)	Uncontrolled	Passive	QLF	BLF
60	0.4932	0.4657	0.4564	0.4378
100	0.3343	0.2939	0.2727	0.2635
200	0.1172	0.0760	0.0667	0.0628
300	0.0571	0.0329	0.0348	0.0314

As given Figure 6.5 and Figure 6.6, proposed controllers act as a hard damper at the transition stage, by this way, lateral displacement of the vehicle body is restricted. Also, the oscillation that occurs during the circular curve stage is eliminated. The same trend is preserved at the transition to the tangent track after the circular curve.

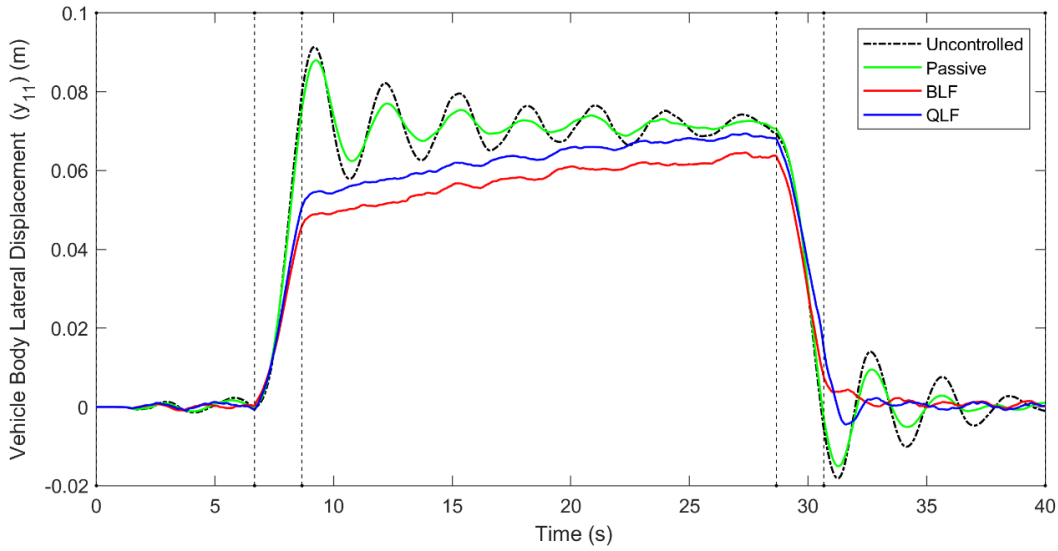

Figure 6.5: Monorail body lateral displacement on the curve radius of 300 m.

When the lateral bogie displacement and the rolling motion of the body given in Figure 6.6 are considered together, it can be concluded that bogie structure that includes semi-active suspension with proper control design not only improve vehicle dynamics but also provide an extended service life to running tires.

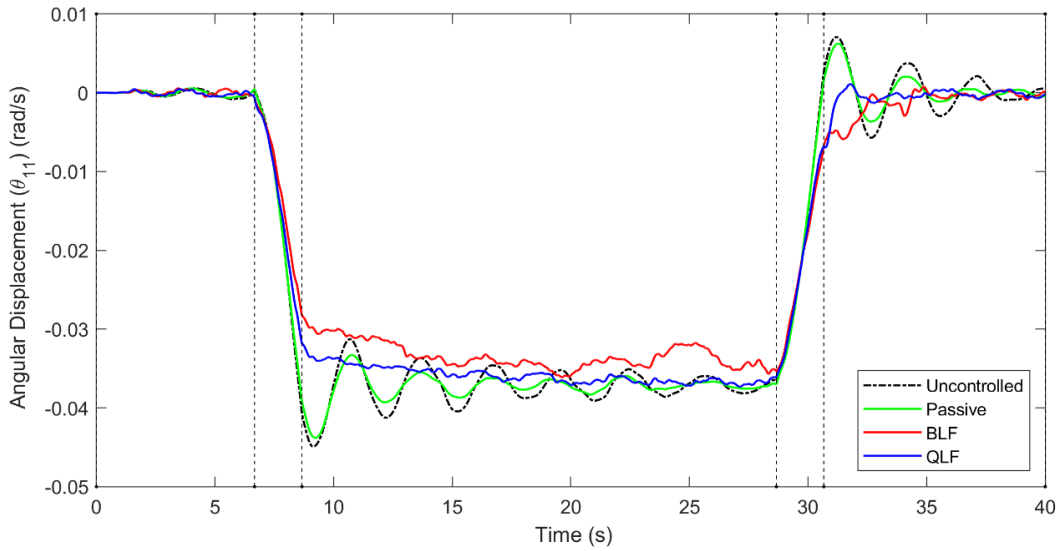

Figure 6.6: Monorail body rolling angle on the curve radius of 300 m.

Figure 6.7 shows the stabilizing tire contact situation which is one of the important indices of the curving performance of the bogie. In case of uncontrolled, the stabilizing tire of the front bogie inner side lost its contact for the most part of the circular stage, but proposed BLF based backstepping controller maintains contact with the guideway side surface.

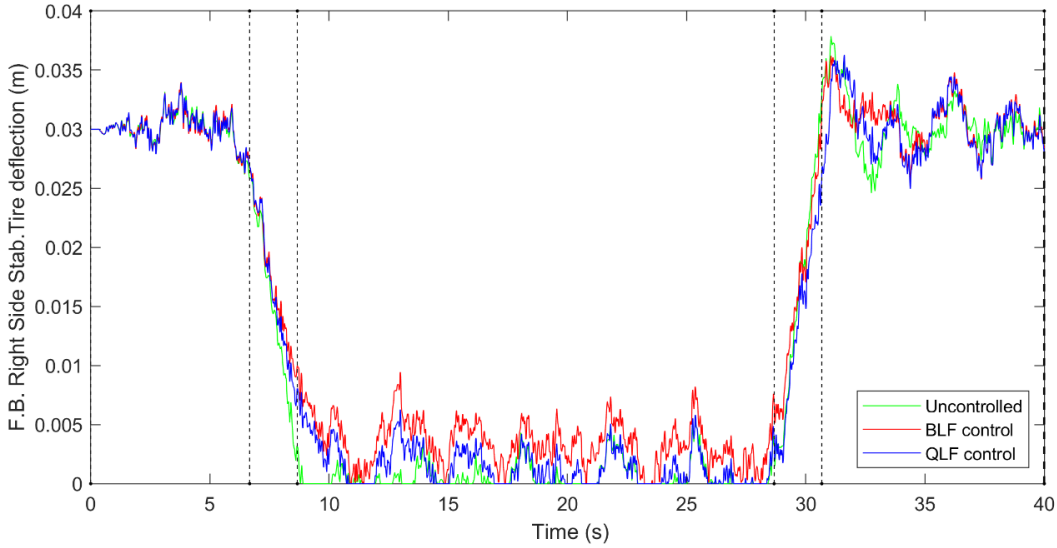

Figure 6.7: Stabilizing tire deflection on the curve radius of 200 m.

An illustration of an exaggerated working condition is shown in Figure 6.8. In case of extreme lateral movement and rolling angle of the bogie, the running tires are getting closer to the edge of the track, but derailment does not occur in running tire.

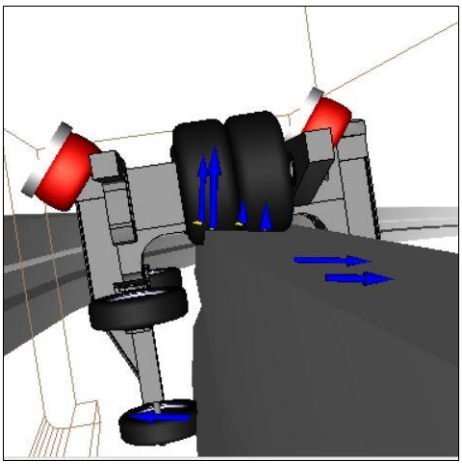

Figure 6.8: Passive system entering the curve segment at excessive speed.

The characteristic of the control signal produced by the controllers are different. As seen in Figure 6.9, BLF based controller working as a switching controller with the changing signal density but QLF based controller produces maximum signal when it is required. Also, it should be noted that sudden changes in supplied voltage lead to rapid rise in produced force that may cause structural damage or noticeable deterioration in driving comfort level. Therefore, adaptive control based on QLF is promising approach because of the changing the MR damper control voltage gradually and smoothly. In addition, it can be seen that when the vehicle enters the circular curve, left side (outside of the curve) MR damper becomes stiffer than the right side, thus, rolling motion of the vehicle body is reduced.

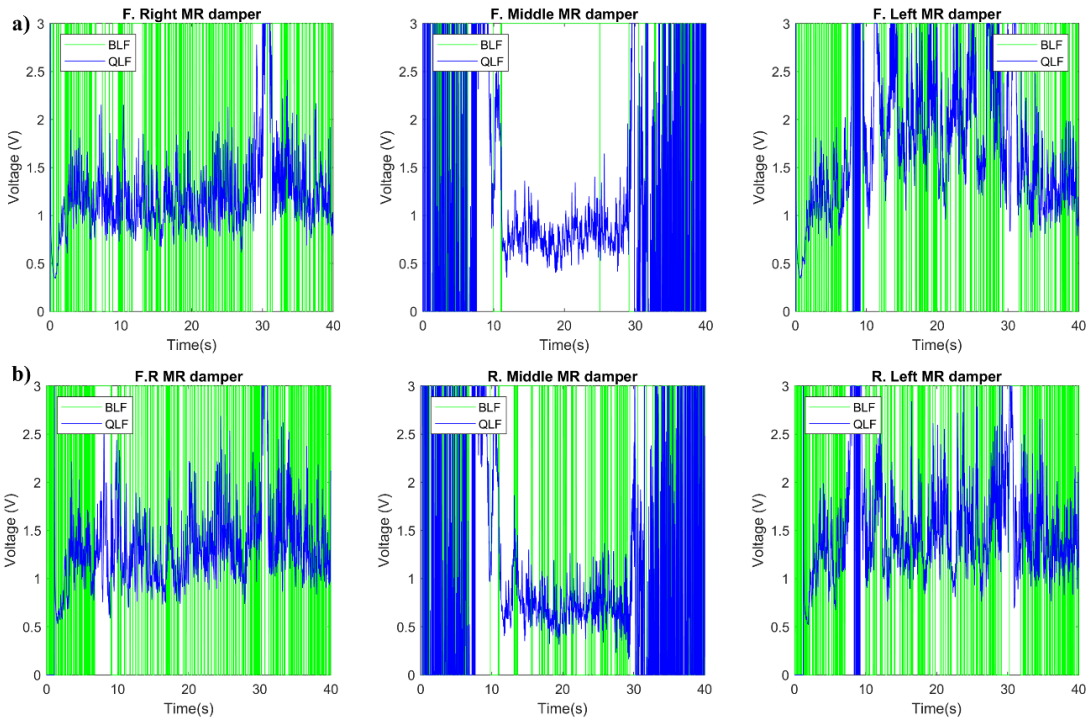

Figure 6.9: Voltage to MR dampers at radius of 100 m: a) Front Bogie, b) Rear Bogie.

Force response of the MR dampers are given Figure 6.10. Due to the lower voltage signal provided to MR dampers in QLF based control, force level becomes lower, but their trends are similar. Also, it can be noted that force requirement can be supplied by a mid-size MR damper.

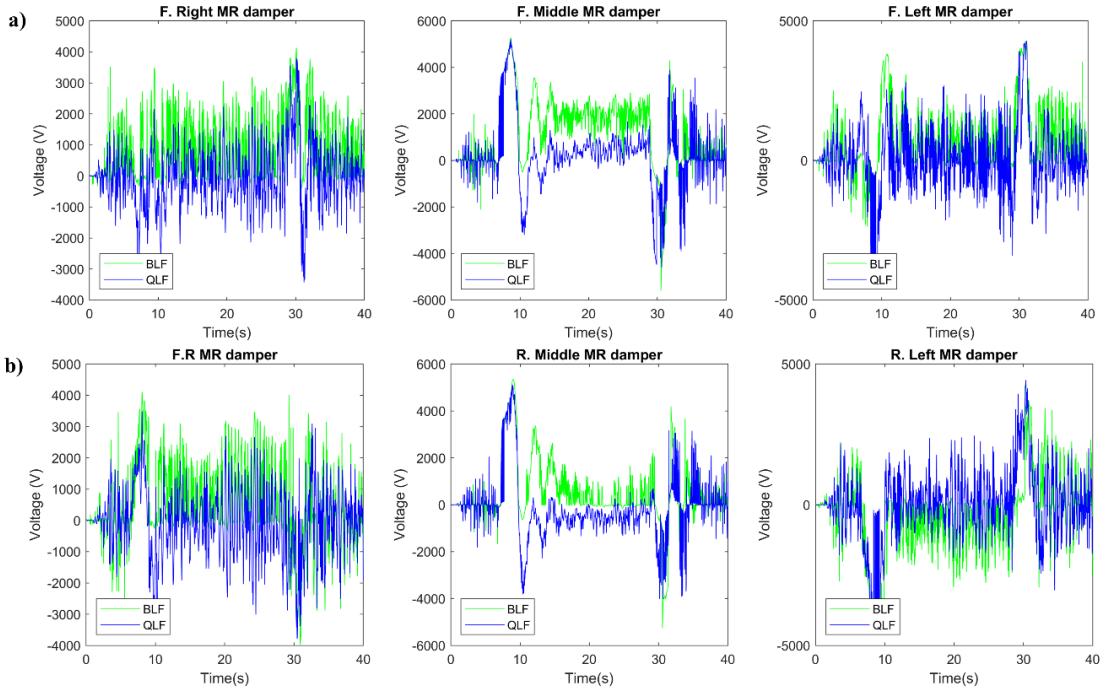

Figure 6.10: MR dampers force at a radius of 100 m: a) Front Bogie, b) Rear Bogie.

6.2. Effect of the Crosswind

Monorail vehicle operates on the elevated guideway structure that placed 7 m to 19 m from the ground and has a width of 850 mm. Also, the distance between left and right-side running tire is about 400 mm, therefore, the lateral wind will seriously affect the monorail vehicles and it should be considered from the point of operation stability and comfort criteria [Yıldız and Sivrioğlu, 2016]. In this subsection, a wind scenario is introduced where the vehicle is loaded with a mean crosswind at a relative wind speed of 0 m/s (stationary), 1 m/s, 3 m/s and 5 m/s during curve negotiation. The system is excited by the road irregularities, external centrifugal force and wind disturbances. The force and moment due to cross-wind effect are defined by equation (6.1) and (6.2). The parameters given in Table 6.2 are taken from the standard which is given by [EN 14067-6, 2010].

$$\begin{aligned}\left(F_{drag}, F_{side}, F_{lift}\right) &= \frac{\rho V_{rel}^{2}}{2} A_{x,y}\left(C_x(\beta), C_y(\beta), C_z(\beta)\right) \\ \left(M_{roll}, M_{pitch}, M_{yaw}\right) &= \frac{\rho V_{rel}^{2}}{2} L A_{x,y}\left(C_{\alpha x}(\beta), C_{\alpha y}(\beta), C_{\alpha z}(\beta)\right)\end{aligned} \tag{6.1}$$

Here A_x and A_y are the frontal and side reference area, ρ is the air density of 1.2 kg/m3. The term, V_{rel} , is the air velocity relative to the vehicle. β is the angle that the crosswind makes with the direction of travel as shown in Figure 6.11. C_x, C_y, C_z are drag force, side force and lift force coefficients along x, y and z axis respectively. $C_{\alpha x}$, $C_{\alpha y}$,$C_{\alpha z}$ are roll moment, pitch moment and yaw moment coefficients about x, y and z axis, respectively.

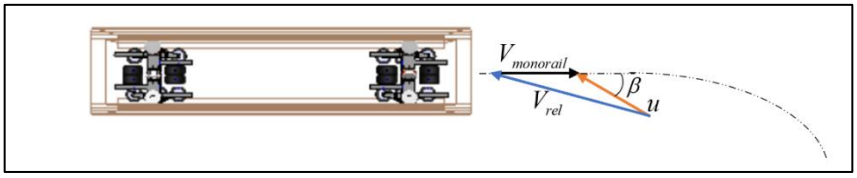

Figure 6.11: Wind load acting on vehicle during the movement.

Table 6.2: The values of aerodynamic coefficients.

Yaw angle (β)	Force coefficients			Moment coefficients		
	C_x	C_y	C_z	$C_{\alpha x}$	$C_{\alpha y}$	$C_{\alpha z}$
40°	0.200	-6.368	6.806	3.773	3.443	4.840

It can be seen in Figure 6.12 that the lateral motion of the monorail vehicle body equipped with a conventional suspension structure significantly influenced by increased wind speed. However, semi-actively controlled suspension systems provide more robustness to the changing crosswind speed conditions.

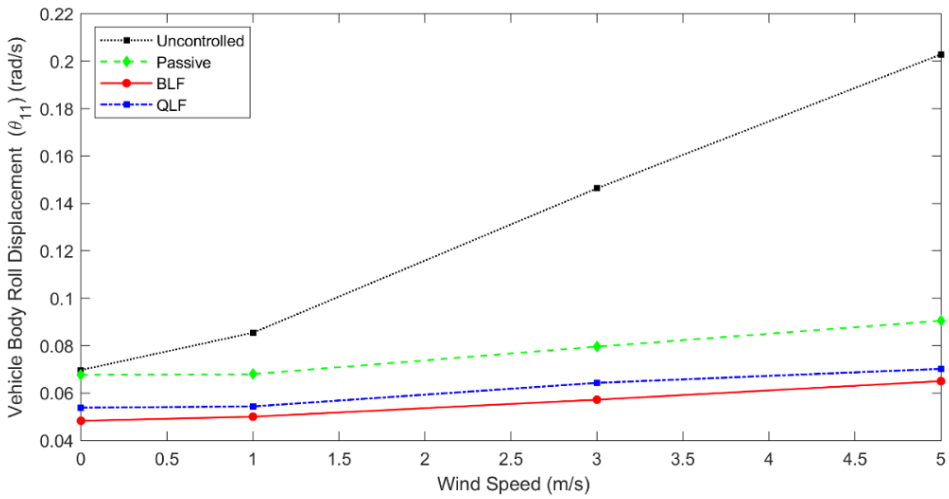

Figure 6.12: Peak-to-peak values of body roll angle at different speed levels.

The effects of crosswinds at various speed levels can be seen in Figure 6.13. In the simulation scenario, the radius of curvature of the circular segment was held constant at 200 m. It can be noted that the crosswind speed above 3 m/s greatly influence the bogie lateral dynamics and it should be taken into consideration when the planning the vehicle operation. The peak to peak lateral displacement even in BLF control is increased by 90.29 percent to 119.5 mm at 5 m/s wind speed.

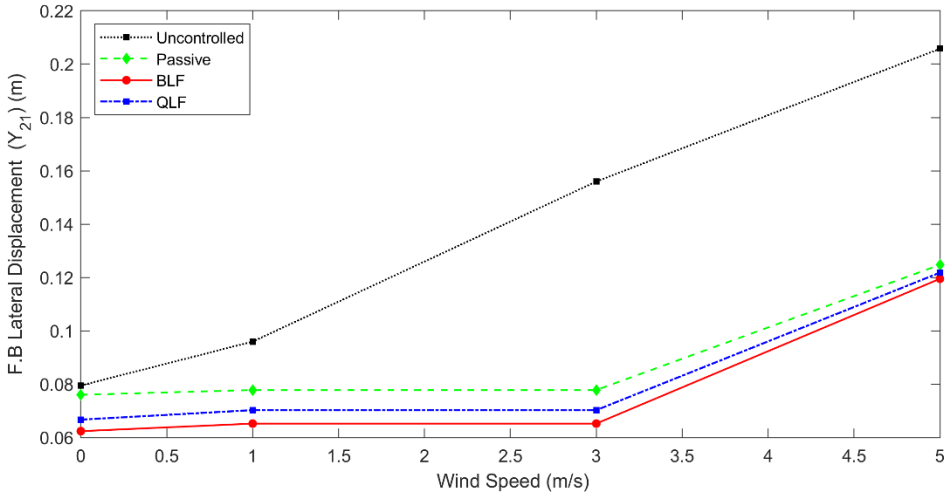

Figure 6.13: Peak-to-peak values of front bogie lateral displacement at different speed levels.

As it can be seen in Figure 6.14, the peak value of the lateral slip of the running tire at front bogie left side is decreased in cased of BLF. This improvement provides better curving stability while the monorail vehicle negotiating the curve.

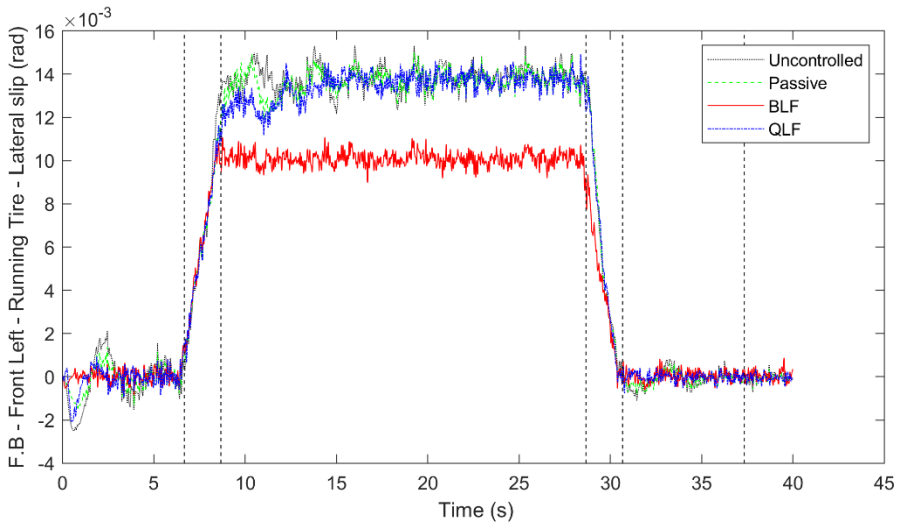

Figure 6.14: Lateral slip of the running tire at wind speed of 3 m/s.

7. CONCLUSIONS AND RECOMMENDATION

In this dissertation, the curving performance of the monorail vehicles is enhanced by using semi-active magnetorheological (MR) dampers because of the fact that negotiating small radius curves provides more flexibility to monorail vehicle in urban areas. In order to address this problem thoroughly, a monorail vehicle model including the tire model and road surface model is necessary. To enable the monorail vehicles to negotiate sharp curves, it is required to optimize system model parameters and suspension parameters. This optimization for the conventional type passive suspension may result in passenger discomfort when the vehicle travelling on straight route or large radius curves. It is observed that the adding controllable dampers next to conventional air suspension without costly replacements or adjustments have a prominent effect on the compensation of vehicle dynamics, especially in the lateral direction. Also, the allowable maximum travelling speed value of the monorail vehicles is specified by the international railway standard in terms of curve radius without regard to vehicle suspension structure. At this point, an alternative restriction should be made on a monorail operating speed limits by considering unique bogie structure.

Vehicle travelling speed has been extended with a further possible way of improving both uncompensated lateral acceleration and stabilizing tire contact condition. For the considered vehicle, it is shown that the vehicle can reach to speed of 10.96 m/s on 50 m curve radius which is higher than the % 17 specified in the standards. This improvement reduces the average travel time between station. In addition, the pre-pressure value of the guiding and stabilizing tire should be below 13 kN to ensure travelling comfort criteria and avoid excessive tire wear.

It is observed that both vertical and lateral comfort indices are majorly influenced by the transition track segment. Also, driving stability can be quantified by the lateral and roll motion of the bogie and vehicle body, these criteria reach to high level in the transition stage. It is observed that proposed BLF based backstepping control reduce the RMS values of the vehicle vertical and lateral acceleration by 5.8 % and 66.1 % when compared to conventional suspension.

Adaptive backstepping control approach can restrict the suspension working space to prevent structural damage. When the constructed quarter-train model is

considered, it is shown that BLF based controller provides better comfort in smoother road surfaces where there is no restriction on suspension travel. For the poor-quality roads, BLF based controller sacrifices the performance in terms of comfort in order to restrict suspension deflection. Also, the proposed control approaches effectively reduce the vertical oscillation of the quarter-train model in a range of frequency near the resonant frequency of the sprung mass which corresponding to the monorail vehicle body.

Utilized multibody simulation software results show that the proposed suspension control approaches not only improve the curving performance of the monorails but also provide extended tire life when the reduction in lateral displacement of the bogies and the running tire slip angle is taken into consideration. It can be noted that the wind speed exceeding the 3 m/s have a significant influence on the lateral displacement responses of the moving monorail vehicle.

The results obtained by the MR damper parameter identification setup show that the identified MR damper parameter with the selected mathematical model can capture the dynamic force response of the MR damper. Thus, the performance of the controllers that will be implemented can be increased. Also, it should be noted that applying constant electrical input to the MR damper not only cause performance degradation but also increase energy consumption. In addition, supplying high control voltage to low capacity MR damper leads to chattering behavior which adversely affects the passenger comfort.

First future development of this dissertation is to investigate the influence of guideway flexibility on the curving performance of a monorail vehicle. Also, the effect of the suspension control strategies on guideway vertical and lateral displacement can be investigated by constructing a coupled model. The utilized multibody simulation software results show that the constituted mathematical equations including centrifugal effects and tire model are sufficient for the curving simulation of a monorail vehicle, but further improvement is needed to investigate the acceleration and deceleration of the vehicle. In order to do so, longitudinal tire dynamics should be taken into account. The final step in this future study can be the practical implementation of the developed control strategies to real scale monorail vehicle.

REFERENCES

Atray V. S., Roschke P. N., (2004), "Neuro-fuzzy control of railcar vibrations using semi-active dampers", Computer-Aided Civil and Infrastructure Engineering, 19 (2), 81-92.

Brenna M., Foiadelli F., Zaninelli D., (2018), "Electrical Railway Transportation Systems", John Wiley & Sons.

Cai C., He Q., Zhu S., Zhai W., Wang M., (2019), "Dynamic interaction of suspension-type monorail vehicle and bridge: numerical simulation and experiment", Mechanical Systems and Signal Processing, 118, 388-407.

CEN-EN, (2010), Railway applications–aerodynamics–part 6: requirements and test procedures for cross wind assessment, CEN-EN 14067-6, European Committee for Standardization.

Choi S. B., Lee S. K, Park Y. P., (2001), "A Hysteresis model for the field dependent damping force of a aagnetorheological damper", Journal of Sound and Vibration, 245 (2), 375-383.

Dong X. M., Yu M., Liao C. R., Chen W. M., (2010), "Comparative research on semi-active control strategies for magneto-rheological suspension", Nonlinear Dynamics, 59 (3), 433-453.

Du H., Lam J., Cheung K. C., Li W., Zhang N., (2013), "Direct voltage control of magnetorheological damper for vehicle suspensions", Smart Materials and Structures, 22 (10), 105016.

Du H., Sze K. Y., Lam J., (2005), "Semi-active control of vehicle suspension with magneto-rheological dampers", Journal of Sound and Vibration, 283 (3-5), 981–996.

Du Z., Wen X., Zhao D., Xu Z., Chen L., (2017), "Numerical analysis of partial abrasion of the straddle-type monorail vehicle running tyre" Transactions of FAMENA, 41 (1), 99-112.

Du Z., Zhou J., Yang Z., Bo J., (2018), "The research on operational reliability evaluation of straddle-type monorail vehicle", Systems Science & Control Engineering, 6 (1), 537-546.

Fiala E., (1954), "Lateral forces on rolling pneumatic tires" In Zeitschrift V.D.I., 96 (29), 114.

Fukao T., Yamawaki A., Adachi N., (2002), "Adaptive control of partially known systems and application to active suspensions", Asian Journal of Control, 4 (2), 199-205.

Gamota D. R., Filisko F. E., (1991), “Dynamic mechanical studies of electrorheological materials: moderate frequencies”, Journal of Rheology, 35 (3), 399-425.

Goda K., Nishigaito T., Hiraishi M., Iwasaki K., (2000), “A curving simulation for a monorail car”, In Proceedings of the 2000 ASME/IEEE Joint Railroad Conference, 171-177, Newark, NJ, USA, 6 April.

Goda K., Nishigaito T., Hiraishi M., Iwasaki K., (2002), “Improving curving performance for articulated-type small monorail car”, Transactions of the Japan Society of Mechanical Engineers C, 68 (672), 2410-2417.

Gu D. W., Petkov P. H., Konstantinov M. M., (2014), “Robust control design with MATLAB®”, Springer Science & Business Media.

Ha S. H., Choi S. B., Lee G. S., Yoo W. H. (2013), “Control performance evaluation of railway vehicle MR suspension using fuzzy sky-ground hook control algorithm” Journal of Physics: Conference Series, 412 (1), 012042.

Huang Y., Na J., Wu X., Liu X., Guo Y., (2015), “Adaptive control of nonlinear uncertain active suspension systems with prescribed performance”, ISA Transactions, 54, 145-155.

ISO, (1995), Mechanical vibration–road surface profiles–reporting of measured data, ISO 8608, International Standardization Organization.

Iwnicki S., (2006), “Handbook of railway vehicle dynamics”, 1st Edition, CRC press.

Ji Y., Ren L., (2018), “Anti-overturning capacity and critical roll angle of straddling monorail vehicle”, Proceedings of the Institution of Mechanical Engineers, Part C: Journal of Mechanical Engineering Science, 232 (23), 4420-4429.

Jiang Y., Wu P., Zeng J., Gao H., (2018), “Comparison of the curve negotiation properties of two different articulated monorail vehicles”, Proceedings of the Institution of Mechanical Engineers, Part F: Journal of Rail and Rapid Transit, 223 (8), 831-843.

Jiang Y., Wu P., Zeng J., Wei L., Lv K., Zhang Y., Dai X., (2019), “Detection and alleviation of the abnormal vibration of the monorail based on experiment and simulation”, Journal of Low Frequency Noise, Vibration and Active Control, 38 (2), 282-295.

Jimenez R., Alvarez-Icaza L., (2005), “LuGre friction model for a magnetorheological damper”, Structural Control and Health Monitoring, 12 (1), 91–116.

Karkoub M. A., Zribi M., (2006), “Active/semi-active suspension control using magnetorheological actuators”, International Journal of Systems Science, 37 (1), 35–44.

Koch G., Kloiber T., (2013), “Driving state adaptive control of an active vehicle suspension system”, IEEE Transactions on Control Systems Technology, 22 (1), 44-57.

Kwok N. M., Ha Q. P., Nguyen M. T., Li J., Samali B., (2006), “A novel hysteretic model for magneto-rheological fluid damper and parameter identification using particle swarm optimization”, Sensor and Actuators A: Physical, 132 (2), 441-451.

Lee C. H., Kim C. W., Kawatani M., Nishimura N., Kamizono T., (2005), “Dynamic response analysis of monorail bridges under moving trains and riding comfort of trains”, Engineering Structures, 27 (14), 1999-2013.

Liao W. H., Wang D. H., (2003), “Semi-active vibration control of train suspension systems via magnetorheological dampers”, Journal of intelligent material systems and structures, 14 (3), 161-172.

Lin J. S., Kanellakopoulos I., (1997), “Nonlinear design of active suspensions”, IEEE Control Systems Magazine, 17 (3), 45-59.

Maciel G. P., Barbosa R. S., (2016), “Monorail vehicle model to study influence of tyre modelling on overall dynamics”, International Journal of Heavy Vehicle Systems, 23 (4), 317–332.

Múčka P., (2017), “Simulated road profiles according to ISO 8608 in vibration analysis”, Journal of Testing and Evaluation, 46 (1), 405-418.

Na J., Huang Y., Wu X., Gao G., Herrmann G., Jiang, J. Z., (2017), “Active adaptive estimation and control for vehicle suspensions with prescribed performance”, IEEE Transactions on Control Systems Technology, 26 (6), 2063-2077.

Orvnäs A., Stichel S., Persson R., (2011), “Active lateral secondary suspension with H∞ control to improve ride comfort: simulations on a full-scale model”, Vehicle System Dynamics, 49 (9), 1409-1422.

Pacejka H. B., (2005), “Tire and vehicle dynamics”, 3rd Edition, Elsevier.

Pombo J., Ambrósio J. A., (2003), “General spatial curve joint for rail guided vehicles: kinematics and dynamics”, Multibody System Dynamics, 9 (3), 237-264.

Şahin I., Engin T., Çeşmeci Ş., (2010), “Comparison of some existing parametric models for magnetorheological fluid dampers”, Smart Materials and Structures, 19 (3), 035012.

Sakai C., Ohmori H., Sano A., (2003), “Modeling of MR damper with hysteresis for adaptive vibration control”, Proceedings of the 42nd IEEE Conference on Decision and Control, 3840-3845, Hawaii, USA, 9-12 December.

Sammier D., Sename O., Dugard L., (2003), “Skyhook and H8 control of semi-active suspensions: some practical aspects”, Vehicle System Dynamics, 39 (4), 279-308.

Schmeitz A., (2004), “A Semi-Empirical Three-Dimensional Model of the Pneumatic Tyre Rolling over Arbitrarily Uneven Road Surfaces”, Doctoral Thesis, Delft University of Technology.

Shaltout R., Ulianov C., Baeza L., (2015), “Development of a simulation tool for the dynamic analysis of railway vehicle-track interaction”, Transport Problems, 10, 47-58.

Shin Y. J., You W. H., Hur H. M., Park J. H., (2014), “H∞ control of railway vehicle suspension with MR damper using scaled roller rig”, Smart Materials and Structures, 23 (9), 095023.

Spencer B. F., Dyke S. J., Sain M. K., Carlson J. D., (1997), “Phenomenological model of a magnetorheological damper”, ASCE J. Eng. Mech, 8, 123-230.

Sun S., Deng H., Li W., Du H., Ni Y. Q., Zhang J., Yang J., (2013), “Improving the critical speeds of high-speed trains using magnetorheological technology”, Smart Materials and Structures, 22 (11), 115012.

Sun W., Gao H., Kaynak O., (2013), “Adaptive Backstepping Control for Active Suspension Systems with Hard Constraints”, IEEE/ASME Transactions on Mechatronics, 18 (3), 1072–1079.

Sun W., Pan H., Zhang Y., Gao H., (2014), “Multi-objective control for uncertain nonlinear active suspension systems”, Mechatronics, 24 (4), 318–327.

Tee K. P., Ge S. S., Tay E. H., (2009), “Barrier Lyapunov functions for the control of output-constrained nonlinear systems”, Automatica, 45 (4), 918–927.

Terasawa T., Sakai C., Ohmori H., Sano A., (2004), “Adaptive Identification of MR damper for vibration control”, Proceedings of the 43rd IEEE Conference on Decision and Control, 2297-2303, Atlantis, Bahamas, December 14-17.

Wang H., Zhu E., (2018), “Dynamic response analysis of monorail steel-concrete composite beam-train interaction system considering slip effect”, Engineering Structures, 160, 257-269.

Wang H., Zhu E., Chen Z., (2017), “Dynamic response analysis of the straddle-type monorail bridge–vehicle coupling system”, Urban Rail Transit, 3 (3), 172-181.

Web 1, (2019), https://www.mlit.go.jp/english/2006/h_railway_bureau/Laws_concerning/14.pdf, (Date Accessed: 23/04/2019).

Web 2, (2019), http://mohua.gov.in/upload/uploadfiles/files/6.Hitachi.pdf, (Date Accessed: 23/04/2019).

Web 3, (2012), http://www.universalmechanism.com/, 2019., (Date Accessed: 14/06/2012).

Wei X., Zhu M., Jia L., (2016), “A semi-active control suspension system for railway vehicles with magnetorheological fluid dampers”, Vehicle System Dynamics, 54 (7), 982-1003.

Wu Q., Spiryagin M., Cole C., Chang C., Guo G., Sakalo A., Chollet H., (2018), “International benchmarking of longitudinal train dynamics simulators: results”, Vehicle System Dynamics, 56 (3), 343-365.

Xia P. Q., (2003), “An inverse model of MR damper using optimal neural network and system identification”, Journal of Sound and Vibration, 266 (5), 1009-1023.

Yıldız A. S., (2013), “Semi Active Adaptive Control of Quarter Car Model”, Master’s Thesis, Gebze Technical University.

Yıldız A. S., Sivrioğlu S., (2019), “Improving curving performance of a straddle type monorail vehicle by using semi-active devices”, International Journal of Heavy Vehicle Systems, In Press.

Yıldız A. S., Sivrioğlu S., Zergeroğlu E., Çetin Ş., (2014), “Nonlinear adaptive control of semi-active MR damper suspension with uncertainties in model parameters”, Nonlinear Dynamics, 79 (4), 2753–2766.

Zhao S., Liu X., Du, Z., Li Y., (2014), “Riding stability of urban straddle-type monorail vehicles under lateral wind”, Science & Technology Review, 32 (22), 42-46.

Zhou J., Du Z., Yang Z., Xu Z., (2019), “Dynamic parameters optimization of straddle-type monorail vehicles based multi objective collaborative optimization algorithm”, Vehicle System Dynamics, 1-20.

Zong L. H., Gong X. L., Xuan S. H., Guo, C. Y., (2013), “Semi-active H∞ control of high-speed railway vehicle suspension with magnetorheological dampers”, Vehicle System Dynamics, 51 (5), 600-626.

BIOGRAPHY

Ali Suat Yıldız was born in Arsin/Trabzon, in 1987. He received the bachelor's degree in mechanical engineering from the Celal Bayar University in 2008. He received the M.Sc. degree in mechanical engineering from the Gebze Institute of Technology in 2013. He started doctoral studies at Gebze Technical University Graduate School of Natural and Applied Science Department of Mechanical Engineering. He is currently a research assistant and PhD student at Gebze Technical University. His research interests include modelling and control of the dynamic systems, nonlinear control applications, robust control designs, magnetorheological dampers and the modelling of the superconductive levitation systems.

APPENDICES

Appendix A: Articles Published During the Thesis Study

A1- A. S. Yildiz and S. Sivrioglu (2019) ‘Constrained Adaptive Backstepping Control of a Semi-active Suspension Considering Suspension Travel Limits’, Asian Journal of Control, In Revision.

A2- A. S. Yildiz and S. Sivrioglu (2020) ‘Improving Curving Performance of a Straddle Type Monorail Vehicle by Using Semi-Active Devices’, Int. J. Heavy Vehicle Systems, DOI: 10.1504/IJHVS.2020.10021579.

A3- Saltık, S., Yıldız, A. S., Sivrioglu, S., Dülger, Z. (2019) ‘Experimental comparison of control methods for armoured personnel carriers with semi-active magneto-rheological suspension, Int. J. Heavy Vehicle Systems, DOI: 10.1504/IJHVS.2019.10016575

A4- Yıldız, A. S., Sivrioğlu, S., Zergeroğlu, E., Çetin, Ş. (2015). Nonlinear adaptive control of semi-active MR damper suspension with uncertainties in model parameters. Nonlinear Dynamics, 79(4), 2753-2766. DOI:10.1007/s11071-014-1844-9

A5- A. S. Yildiz, S. Sivrioglu, E. Zergeroglu, S.Cetin, “ Adaptive Control of Semiactive Quarter Car Model with MR Damper” Proc. of Asian Control Conf., Post-A.48, Istanbul, Turkey, 2013. DOI: 10.1109/ASCC.2013.6606324

A6- A. S. Yildiz,S. Sivrioglu “Semi-active Vibration Control of Lateral and Rolling Motions for a Straddle Type Monorail Vehicle, 14th IFAC Symposium on Control in Transportation Systems, 18-20 May 2016,Istanbul Technical University, İstanbul, Turkey. DOI: 10.1016/j.ifacol.2016.07.047

A7- A. S. Yildiz, S. Sivrioglu “Characterization of MR Damper for Use in Semi Active Suspension”, Automotive and Vehicle Technologies Conference, AVTECH’14, 16-18 Oct 2014, Yildiz Technical University, İstanbul, Turkey.

A8- A. S. Yildiz, S. Sivrioglu “Design and Control of a Semi- active Regenerative Suspension System”, 9th International Automotive Technologies Congress, OTEKON2018, 7-8 May 2018, Bursa, Turkey.

A9- A. S. Yildiz, S. Sivrioğlu "Yarı Aktif Sönümleyiciler ile Monoray Taşıtların Viraj Dönme Dinamiklerinin İyileştirilmesi" Otomatik Kontrol Ulusal Toplantısı TOK-2016, Eskişehir-Turkiye, 29 Eylül-1 Ekim 2016.

Appendix B: Monorail vehicle parameters

Definition	Notation	Values	Unit
Mass of body	m_{11}	14.22	ton
Mass of bogies	m_{21}, m_{22}	6.20	ton
Spring constant of vertical air suspension	$K1_{ijn}$	900	kN/m
Vertical stiffness of the running tire	$K2_{ijn}$	509.58	kN/m
Lateral stiffness of the running tire	$Ky2_{ijn}$	255.820	kN/m
Aligning stiffness of the running tire	Ktz_{ijn}	25.582	kN/m
Lateral stiffness of the guide tire	$K3_{ijn}$	325	kN/m
Vertical stiffness of the guide tire	$Ky3_{ijn}$	55.820	kN/m
Lateral stiffness of the stabilizing tire	$K4_{i1n}$	325	kN/m
Vertical stiffness of the stabilizing tire	$Ky4_{i1n}$	55.820	kN/m
Spring constant of lateral air suspension	$K5_{i11}$	980	kN/m
Damping constant of vertical air suspension	$C1_{ijn}$	22.8	kN.s/m
Damping constant of running tire	$C2_{ijn}$	13.05	kN.s/m
Damping constant of guide tire	$C3_{ijn}$	92.75	kN.s/m
Damping constant of stabilizing tire	$C4_{i1n}$	92.75	kN.s/m
Damping constant of lateral air suspension	$C5_{i11}$	333.6	kN.s/m
Height between cog of car body and lateral air suspension	Lz_1	0.885	m
Height between cog of bogies and lateral air suspension	Lz_2	0.1	m
Height between cog of bogies guide tire	Lz_3	0.8375	m
Height between guide and stabilizing tires	Lz_4	0.97	m
Half-length right and left air suspension	Ly_2	0.949	m
Half-length right and left running tire	Ly_4	0.17	m